SANDIA REPORT

SAND2005-6824
Unlimited Release
Printed November 2005

3D Active Photonic Crystal Devices for Integrated Photonics and Silicon Photonics

James G. Fleming, Ihab F. El-Kady, Ganapathi S. Subramania, Paul G. Clem, Weng W. Chow, and Joel R. Wendt

Prepared by Sandia National Laboratories
Albuquerque, New Mexico 87185, and Livermore, California 94550

Sandia is a multiprogram laboratory operated by Sandia Corporation,
a Lockheed Martin Company, for the United States Department of Energy's
National Nuclear Security Administration under Contract DE-AC04-94AL85000.

Issued by Sandia National Laboratories, operated for the United States Department of Energy by Sandia Corporation.

Available to DOE and DOE contractors from
U.S. Department of Energy
Office of Scientific and Technical Information
P.O. Box 62
Oak Ridge, TN 37831

Telephone: (865)576-8401
Facsimile: (865)576-5728
E-Mail: reports@adonis.osti.gov
Online ordering: http://www.osti.gov/bridge

Available to the public from
U.S. Department of Commerce
National Technical Information Service
5285 Port Royal Rd
Springfield, VA 22161

Telephone: (800)553-6847
Facsimile: (703)605-6900
E-Mail: orders@ntis.fedworld.gov
Online order: http://www.ntis.gov/help/ordermethods.asp?loc=7-4-0#online

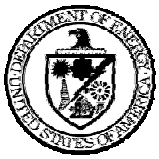

SAND2005-6824
Unlimited Release
Printed November 2005

3D Active Photonic Crystal Devices for Integrated Photonics and Silicon Photonics

James G. Fleming
MEMS Technology S&T

Ihab F. El-Kady, Ganapathi S. Subramania, Joel R. Wendt
Photonic Microsystems Technologies

Paul G. Clem
Microsystem Materials

Weng W. Chow
Semiconductor Mater and Device Sciences

Sandia National Laboratories
P.O. Box 5800
Albuquerque, NM 87185-0603

Abstract

Over the past 15 years, basic photonic crystals operating in optical wavelengths have been theoretically investigated and experimentally realized. New directions must now be set to understand fundamental photon-matter interactions and thus realize active photonic components for integrated and silicon-based photonic applications.

This proposal aims at two key areas to study. They are: (1) Thermal emission and silicon photonic crystal lasers— an aspect of photon-phonon interaction. (2) Optical interconnects-an aspect of photonic transport and mutual interaction. Understanding the underlining photon-phonon interaction, blackbody radiation can be altered, and wasted thermal energy recycled. Furthermore, we intend to build SOI based optical components, and study their mutual interaction for achieving complex optical functionality. Two examples are waveguide-cavity and cavity-cavity interaction for channel dropping filter applications.

Indeed, the next challenge in photonic crystal research is in material integration, in on-chip integration of photonic components, and lastly the realization of silicon lasers.

1 Introduction 6
1.1 Thermal emission of photonic crystals and photonic crystal silicon tight emitters 6
1.2 Optical switches and optical interconnects in photonic crystals— an aspect of photon-electron interaction and photonic transport 7
2 Accomplishments: 8
2.1 Observation of Sharp Emission Near the Band-Edge of 3D Metallic Photonic Crystals at λ=3.5-4.5μm Wavelength. 8
2.2 Experimental Realization of 3D Metallic Photonic Crystal at Near-Infrared Wavelength of λ=1.5μm Wavelength. 10
2.3 Experimental Realization of PEG Y-Splitters and a High-Q PBG Micro-Cavity. 11
2.4 Progress toward a short wavelength 3D tungsten photonic-lattice emitter. 11
2.5 Experimental Realization of 3D Metallic Photonic Crystal that can be designed to have selective absorption and emission bands in the Infrared. 12
2.6 Theoretical formulation and understanding of 3D tungsten photonic lattice emission. 13
3 Appendix I: List of Publications 15

1 Introduction

Over the past five years, Sandia National Laboratories has made seminal contributions to the field of photonic crystal. Most recently, thermal emission from a metallic 3D photonic crystal was observed to modify the blackbody radiation spectrum and funnel it into a narrow spectrum. This demonstration will lead to efficient light emitters for a wide range of wavelengths, from visible, infrared and to Tera-Hertz. The goal of this proposal is to explore such fundamental photon-matter interactions and to realize active photonic components for integrated photonics and silicon photonics applications.

This proposal aims at two key areas to study. They are: (1) thermal emission and silicon photonic crystal lasers— an aspect of photon-phonon interaction. (2) optical switches and optical interconnects in photonic crystals—an aspect of photon-electron interaction and photonic transport.

1.1 Thermal emission of photonic crystals and photonic crystal silicon tight emitters

A photonic crystal fundamentally changes the distribution of photonic density-of-states. This change impacts not just the better-known photon-electron but also the photon-phonon and photon-matter interactions; One example of this is the strong alteration of thermal emission of almost any material, dielectric or metallic. The emission spectrum may be suppressed, an important aspect for DOD infrared imaging applications, enhanced and even re-shaped. It is further suggested that the suppressed energy is not wasted, but rather is re-channeled and emitted into a selective frequency band. Very recently, an extraordinary emission enhancement is observed at Sandia in a 3D Tungsten photonic crystal; see Fig. l (a). Thus, a promising incandescent lamp with >49-50% efficiency becomes possible. It is our goal to realize white light emission using this new principle. However, the physical origin of the enhancement is not known at present. One possible mechanism is the formation of photon-atom bound system that enhances the emission rate. The new science of photon-phonon interaction will be explored in this proposal.

There are two possible approaches for fabricating the top and bottom mirrors for the proposed thermal lasers. One is to build similar layer-by-layer structure, but with 20-30% smaller dimensions, see Fig. l (b). This structure effectively extends the photonic band gap to a shorter wavelength and acts as an effective mirror. For example, four bottom layers could act as the high reflector (R_1~95%) and three top layers as the partial reflector (R_2~50-80%). One drawback for this design is that it adds seven additional layers to the existing structure, making the fabrication a more difficult task. A second design is to use dielectric DBR (distributed feedback) stacks, such as SiO2/SiN, as mirrors. These mirrors are planar and therefore easier to fabricate.

Although, the presence of the dielectric stacks makes it difficult to lift off the Tungsten 3D photonic-crystal from the silicon substrate.

The next challenge is to realize Tungsten photonic crystal in the λ=1μm and in the red color regime. The minimum feature size is in the order of 100-200nm and is currently beyond the MDL's fabrication capability. However, by combining better structure design and innovative process control, it is quite possible to achieve λ~600nm-1μm emission. At this wavelength, a complete process integration that includes electrical isolation, thermal isolation, and electrical contacts becomes essential. We believe once this step is achieved, packaging and testing of the incandescent devices becomes low cost and easy. Another focus at this stage of research is to study the effect of scaling on device performance, such as light emission efficiency. We will also study different structures with either a broad emission wavelength (for future white light application) or a narrow emission (for multi-color display application). We firmly believe that in the process of achieving these goals, many key patents will result.

1.2 Optical switches and optical interconnects in photonic crystals— an aspect of photon-electron interaction and photonic transport

There is tremendous interest in using photonic crystals for guiding and directing light for optical communication applications. For on-chip control of light, we propose to use 2D photonic crystal slab structure that Sandia pioneered to achieve (1) efficient optical interconnect and (2) dynamic signal routing. For the vertical coupling and a subsequent in-plane processing of light, a 3D layer-by-layer photonic crystal will be used.

Waveguides, bends and splitters are among the most basic components for achieving optical interconnects. The loss and bandwidth are two of the most important issues that will be addressed. A full 3D numerical simulation will be carried out to design and minimize various losses, such as the guiding, bending and splitting losses. Examples of a power splitter and a waveguide bend are shown in Fig.1 (a) and (b). It is to be noted that such components are very compact (3-5 μm in size) and suitable for a large-scale monolithic integration. Indeed, a successful demonstration of this work will lead to the realization of photonic VLSI. For system applications, the problem of efficiently coupling light into and out of a localized cavity or waveguide in a photonic crystal will be addressed.

A means of altering the photonic band gap behavior is use of ferroelectric materials with large electro optic coefficients to electrically tune the PBG composite refractive index. This would enable changes in transmission coefficient at GHz to THz speeds, enabling PBG waveguide switches and other applications. The electro optic materials of interest display either linear (Pockels $\Delta n_i = -1/2\ n^3\ r_{ij}\ E_i$) or quadratic (Kerr $\Delta n_i = -1/2\ n^3\ r_{ij}\ E_i\ E_k$) electro optic behavior upon application of bias fields, depending on whether they are in the ferroelectric state or not, respectively. Examples of such linear and quadratic electro optic materials are listed in Table I, along with the index change An on application of a

5-10 V/μm (50-100 kV/cm) electric field. As displayed in the table, there are numerous ways to achieve index changes of 10^{-2} or greater to tune the properties of PBG with such materials. A Δn of 0.1 is sufficient to switch the resonant frequency of a high-Q micro-cavity, shown in Fig.1(c), for high-speed on-off switching.

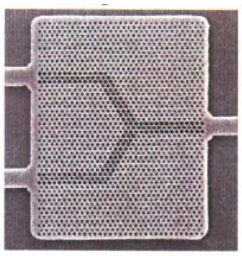

Fig . 1(a)

Fig . 1(b)

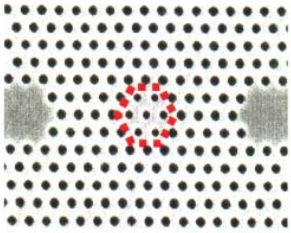

Fig . 1(c)

Table I: Selected electro optic oxides and index change at 5-10 V/μm

Material	linear coefficient	quadratic coefficient	Δn (E)
$Pb_{.92}La_{.08}Zr_{.40}Ti_{.60}O_3$		3.86×10^{-15} (m/V)^2	0.82 (5 V/μm)
$Pb_{.92}La_{.08}Zr_{.65}Ti_{.65}O_3$	1.0×10^{-10} m/V		0.01 (10 V/μm)
$Sr_{.75}Ba_{.25}NbO_3$	1.34×10^{-9} m/V		0.10 (10 V/μm)

2 Accomplishments:

2.1 Observation of Sharp Emission Near the Band-Edge of 3D Metallic Photonic Crystals at λ=3.5-4.5μm Wavelength.

A three-dimensional tungsten photonic-crystal is realized with a photonic band-edge at λ~4μm wavelength. Its thermal emission is suppressed in the band-gap regime and, at the same time, exhibits sharp peaks near the band-edge. It is further observed that energy conversion-efficiency from one side of the sample reaches T~40%. This finding is attributed to a complete metallic photonic band-gap in the infrared (λ≥6μm) and the enhanced density of photon-states near the band-edge of our tungsten photonic-crystal.

In Fig. 2(a), the measured reflection (black color) and absorption (blue color) spectra from a five-layer tungsten PBG sample are shown, respectively. The 3D metallic photonic band-gap at λ>6μm is a complete gap and is effective (~30dB/unit cell) in trapping light fully in all 4π solid angles and for both polarizations. In Fig. 2(b), the measured emission spectra at low biases (V<0.20V) are shown. The broad peak behaves

like a gray-body radiation. The three sharp peaks are pinned at their respective wavelengths and are independent of sample temperatures.

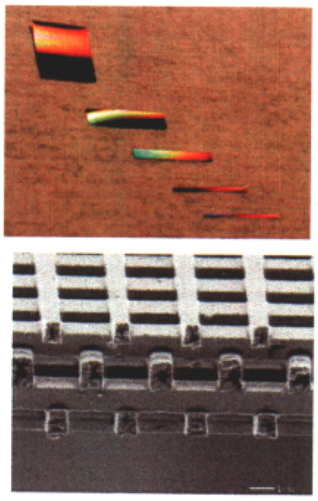

Fig . 2(a),(b)

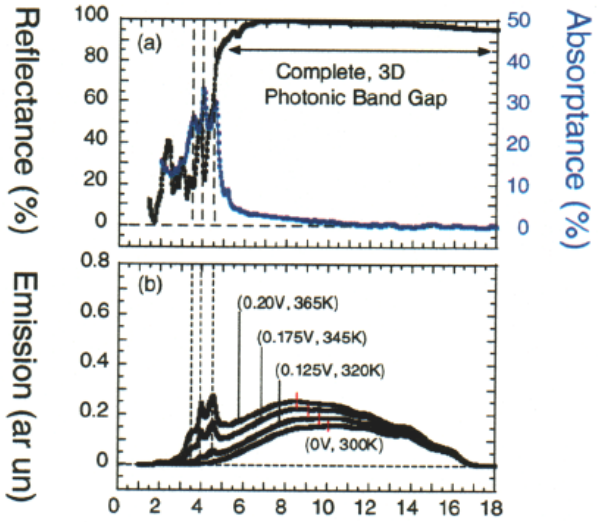

Fig . 3(a),(b)

In Fig. 3(a), the sharp peaks dominate the emission spectrum. In Fig. 3(b), the emission amplitudes are summarized as a function of P_{in} at λ=4, 4.5μm (the sharp peaks) and λ=8μm (the broad emission), respectively. For P_{in}>150mW, the amplitudes at λ=4/4.5μm far exceed that at λ=8μm. Furthermore, the emitted power scales linearly with P_{in} at high input power (indicated by the dash line) and reaches η=40% electric-to-radiation conversion-efficiency. Taking into account radiation from the top and bottom emitting-surfaces, the conversion-efficiency is expected to be ~80%.

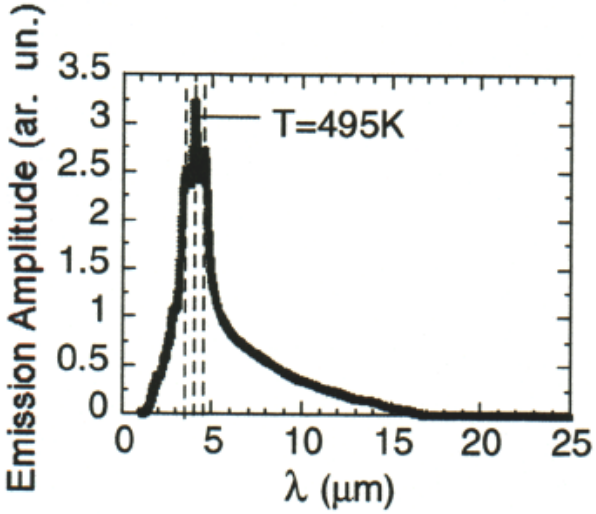

Fig . 4(a) Emission Spectrum at T=495K

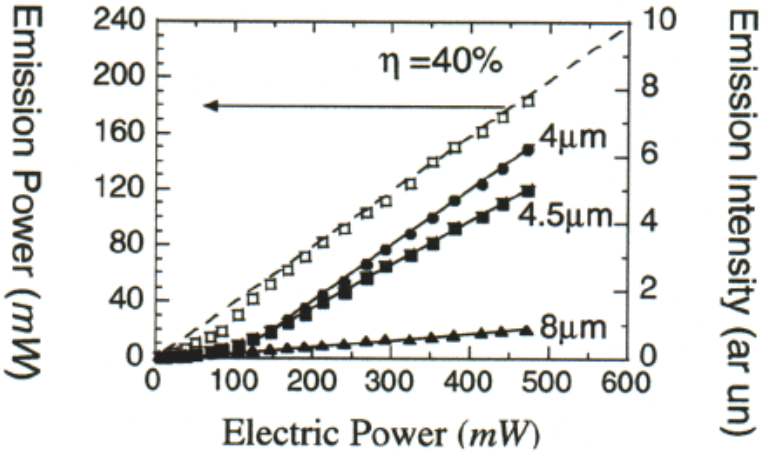

Fig . 4(b) Emission intensity and power vs input power

2.2 *Experimental Realization of 3D Metallic Photonic Crystal at Near-Infrared Wavelength of λ=1.5μm Wavelength.*

Our next effort is to reduce the emission wavelength of our photonic-crystal sample into near-infrared (λ=1-2μm) and eventually into visible (λ~400-700nm) wavelengths. An emission at λ=1.5μm is an important first step for realizing highly efficient thermal photo-voltaic electric generators. A GaSb photovoltaic-cell used for this application has a wavelength cut-off at λ=1.7μm.

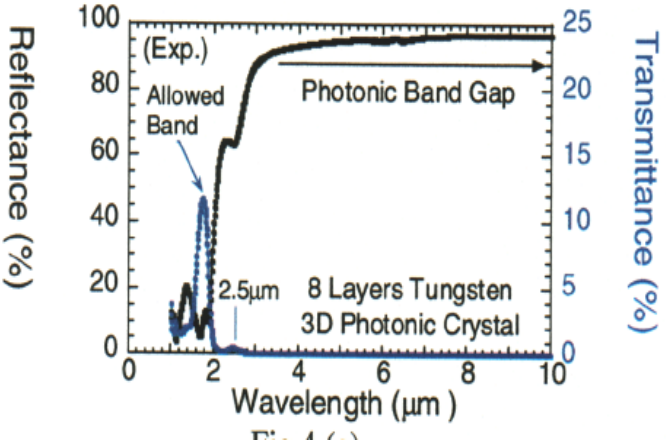

Fig . 5(a)

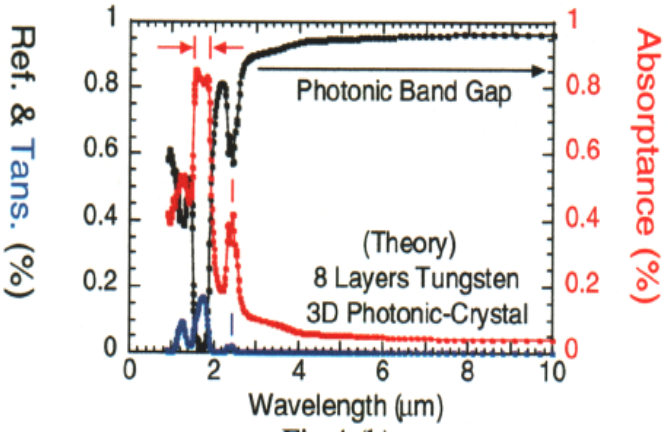

Fig . 5(B)

The 3D near-infrared metallic photonic crystal is successfully realized and its transmission and reflection spectra are shown in Fig. 4(a). The band edge is at λ~2μm. In Fig. 4(b), computed results of the reflection (black curve), transmission (blue curve) and absorption (red curve) spectra are shown, respectively. The absorptance exhibits two absorption peaks, indicating that emission can occur at both bands. The emission is shown in Fig. 5(a) and (b) for low, intermediate and high temperatures. The photograph

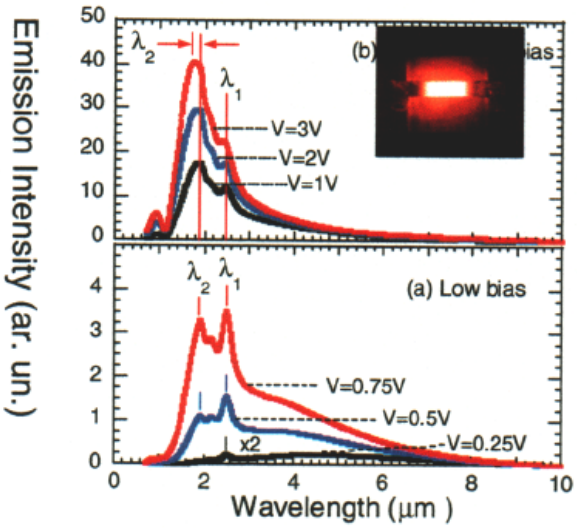

Fig . 6(a)

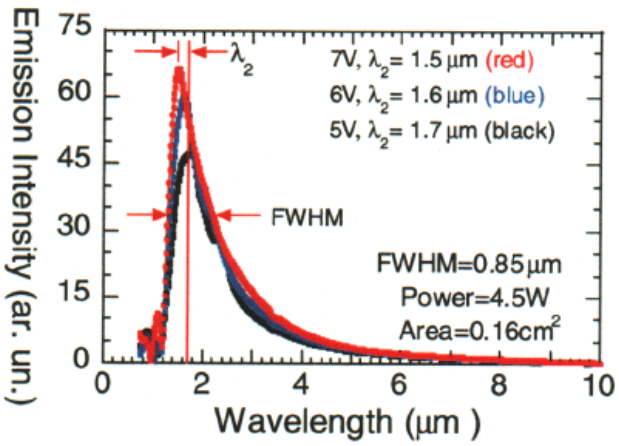

Fig . 6(b)

shown in the inset of Fig. 5(b) is due to a slight visible emission at the tail of the emission peak.

2.3 Experimental Realization of PEG Y-Splitters and a High-Q PBG Micro-Cavity.

We report the successful experimental realization of a photonic crystal y-splitter, operating at λ~1.6μm. Our device has a large splitting angle of 120-degrees, a miniaturized size of ~ (3x3) μm^2 and y-splitter loss of (0.5-1) dB at λ=1640-1680nm, making it promising for integrated photonic-circuit applications. In Fig. 6(a), the two y-splitter output powers are shown as a function of position of input laser beam relative to the input waveguide. Clearly, the total power is close to that of the reference waveguide, indicating a nearly loss less and perfect splitting of light. A high-Q micro-cavity operating at λ=1517nm is also successfully realized using a 2D photonic crystal slab approach. The transmission spectrum is shown in Fig. 6(b), exhibiting a cavity-Q of 1800. This cavity-Q value is two times higher than previously achieved. With this accomplishment, we are now ready to explore non-linear material coatings for electro-optical switching experiments.

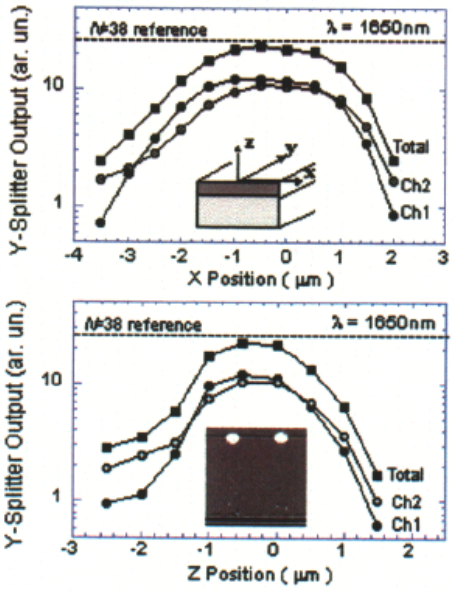

Fig . 7(a)

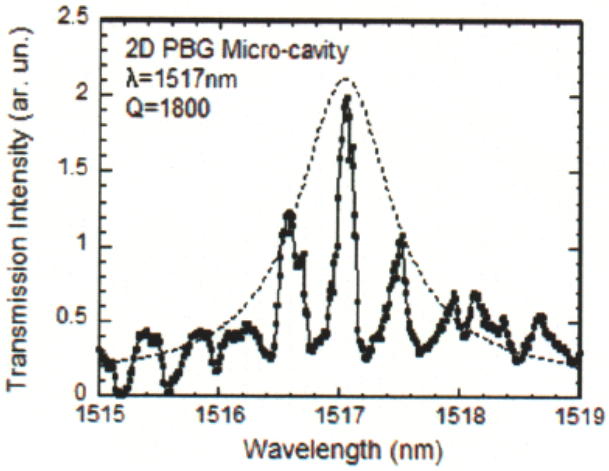

Fig . 7(b)

2.4 Progress toward a short wavelength 3D tungsten photonic-lattice emitter.

A three-dimensional tungsten photonic-crystal is realized Fig. 7(a, b) with a photonic band-edge at λ~2μm wavelength. Different from our earlier report of emission hear the band edge, this new emission is associated with a narrow allowed band. As shown in Fig. 7(c), the lattice emission peak occurs at λ~1.5μm with a high power (a few Watts).

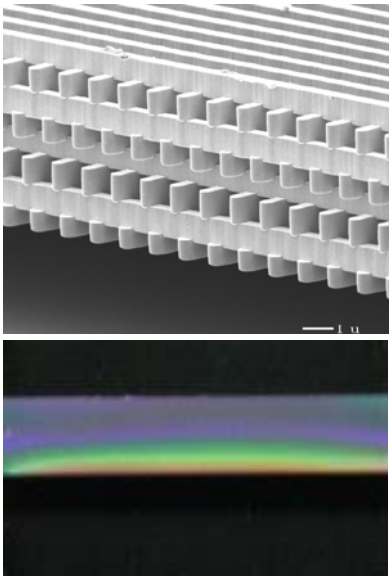

Fig . 8(a),(b)

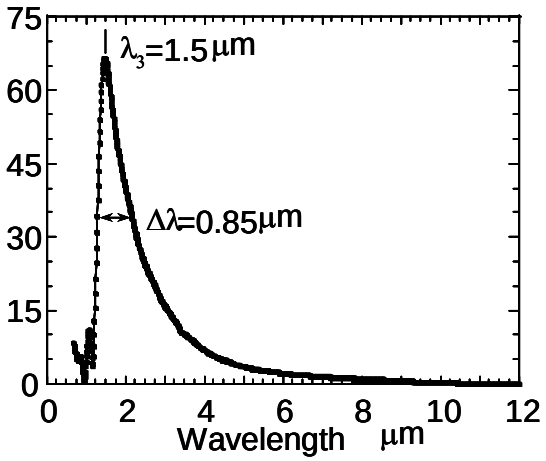

Fig . 8(c)

2.5 Experimental Realization of 3D Metallic Photonic Crystal that can be designed to have selective absorption and emission bands in the Infrared.

Our next effort was to engineer the emission wavelength of our photonic-lattice by changing its lattice constant, a. As the first step, a series of absorption spectrum were computer generated for a range of different lattice constants. The spectra are shown in Fig. 8(a), indicating a systematic shifting of absorptance peaks as a function lattice constant. This data clearly illustrates that the internal lattice structure does modify the intrinsic photon-tungsten absorption process. For reference purposes, absorptance of a uniform tungsten slab is also shown as the blue curve. The peak lattice absorption ranges from 0.6 to 0.92, which is much larger that of a uniform tungsten slab.

The corresponding emission spectra are shown in Fig. 8(b). The emission peaks are observed to also shift systematically with the lattice constant. A plot of the emission peak

as a function of lattice constant indicates a linear relationship. We now have a good handle on engineering the emission wavelength at infrared wavelengths.

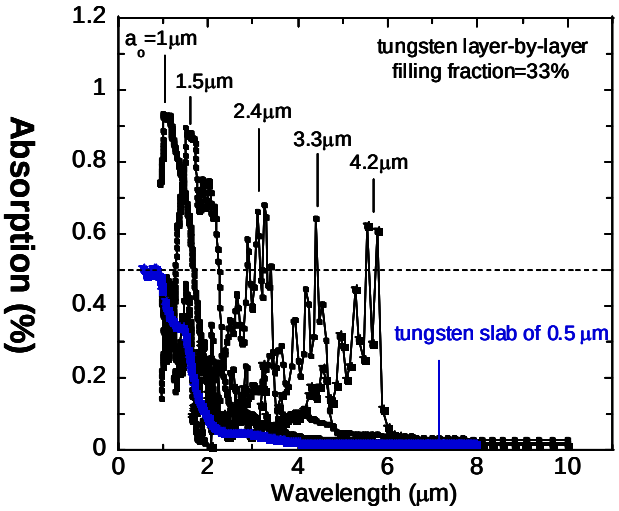

Fig . 9(a)

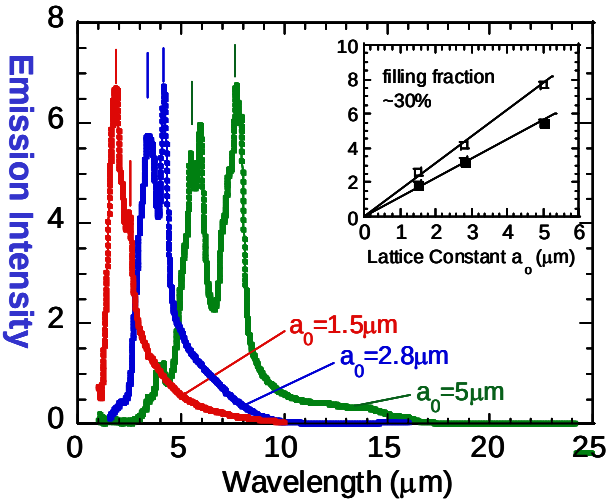

Fig . 9(b)

2.6 Theoretical formulation and understanding of 3D tungsten photonic lattice emission.

In this part of the project we investigated the thermal emission characteristics of a metallic layer-by-layer photonic lattice using a first principles quantum optics approach. The approach is based on a two-level quantum electrodynamics treatment of the host photonic lattice as a two-level system interaction with a multi-mode radiation field. The system is thermally pumped and the emission spectrum is calculated.

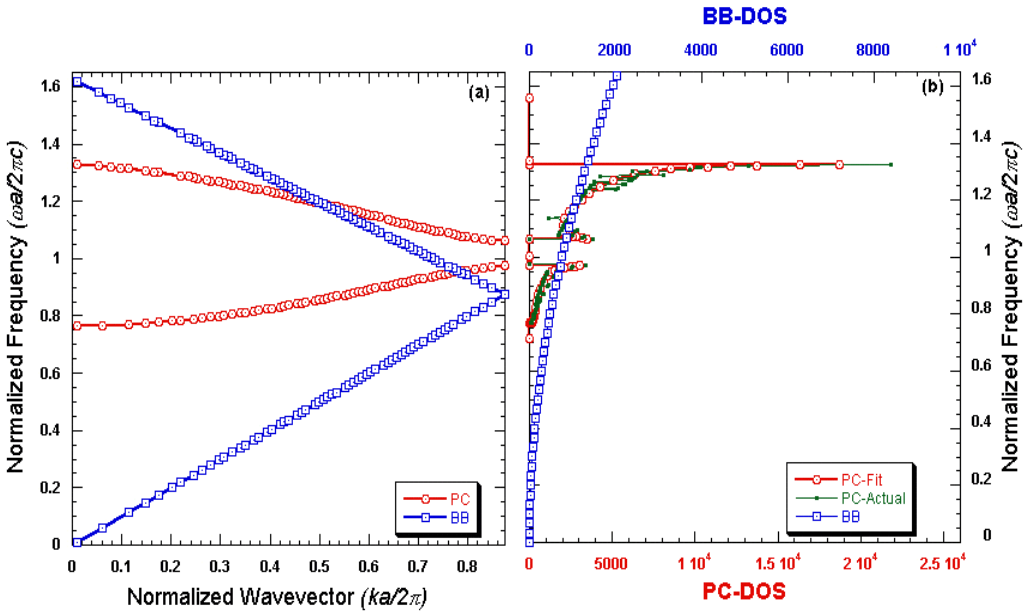

Fig . 10(a),(b)

In Fig. 10(a), the frequency-momentum dispersion is shown for our photonic lattice (red curve) assuming that the imaginary part of tungsten's dielectric constant is zero. For comparison purposes, the free space dispersion is also shown as the blue curve. The photonic density-of-states (DOS) can then be derived from the dispersion curve and is shown in Fig. 10(b). In particular, there are peaks centered at 0.95, 1.05 and 1.35.

The corresponding emission spectrum is shown in Fig. 11. Three emission peaks were predicted, corresponding to the peaks in DOS as shown in Fig. 10(b). This calculation provides a framework for understanding the emission process of our lattice emission.

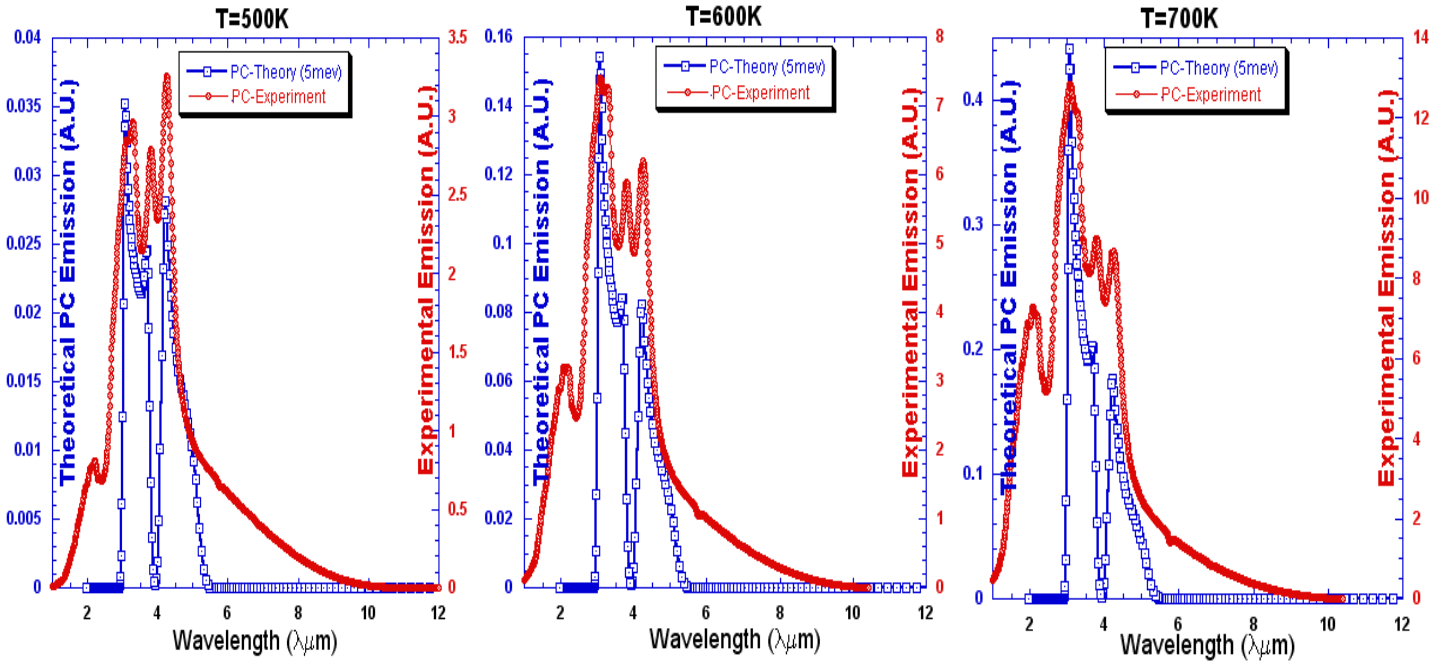

Fig . 11(a),(b),(c)

3 Appendix I: List of Publications

(1) "Thermal Emission from an Active Metallic Photonic Crystal: Theory and Experiment", I. El-Kady, W. W. Chow, J. G. Fleming. PHOTONIC NANO-STRUCTURES FUNDAMENTALS AND APPLICATIONS, submitted Oct. 2005.

(2) "I", I. El-Kady, W. W. Chow, J. G. Fleming. PHYSICAL REVIEW B, accepted for publication, Sep. 2005.

(3) "Experimental Observation of Photonic-Crystal Emission Near a Photonic Band Edge", S-Y Lin, J. G. Fleming, I. El-Kady. APPLIED PHYSICS LETTERS, Jul. 28, 2003, V. 83, No. 4, Pg. 593-595.

(4) "Three-Dimensional Photonic-Crystal Emitter for Thermal Photovoltaic Power Generation", S-Y Lin, J. Moreno, J. G. Fleming. APPLIED PHYSICS LETTERS, Jul. 14, 2003, V. 83, No. 2, Pg. 380-2.

(5) "Origin of Absorption Enhancement in a Tungsten, Three-Dimensional Photonic Crystal", S-Y Lin, J. G. Fleming, ZY Li, I. El-Kady, R. Biswas, K. M. Ho. JOURNAL OF THE OPTICAL SOCIETY OF AMERICA B (OPTICAL PHYSICS), Jul. 2003, V. 20, No. 7, Pg. 1538-41.

(6) "Three-Dimensional Photonic-Crystal Emission Through Thermal Excitation", S-Y Lin, J. G. Fleming, I. El-Kady. OPTICS LETTERS, Oct. 15, 2003, V. 28, No. 20, Pg. 1909-1911.

(7) "Highly Efficient Light Emission at LAMBD = 1.5 {mu}m by a Three-Dimensional Tungsten Photonic Crystal", S-Y Lin, J. G. Fleming, I. El-Kady, OPTICS LETTERS, Sept. 15, 2003, V. 28, No. 18, Pg. 1683-5.

(8) "Efficient Light Emission by a Three-Dimensional, All-Metallic Photonic Crystal and Its Energy Consequences", S-Y Lin, J. G. Fleming. PROCEEDINGS OF THE SOCIETY OF PHOTO-OPTICAL INSTRUMENTATION ENGINEERS (SPIE), 2003, V. 5000, Pg. 1-7.

Thermal Emission from an Active Metallic Photonic Crystal: Theory and Experiment

I. El-Kady, W. W. Chow, and J. G. Fleming
Sandia National Laboratories, P.O. Box 5800, Albuquerque, NM 87185-0603
(Dated: September 16, 2005)

A quantum optics approach coupled with plane wave expansion and transfer matrix techniques are used to calculate the thermal emission from an active 3D metallic photonic crystal. The emitting source is modeled as a collection of inhomogenously broadened two-level systems that is allowed to equilibrate via collisions to a Maxwell-Boltzmann distribution at a specific temperature. Emission and absorption processes create a photon population distribution within the photonic lattice as dictated by the photonic lattice bandstructure. This population distribution is then coupled to the exterior to give the output of the active photonic crystal. The outcoupling of the intracavity radiation is investigated with different schemes: passive photonic filter and a photonic crystal cavity coupler. Calculated emission spectra show good agreement with experiments performed under lossy and low-loss radiative conditions.

PACS numbers:

I. INTRODUCTION

A photonic crystal (PC) introduces a periodic perturbation in the refractive index of the medium. This in turn results in the generation of a particular photonic band structure characterized by the suppression of the photon density of states along certain crystallographic directions and the propagation of selected Bloch-modes mandated by translational symmetry in others. The result is a multitude of novel optical phenomena among which are: inhibition of spontaneous emission[1–3] , slow and frozen light modes due to the drastic reduction in group velocity[4,5], exceedingly large cavity quality factors[6], low threshold lasing[7,8] , and modified thermal emission characteristics[9,10].

In this article we focus on the thermal emission characteristics from metallic photonic lattices. Several theoretical as well as experimental studies conducted thus far have reported exceedingly high emission intensities at the photonic band edges[9,11,12]. Most of the theoretical approaches however, were based on the direct or indirect use of Kirchoff's law. While such an approach is widely accepted when treating passive radiation filters and hot mirrors, where the source and the Kirkoffian element are separate entities, it is unclear how one could extend the use of such a classical approach to treat an active PC source. In addition, none of the previous studies, to our knowledge, have addressed the essential issue of contrasting results between theoretical predictions and experimental observations. In this article we present a quantum optics approach coupled with well established electromagnetic numerical simulation techniques to calculate the emission from an active metallic PC. The model is then evaluated for accuracy by showing that it correctly retrieves Plank's blackbody distribution in absence of the PC. A further reinforcement of the model is given by showing that it correctly reproduces the emission peak wavelengths and relative peak intensities measured experimentally under two different limiting conditions.

II. THEORETICAL FORMULATION

We begin by separating the emission problem into three stages. First the active photonic lattice is modeled as inhomogeneously broadened ensemble of two-level systems interacting with a quantized multimode radiation field. The composite system is excited by an external pump and allowed to equilibrate with a thermal bath via collisions. The generated photon population is then subjected to the photonic density of states mandated by the host PC lattice, which in turn determines the modal properties of the radiation field[13]. A passive photonic coupling factor then dictates the radiation coupling strength to the exterior of the PC lattice.

In deriving the working equations, we label each two-level system with n, so that $|a_n\rangle$ and $|b_n\rangle$ are the ground and excited states, respectively, that are separated by energy $\hbar\omega_n$. Correspondingly, each radiation field mode has energy $\hbar\Omega_k$, and is described by creation and annihilation operators $a_k^\dagger$ and a_k, respectively. The relation between Ω_k and k depends on the photonic lattice structure. The Hamiltonian for the combined matter and radiation field system is[13,14]

$$H = \sum_n \hbar\omega_n |b_n\rangle\langle b_n| + \sum_k \hbar\Omega_k a_k^\dagger a_k - \sum_{k,n} g_k \left(|b_n\rangle\langle a_n| a_k + a_k^\dagger |a_n\rangle\langle b_n| \right) , \quad (1)$$

where dipole interaction is assume, with $g_k = \mu \left[\hbar\Omega_k / \left(\varepsilon_0 V\right)\right]^{1/2}$, μ is the dipole matrix element, ε_0 is the permittivity in vacuum and V is the system volume. Working in the Heisenberg picture, we derive the following equations of motion for the photon, excited-state and ground-state populations, $n\left(\Omega, t\right)$, $n_a\left(\omega_n, t\right)$ and $n_b\left(\omega_n, t\right)$, respectively:

$$\begin{aligned}
\frac{dn_a(\omega_n,t)}{dt} &= \frac{2\pi}{\hbar^2}\rho\left(\omega_n\right) g\left(\omega_n\right)^2 \left\{\left[n_b\left(\omega_n,t\right) - n_a\left(\omega_n,t\right)\right] n\left(\omega_n,t\right) + n_b\left(\omega_n\right)\right\} \\
&\quad - \gamma_r\left[n_a\left(\omega_n,t\right) - f_a\left(\omega_n,T\right)\right] - \Lambda\left(\omega_n\right) n_a\left(\omega_n,t\right) \qquad (2) \\
\frac{dn_b(\omega_n,t)}{dt} &= -\frac{2\pi}{\hbar^2}\rho\left(\omega_n\right) g\left(\omega_n\right)^2 \left\{\left[n_b\left(\omega_n,t\right) - n_a\left(\omega_n,t\right)\right] n\left(\omega_n,t\right) + n_b\left(\omega_n\right)\right\} \\
&\quad - \gamma_r\left[n_b\left(\omega_n,t\right) - f_b\left(\omega_n,T\right)\right] + \Lambda\left(\omega_n\right) n_a\left(\omega_n,t\right) \qquad (3) \\
\frac{dn(\Omega,t)}{dt} &= \frac{2}{\hbar^2} g\left(\Omega\right)^2 \sum_n \frac{\gamma}{\left(\omega_n - \Omega\right)^2 + \gamma^2} \\
&\quad \times \left\{\left[n_b\left(\omega_n,t\right) - n_a\left(\omega_n,t\right)\right] n\left(\Omega,t\right) + n_b\left(\omega_n,t\right)\right\} - \gamma_c n(\Omega,t) \qquad (4)
\end{aligned}$$

In the formulation, we assume that the polarization dephasing rate γ is much faster than the time variations in the active medium and photon populations, so that the polarization equation may be adiabatically eliminated. In Eqs. (2) and (3), $\rho\left(\omega\right)$ is the photon-lattice density of states, which is assumed to be spherically symmetric. Additionally, the pump and decay contributions are included phenomenologically, where γ_c is the photon decay rate, $\Lambda\left(\omega_n\right) = \Lambda_0 \exp\left[-\hbar\omega_n / \left(k_B T_p\right)\right]$ is the pump rate, and γ_r is the effective rate for the actual populations n_a and n_b to relax to the equilibrium distributions $f_a(\omega_n, T) = Z_o$ and $f_b(\omega_n, T) = Z_o \exp\left[-\hbar\omega_n / \left(k_B T\right)\right]$, where Z_o is the thermodynamic partition function, $N_o = \sum_n \left[f_a(\omega_n) + f_b(\omega_n)\right]$ is the total number of two-level systems, T_p and T are the pump and reservoir temperatures. Solving (2) to (4) gives the photon population $n(\Omega)$, which is used in

$$u\left(\lambda\right) = \Gamma(\lambda)\frac{d\Omega}{d\lambda}\hbar\Omega\rho\left(\Omega\right) n(\Omega) \qquad (5)$$

to obtain the emission wavelength spectrum outside the photonic lattice enclosure. In (5), $\Gamma(\lambda)$ is the coupling factor describing the efficiency with which radiation within the interior of the PC is coupled to its exterior. To evaluate $\Gamma(\lambda)$, two coupling schemes are considered: a *passive photonic filter* scheme, and a *passive photonic cavity* scheme. In the first scenario, we assume that after the generation of the steady state photon population, the PC simply acts as a passive filter in which case:

$$\Gamma_{Filter}(\lambda) = 1 - \left[R(\lambda) + A(\lambda)\right] \qquad (6)$$

In the cavity coupling scenario, on the other hand, the encapsulating PC is viewed as an imperfect cavity with a radiation outcoupling factor of:

$$\Gamma_{Cavity}(\lambda) = \frac{-C}{L_{eff}} ln\left[R(\lambda) + A(\lambda)\right] = \frac{-C}{L_{eff}} ln\left[1 - \Gamma_{Filter}(\lambda)\right] \qquad (7)$$

In (6) and (7), $R(\lambda)$ is the reflectivity and $A(\lambda)$ is the absorptivity of the PC, L_{eff} is the effective cavity length, and C is the speed of light.

We consider a tungsten Lincoln-Log PC with square cross-section rods and a 28.5% filling fraction. A coupled-wave method is used to compute the bandstructure, where the fields and dielectric functions are expanded in terms of plane waves. Maxwell's equations are cast in an eigen problem format in Fourier space and solved using a transfer matrix approach by treating each layer of the structure as an independent 2D Lamellar grating. Details of this method and its accuracy in describing our structure are discussed elsewhere.[15] Following customary laser physics procedure[16], we assume that the modal and outcoupling effects may be, to a good approximation, determined separately. The reflectivity $R(\lambda)$ and absorption $A(\lambda)$ are obtained by an independent frequency domain transfer matrix calculation performed on six layers of the photonic crystal structure.[17]

Figure 1 (a) shows the photonic-lattice dispersion in the (001) crystallographic direction (red curve). Clearly visible are the fundamental and first higher order gaps, as well as the significant flattening of the dispersion at the bandedges due to anticrossing. The red line in Fig. 1 (b) give the density of states (DOS) $\rho(\omega)$ computed from the dispersion,

assuming spherical symmetry. Note the drastic increases in DOS as the photonic crystal dispersion flattens at the band edges. For comparison, Fig. 1 also shows the free-space dispersion and DOS (dashed blue curves).

Using the photonic-crystal DOS, (2) and (4) are solved numerically with a fourth-order Runge-Kutta finite difference method. Following previous comparisons of photonic crystal and blackbody emissions, we ensure that the steady-steady active-medium populations $n_a(\omega_n)$ and $n_b(\omega_n)$ are to a good approximation given by the equilibrium distributions $f_a(\omega_n, T)$ and $f_a(\omega_n, T)$ by performing the calculations for low excitation and rapid relaxation conditions, specifically, with $\gamma = 10^{14}s^{-1}$, $\gamma_r = 10^{12}s^{-1}$, and $\gamma_c = \Lambda_0 = 10^9 s^{-1}$. Furthermore, we choose $\mu = e \times 0.5nm$, $V = 10^{-18}m^{-3}$, $N_0 = 200$ and $T_p = T$. The steady-state solutions to (2) and (4), are used in (5), with two limits (as discussed in the next section) to the coupling function $\Gamma(\lambda)$, to obtain the emission spectrum.

III. RESULTS AND DISCUSSION

The coupling factor depends on experimentally imposed boundary conditions. To estimate the upper emission limit, we consider the best-case scenario of negligible nonradiative losses, so that every photon absorbed by the photonic lattice structure is eventually remitted into a propagating Bloch-mode. This case gives a maximum coupling factor of $\Gamma_{max}(\lambda) = 1 - R(\lambda)$ for the filter coupling scheme, and $\Gamma_{max}(\lambda) = \frac{-C}{L_{eff}} lnR(\lambda)$ for the cavity coupling scheme. A lower bound for the photonic-crystal emission may be obtained, on the other hand, by considering the worst-case scenario where all secondary photon absorption processes result in nonradiative losses. This situation gives minimal coupling functions of $\Gamma_{min}(\lambda) = 1 - R(\lambda) - A(\lambda)$, and $\Gamma_{min}(\lambda) = \frac{-C}{L_{eff}} ln[R(\lambda) + A(\lambda)]$, where $A(\lambda)$ is calculated using the complex dielectric constant for tungsten[18], for the filter and cavity coupling schemes respectively. Fig.2 shows a plot of the extrema coupling factors for both schemes. In practice, the experimental emission results should thus lie between these two bounds.

Figure 3 shows the calculated lower bound emission spectra using the filter (blue curve) and cavity (green curve) coupling schemes at different temperatures. The figure clearly shows the suppression of photonic lattice emission intensity at the photonic bandgaps. More importantly, they indicate a significant increase in intensity at the bandedges. Figure 3 also depicts (with a different vertical scale) the experimentally measured spectra (red curve) for a 6 layer tungsten Lincoln-log structure obtained in a simple thermal heating experiment where the PC lattice is placed on a temperature controlled copper block. In this experiment non-radiative losses are dominated by conductive losses through the large copper thermal mass. At equilibrium, the temperature of the block and PC is assumed to be identical and was measured by means of a thermocouple embedded in the copper block. Inhomogeneous broadening of $20meV$ is included to approximate experimental line broadening due to crystal imperfections. Remarkable agreement is observed between calculation based on the filter coupling scheme and experiment, in terms of the wavelength and relative magnitude of the intensity peaks. Similar results are observed using the cavity coupling scheme (green curve), though the agreement with the experiment, while acceptable, it is not as good as the filter coupling scheme.

Figure 4 shows a comparison between the calculated and measured PC emission spectra (again on different vertical scales) for the optimal situation of negligible nonradiative losses using the filter (blue curve) and cavity (green curve) coupling schemes at different temperatures. Again an inhomogeneous broadening $5meV$ is included to approximate line broadening due to crystal imperfections. In this case the 6 layer tungsten Lincoln-log structure is suspended in vacuum by wires. Nonradiative losses are reduced by having, asside from the wires, a free-standing structure. The experimental structure was electrically excited by Joule heating. To determine the temperature, the experiment was repeated with blackbody paint coating the central region of the crystal, which then acted as the heating element. Since the blackbody paint behaved essentially as a perfect electrical insulator, it did not change the electrical conductivity of the sample. The temperature was deduced by matching the change in electrical resistivity of the photonic crystal in the two experiments, and using Wein's law for the relationship between temperature and blackbody emission peak. Better agreement with the experimental results is observed with the calculation based on the cavity coupling scheme as compared to the filter coupling scheme. The experimental emission peak at $\sim 2\mu m$ is absent in the calculated results because the bandstructure calculation was terminated at the edge of the second band at $\sim 3\mu m$.

The alternating performance between the two coupling approaches when compared to the experiment is quite puzzling, and is under investigation. However, regardless of the coupling scheme, generally good agreement between theory and experiment is observed. Demonstration of the agreement between experiment and theory to the accuracy and detail depicted in Figs. 3 and 4 has not been previously reported.

IV. SUMMARY AND CONCLUSION

In summary, we have presented a theoretical approach for calculating the emission from an active photonic-lattice crystal using a model consisting of an inhomogeneously broadened ensemble of two-level systems interacting with a quantized radiation field whose modal properties are determined by the photonic-lattice bandstructure. The model is general and produces the emission spectra for arbitrary photonic-lattice configurations. In this work, the example of a 6 layer tungsten Lincoln-log active PC was investigated. Good agreement with experiments performed under conditions approximating emission extrema is obtained and serves to underline the validity of our approach. Comparison of photonic-lattice and blackbody emission shows appreciable modification of the blackbody spectrum by the photonic lattice, where the redistribution of the photonic density of states results in suppression of emission at certain wavelengths and enhancement at others. Finally we wish to emphasize that the parameter space explored excludes situations involving non-equilibrium population effects, even though these effects can be treated within the framework of the present model.

This work was supported the U. S. Department of Energy under contract No. DE-AC04-94AL85000 and the Alexander von Humboldt Foundation.

[1] E. Yablonovitch, Phys. Rev. Lett. **58**, 2059 (1987).
[2] S. John and J. Wang, Phys. Rev. Lett. **64**, 2418 (1990).
[3] R. Sprik, B.A van Tiggelen, and A. Lagendijk, Europhysics Lett. 35, (1996).
[4] S. John and J. Wang, Phys. Rev. B **43**, 12772 (1991).
[5] S. John and T. Quang, Phys. Rev. A **50**, 1764 (1994).
[6] G. Subramania, S. Y. Lin, J. R. Wendt and J. M. Rivera, Appl. Phys. Lett. **83**, 4491 (2003).
[7] O. Painter, R. K. Lee, A. Scherer, A. Yariv, J. D. O'Brien, P. D. Dapkus, I. Kim, Science **284**, 1819 (1999).
[8] H.-Y. Ryu, S.-H. Kwon, Y.-J. Lee, Y.-H. Lee, J.-S. Kim, Appl. Phys. Lett. **80**, 3476 (2002).
[9] C.M. Cornelius and J.P. Dowling, Phys. Rev. A **59**, 4736 (1999).
[10] S.Y. Lin, J.G. Fleming, E. Chow, J. Bur, K.K. Choi, A. Goldberg, Phys. Rev. B. **62**, R2243 (2000).
[11] J. G. Fleming, S.Y. Lin and I. El-Kady, Appl. Phys. Lett. **83**, 593 (2003).
[12] T. Trupke, P. Würfel and M. A. Green, Appl. Phys. Lett. **84**, 1997 (2004)
[13] N. Vats, S.John, K. Busch, Phys. Rev. A **65**, 043808 (2002).
[14] M.O. Scully, M.S. Zubairy, *Quantum Optics*, Cambrdge University Press, Cambridge, (1977).
[15] L-L. Lin, Z-Y. Li, K-M. Ho, J. App. Phys. **94**, 811 (2003).
[16] Sargent, M. III, M. O. Scully and W. E. Lamb, Jr. *Laser Physics*, (Addison-Wesley, Reading, 1974).
[17] Z-Y Li and K-M Ho, Phys. Rev. B **67**, 165104 (2003).
[18] D. R. Lide, *Handbook of Chemistry and Physics,* 83th ed. (CRC Press, Boca Raton, 2003).
[19] Lin, S.Y., Moreno, J., Fleming, J.G., Appl. Phys. Lett., Vol. 83, No.2, (2003).
[20] K.M. Ho, C.T. Chan, C.M. Soukoulis, R. Biswas, M. Sigalas, Solid State Commun. **89**, 413 (1994).

Figure Captions

Fig. 1. Calculated tungsten Lincoln-log photonic crystal (red) and free-space (blue) (a) dispersions and (b) photonic densities of states.

Fig. 2. Coupling factor extrema values: lossy (red), and lossless (black) for a 6 layer tungsten Lincoln-log photonic crystal for (a) the filter coupling scheme and (b) the cavity coupling scheme.

Fig. 3. Comparison of the calculated lossless photonic-crystal emission spectra using the filter (blue) and cavity (green) coupling schemes with the experimental spectra at different temperatures (a) $500K$, (b) $600K$ and (c) $700K$. A $5meV$ inhomogeneous broadening is included in the calculations.

Fig. 4. Comparison of the calculated lossy photonic-crystal emission spectra using the filter (blue) and cavity (green) coupling schemes with the experimental spectra at different temperatures (a) $500K$, (b) $600K$ and (c) $700K$. A $20meV$ inhomogeneous broadening is included in the calculations.

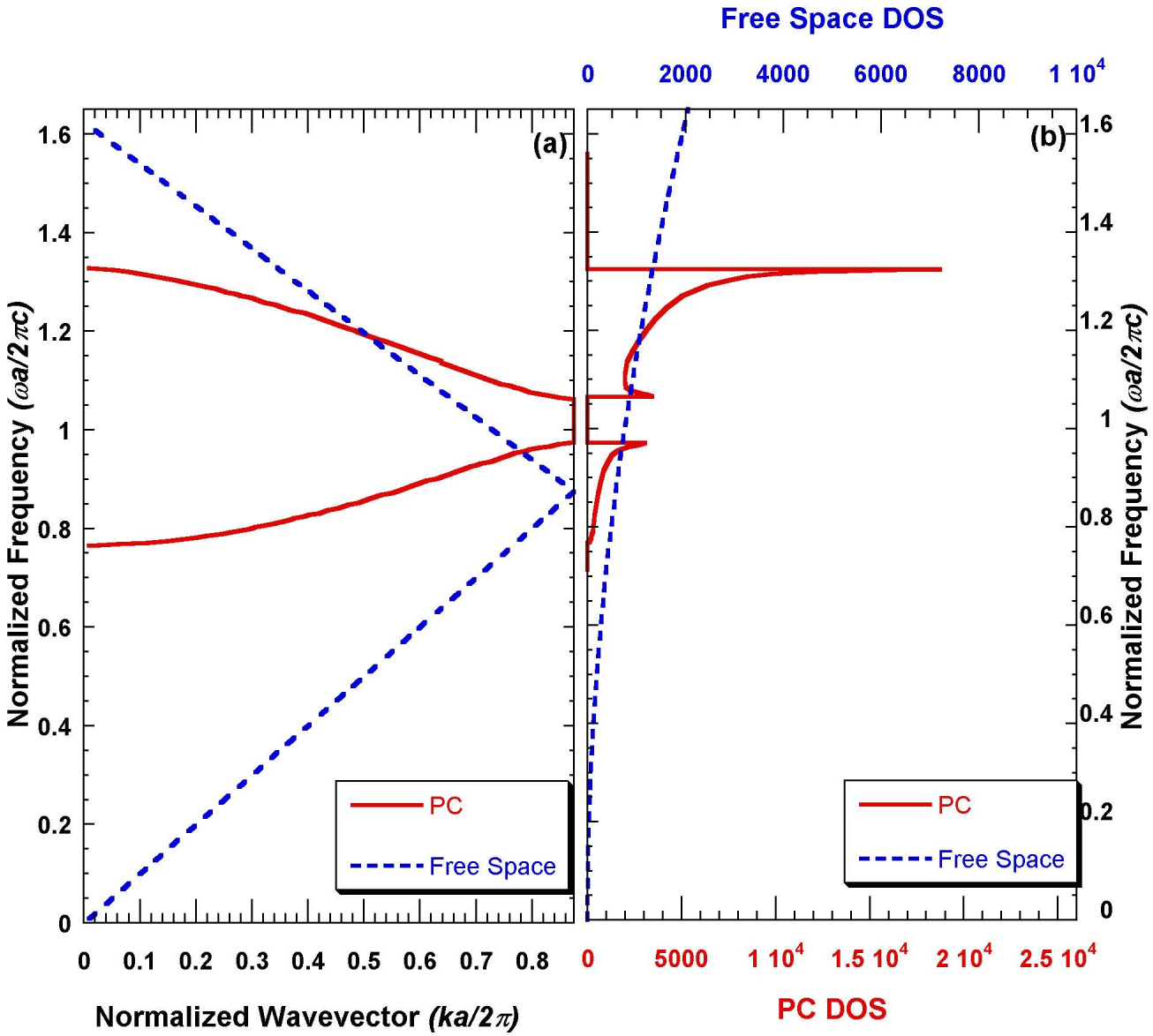
Free Space DOS
0
2000
4000
6000
8000
1 10^4
(a)
(b)
1.6
1.4
1.2
1
0.8
0.6
0.4
0.2
0
Normalized Frequency (ωa/2πc)
PC
Free Space
0
0.1
0.2
0.3
0.4
0.5
0.6
0.7
0.8
Normalized Wavevector (ka/2π)
5000
1 10^4
1.5 10^4
2 10^4
2.5 10^4
PC DOS

Fig.1

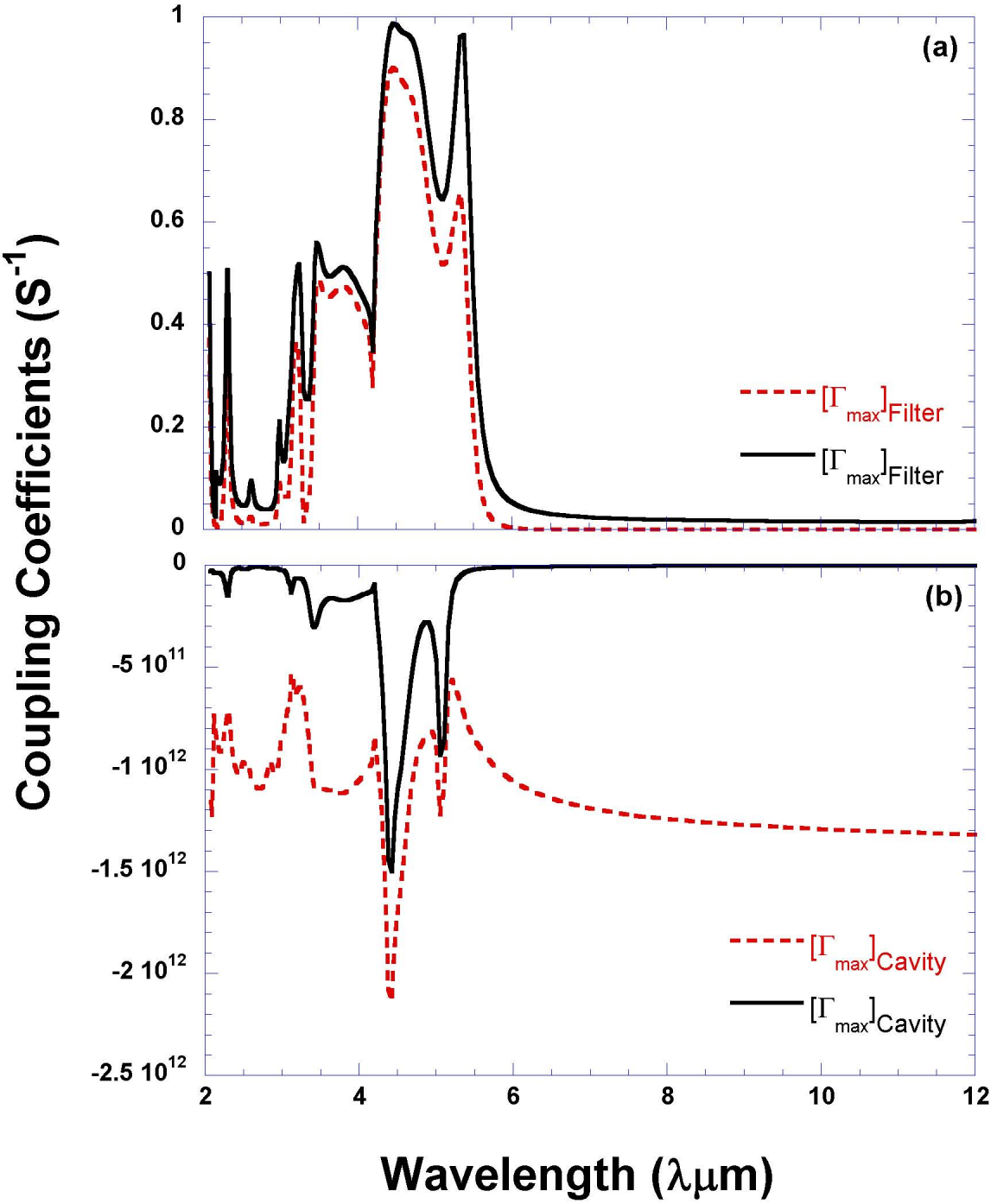
Coupling Coefficients (S^{-1})
(a)
(b)
$[\Gamma_{max}]_{Filter}$
$[\Gamma_{max}]_{Filter}$
$[\Gamma_{max}]_{Cavity}$
$[\Gamma_{max}]_{Cavity}$
1
0.8
0.6
0.4
0.2
0
-5 10^{11}
-1 10^{12}
-1.5 10^{12}
-2 10^{12}
-2.5 10^{12}
2
4
6
8
10
12
Wavelength ($\lambda\mu m$)

Fig.2

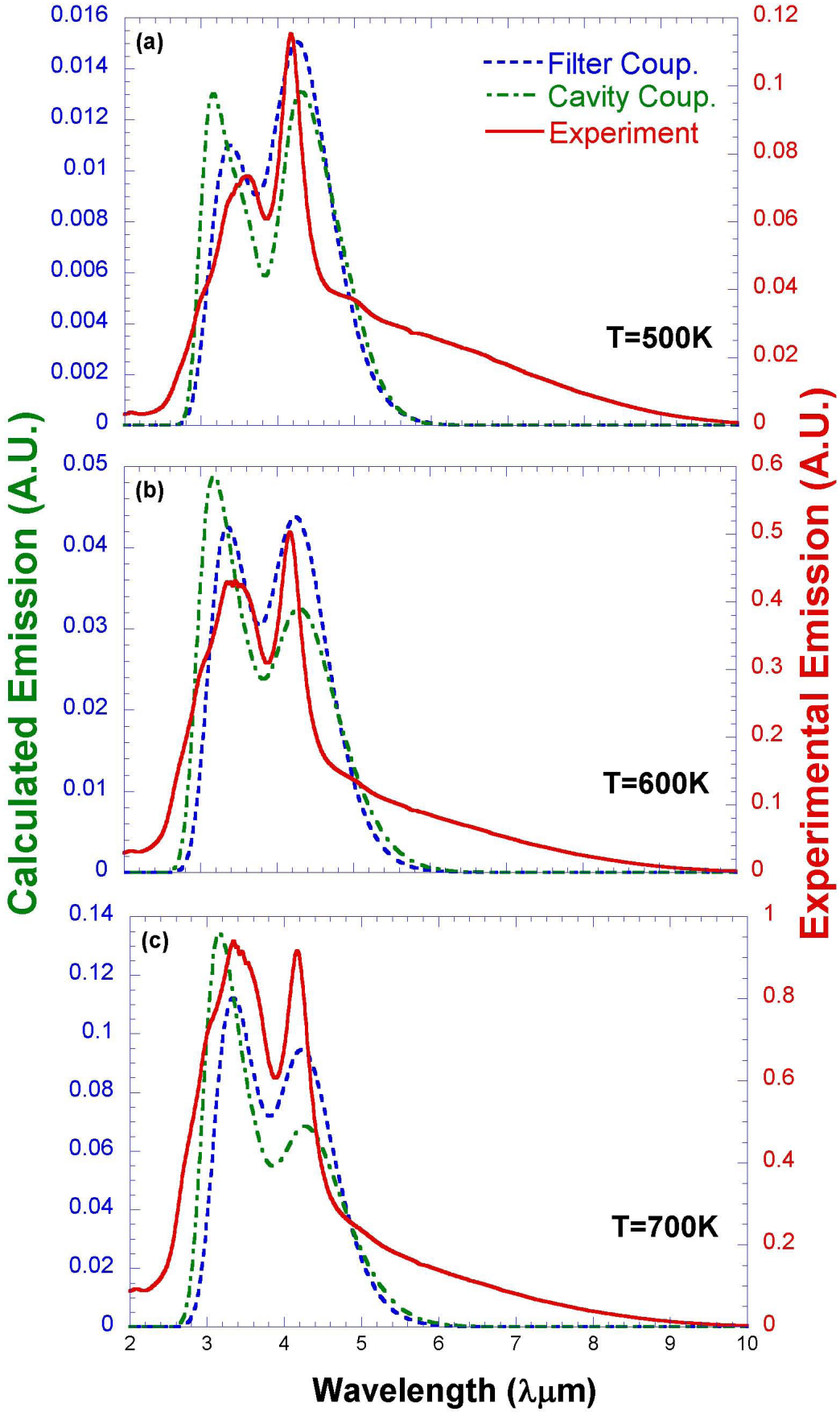
(a)
Filter Coup.
Cavity Coup.
Experiment
T=500K
(b)
T=600K
(c)
T=700K
Calculated Emission (A.U.)
Experimental Emission (A.U.)
Wavelength (λμm)
0.016
0.014
0.012
0.01
0.008
0.006
0.004
0.002
0
0.12
0.1
0.08
0.06
0.04
0.02
0
0.05
0.04
0.03
0.02
0.01
0
0.6
0.5
0.4
0.3
0.2
0.1
0
0.14
0.12
0.1
0.08
0.06
0.04
0.02
0
1
0.8
0.6
0.4
0.2
0
2
3
4
5
6
7
8
9
10

Fig. 3

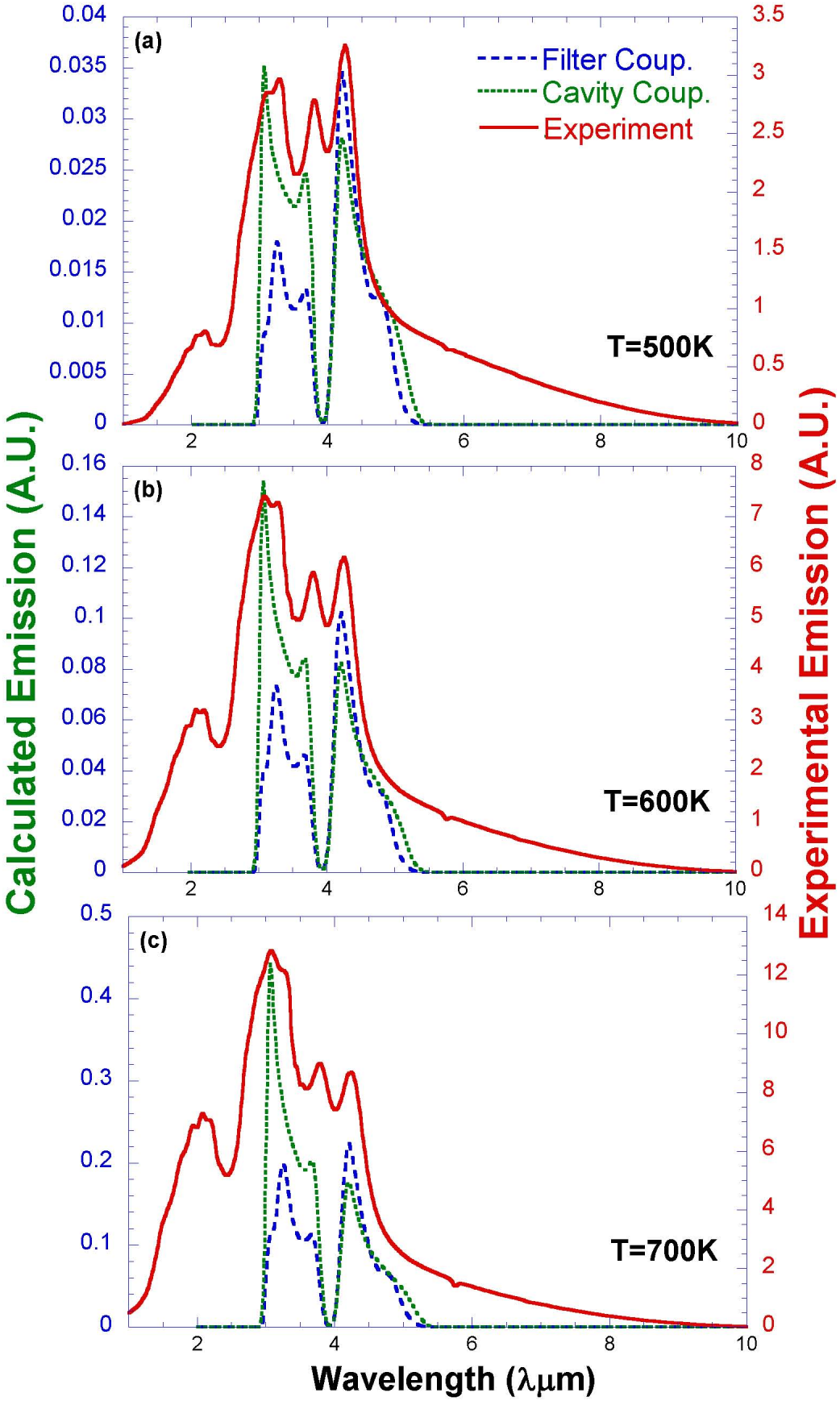
(a)
Filter Coup.
Cavity Coup.
Experiment
T=500K
(b)
T=600K
(c)
T=700K
Calculated Emission (A.U.)
Experimental Emission (A.U.)
Wavelength (λμm)

Fig.4

Emission from an active photonic crystal

I. El-Kady, W. W. Chow, and J. G. Fleming
Sandia National Laboratories, P.O. Box 5800, Albuquerque, New Mexico 87185-0601, USA
(Received 19 September 2005)

We investigated theoretically the emission from an active photonic crystal. Redistribution of photon density of states by a photonic lattice was found to greatly influence the thermal emission spectrum, resulting in substantial deviation from the Planck distribution. The calculation predicts that the photonic lattice intensity may exceed that of a blackbody source within certain spectral regions. However, the excess emission may be lost in practice because of nonradiative losses and photonic lattice inhomogeneities.

DOI: XXXX PACS number(s): 42.70.Qs, 42.55.Tv, 44.40.+a, 78.67.Hc

I. INTRODUCTION

In the presence of a photonic crystal host, a multitude of novel optical phenomena arise because of two main features of a photonic lattice band structure: suppression of photon density of states along certain crystallographic directions and propagation of selected Bloch-modes as mandated by translational symmetry. Examples of novel phenomena include, inhibition of spontaneous emission,[1,2] reduced group velocity,[3] exceedingly high cavity-Q factors,[4] low threshold lasing,[5] and modified emission characteristics.[6,7] This paper focuses on the last phenomenon, where it was shown that a dielectric photonic crystal can funnel thermal radiation into narrow radiation bands.[7] While there are theoretical and experimental results indicating exceedingly high intensities at the photonic lattice band edge, the question of whether these intensities exceed those of a blackbody at the same temperature and wavelength is unresolved.[6,8,9] An answer is important for scientific understanding and engineering development of a new generation of optical sources and detectors whose properties may go beyond the standard quantum limits. A problem with arriving at an answer experimentally is the difficulty in ensuring that the comparison is made under the same conditions.

The aim of this study is to address the question of thermal radiation from photonic lattices theoretically. Our approach begins with a first-principles calculation of the photonic lattice band structure. The results are used in a model of an active photonic crystal consisting of an inhomogeneously broadened ensemble of two-level systems interacting with a quantized multimode radiation field, whose modal properties are determined by the photonic lattice band structure.[10] The composite system is excited by an external pump and allowed to equilibrate with a thermal bath via collisions.

Section II describes the theoretical model, where approximations are made to facilitate the comparison of photonic crystal and blackbody emissions. Results are presented in Sec. III for the limiting cases determined by experimental conditions. To evaluate the model, we show that it retrieves Planck's blackbody distribution in the absence of a photonic crystal, and that the emission peak wavelengths and relative intensities are consistent with experimental values obtained for a lattice subjected to similar conditions.

II. THEORY

In formulating the problem, we label each two-level system with n, so that $|a_n\rangle$ and $|b_n\rangle$ are the ground and excited states, respectively, that are separated by energy $\hbar\omega_n$. Correspondingly, each radiation field mode has energy $\hbar\Omega_k$, and is described by creation and annihilation operators $a_k^\dagger$ and a_k, respectively. The relation between Ω_k and k depends on the photonic lattice structure. The Hamiltonian for the combined matter and radiation field system is[10,11]

$$H = \sum_n \hbar\omega_n |b_n\rangle\langle b_n| + \sum_k \hbar\Omega_k a_k^\dagger a_k - \sum_{k,n} g_k(|b_n\rangle\langle a_n| a_k + a_k^\dagger |a_n\rangle\langle b_n|), \quad (1)$$

where the dipole interaction is assumed, with

$$g_k = \mu\sqrt{\frac{\hbar\Omega_k}{\varepsilon_0 V}}, \quad (2)$$

μ is the dipole matrix element, ε_0 is the permittivity in vacuum, and V is the system volume. Introducing the operators for the microscopic polarization amplitude $\sigma_n^\dagger A_k \equiv |b_n\rangle\langle a_n| a_k \exp[-i(\omega_n - \Omega_k)t]$, the excited and ground state populations, $\sigma_{an} \equiv |a_n\rangle\langle a_n|$ and $\sigma_{bn} \equiv |b_n\rangle\langle b_n|$, respectively, and working in the Heisenberg picture, we derive

$$\frac{d\sigma_n^\dagger A_k}{dt} = \frac{i}{\hbar}\sum_{k'} g_{k'}(\sigma_{bn} A_k A_{k'}^\dagger - A_{k'}^\dagger A_k \sigma_{an}) e^{-i(\omega_n - \Omega_{k'})t}, \quad (3)$$

$$\frac{d\sigma_{an}}{dt} = \frac{i}{\hbar}\sum_k g_k(A_k^\dagger \sigma_n e^{-i(\omega_n - \Omega_{k'})t} - \sigma_n^\dagger A_k e^{i(\omega_n - \Omega_{k'})t}), \quad (4)$$

$$\frac{d\sigma_{bn}}{dt} = -\frac{i}{\hbar}\sum_k g_k(A_k^\dagger \sigma_n e^{-i(\omega_n - \Omega_{k'})t} - \sigma_n^\dagger A_k e^{i(\omega_n - \Omega_{k'})t}). \quad (5)$$

Additionally, the photon number operator obeys,

$$\frac{dA_k^\dagger A_k}{dt} = \frac{i}{\hbar}\sum_n g_k[A_k^\dagger \sigma_n e^{-i(\omega_n - \Omega_k)t} - \sigma_n^\dagger A_k e^{i(\omega_n - \Omega_k)t}]. \quad (6)$$

Assuming that the polarization dephasing rate γ is much faster than the time variations in the active medium and photon populations, one may adiabatically eliminate the polarization equation. Then, introducing the expectation values $n(\Omega, t) = \langle A_k^\dagger(t) A_k(t)\rangle$, $n_a(\omega_n, t) = \langle \sigma_{an}(t)\rangle$ and $n_b(\omega_n, t) = \langle \sigma_{bn}(t)\rangle$, we obtain the working equations for our analysis,

$$\frac{dn_a(\omega_n,t)}{dt} = \frac{2\pi}{\hbar^2}\rho(\omega_n)g(\omega_n)^2\{[n_b(\omega_n,t) - n_a(\omega_n,t)]n(\omega_n,t) + n_b(\omega_n)\} - \gamma_r[n_a(\omega_n,t) - f_a(\omega_n,t)] - \Lambda(\omega_n)n_a(\omega_n,t), \quad (7)$$

$$\frac{dn_b(\omega_n,t)}{dt} = -\frac{2\pi}{\hbar^2}\rho(\omega_n)g(\omega_n)^2\{[n_b(\omega_n,t) - n_a(\omega_n,t)]n(\omega_n,t) + n_b(\omega_n)\} - \gamma_r[n_b(\omega_n,t) - f_b(\omega_n,T)] + \Lambda(\omega_n)n_a(\omega_n,t), \quad (8)$$

$$\frac{dn(\Omega,t)}{dt} = \frac{2}{\hbar^2}g(\Omega)^2\sum_n \frac{\gamma}{(\omega_n-\Omega)^2+\gamma^2}\{[n_b(\omega_n,t) - n_a(\omega_n,t)]n(\Omega,t) + n_b(\omega_n,t)\} - \gamma_c n(\Omega,t), \quad (9)$$

where $\rho(\Omega)$ is the photonic-lattice density of states, which is assumed to be spherically symmetric. Additionally, the pump and decay contributions are included phenomenologically, where γ_c is the photon decay rate,

$$\Lambda(\omega_n) = \Lambda_0 \exp\left(-\frac{\hbar\omega_n}{k_B T_p}\right) \quad (10)$$

is the pump rate, and γ_r is the effective rate for the actual populations n_a and n_b to relax to the equilibrium distributions

$$f_a(\omega_n,T) = Z_o, \quad (11)$$

$$f_b(\omega_n,T) = Z_o \exp\left(\frac{-\hbar\omega_n}{k_B T}\right), \quad (12)$$

where Z_o is the thermodynamic partition function that is determined by the total number of two-level systems $N_o = \Sigma_n[f_a(\omega_n)+f_b(\omega_n)]$, T_p and T are the pump and reservoir temperatures. Solving Eqs. (7)–(9) gives the photon population inside the photonic lattice.

To relate to experiments, it is necessary to obtain the emission outside the photonic lattice. Theoretically, this is a nontrivial step because in our attempt to properly treat the active medium and its emission physics with a quantum theory, we relied on orthonormal optical modes for an infinite photonic lattice. This is very similar to a long-standing problem in laser theory.[12] There, one circumvents the issue by beginning with the Fox-Li modes for a Fabry-Perot cavity with perfectly reflecting mirrors, and then introducing a loss mechanism to represent the outcoupling.[13,14] Following this approach, we use the steady state solutions $n(\Omega,t) \rightarrow n(\Omega)$ in

$$u(\lambda) = \Gamma(\lambda)\frac{d\Omega}{d\lambda}\hbar\Omega_\rho(\Omega)n(\Omega) \quad (13)$$

to obtain the emission wavelength spectrum outside the photonic lattice enclosure, where

$$\Gamma(\lambda) = 1 - [R(\lambda) + A(\lambda)] \quad (14)$$

is the coupling factor describing the efficiency with which radiation inside the photonic crystal is coupled to the outside, $R(\lambda)$ is the reflectivity, $A(\lambda)$ is the absorption. The determination of $R(\lambda)$ and $A(\lambda)$ is described in the following section.

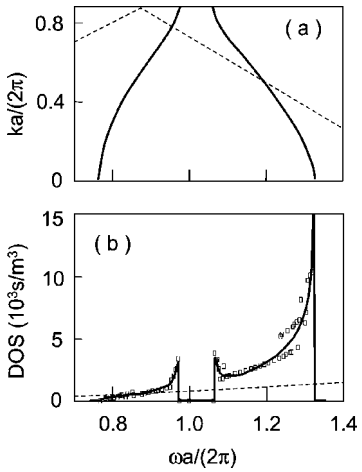

FIG. 1. (a) Calculated photonic-crystal (solid curve) and free-space (dashed curve) dispersions. (b) Densities of states computed from the photonic-crystal (dots) and free-space (dashed curves) dispersions in (a). The solid line is the least-squares fit to the dots.

III. RESULTS

In this study, we consider a tungsten Lincoln-log photonic crystal with 28.5% filling fraction and square cross-section rods. A coupled-wave method is used to compute the band structure, where the fields and dielectric functions are expanded in terms of plane waves. Maxwell's equations are cast in an eigen problem format in Fourier space and solved using a transfer matrix approach by treating each layer of the structure as an independent 2D Limilar grating. Details of this method and its accuracy in describing our structure are discussed elsewhere.[15] The reflectivity $R(\lambda)$ and absorption $A(\lambda)$ are obtained by an independent frequency domain transfer matrix calculation performed on six layers of the photonic crystal structure.[16]

Figure 1(a) shows the photonic-lattice dispersion in the (001) crystallographic direction (solid curve). Clearly visible are the fundamental and first higher order gaps, as well as the significant flattering of the dispersion at the band edges due to anticrossing. The dots in Fig. 1(b) give the density of states (DOS) $\rho(\omega)$ computed from the dispersion, assuming spherical symmetry. Note the drastic increases in DOS as the photonic crystal dispersion flattens at the band edges. For comparison, Fig. 1 also shows the free-space dispersion and DOS (dashed curves).

Using the photonic-crystal DOS in Fig. 1(b), Eqs. (7)–(9) are solved numerically with a fourth-order Runge-Kutta finite difference method. Following previous comparisons of photonic crystal and blackbody emissions, we ensure that the steady-steady active-medium populations $n_a(\omega_n)$ and $n_b(\omega_n)$ are to a good approximation given by the equilibrium distributions $f_a(\omega_n,T)$ and $f_a(\omega_n,T)$ by performing the calculations for low excitation and rapid relaxation conditions, specifically, with $\gamma = 10^{14}$ s^{-1}, $\gamma_r = 10^{12}$ s^{-1}, and $\gamma_c = \Lambda_0 = 10^9$ s^{-1}. Furthermore, we choose $\mu = e \times 0.5$ nm, $V = 10^{-18}$ m^{-3}, $N_0 = 200$ and $T_p = T$. The steady-state solutions to Eqs. (7)–(9),

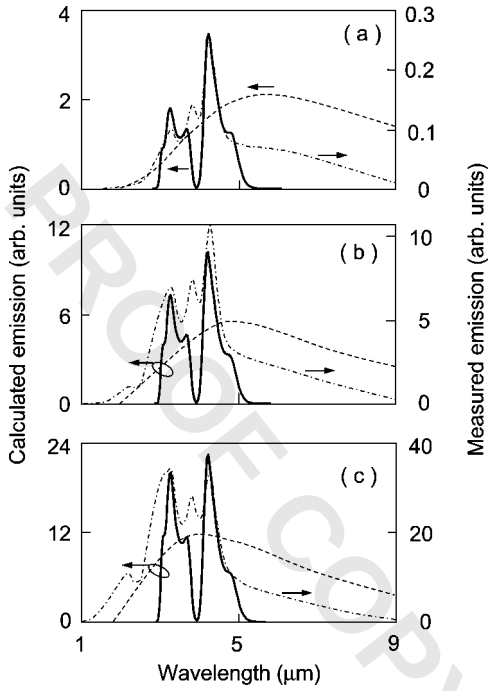

FIG. 2. Calculated blackbody (dashed curve) and lossless photonic-crystal (solid curve) emission spectra for $T=$(a) 500 K, (b) 600 K, and (c) 700 K. The dotted-dashed curves are the experimental spectra.

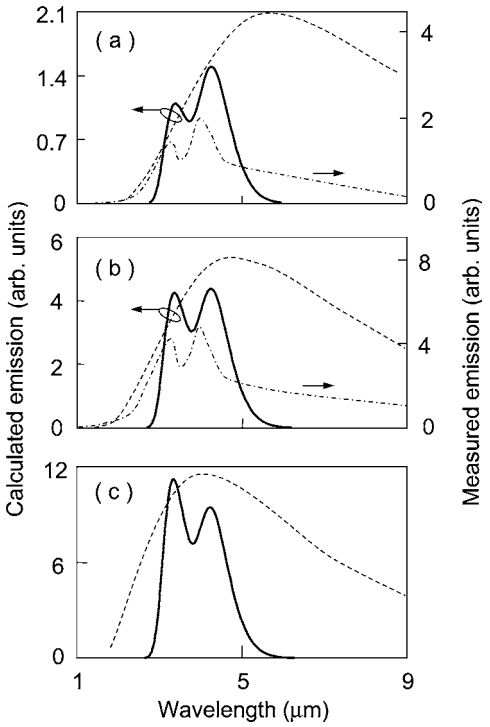

FIG. 3. Calculated blackbody (dashed curve) and lossy photonic-crystal (solid curve) emission spectra for $T=$(a) 500 K, (b) 600 K, and (c) 700 K. The dotted-dashed curves are the experimental spectra.

are used in Eq. (13), with two limits (as discussed in the next two paragraphs) to the transmission function, to obtain the emission spectrum. For the corresponding blackbody emission, we repeat the procedure with $\rho(\omega)$ replaced by the free-space DOS and with $\Gamma(\lambda)=1$.

The coupling factor depends on experimentally imposed boundary conditions. To estimate the upper emission limit, we consider the best-case scenario of negligible nonradiative losses, so that every photon absorbed by the photonic lattice structure is eventually remitted into a propagating Bloch-mode. We approximate this situation with a maximum coupling factor of $\Gamma_{max}(\lambda)=1-R(\lambda)$. The solid curves in Fig. 2 show the calculated photonic-crystal emission spectra for this optimal situation at different temperatures. Also plotted are the corresponding blackbody spectra (dashed curves). The figure clearly shows the suppression of photonic lattice emission intensity at the photonic band gaps. More importantly, they indicate a significant increase in intensity at the band edges.

Figure 2 also depicts (with a different vertical scale) the experimentally measured spectra (dotted-dashed curves) for a 6 layer tungsten Lincoln-log structure suspended in vacuum by wires. Nonradiative losses are minimized by having an essentially free-standing structure. The experimental structure was electrically excited by Joule heating. To determine the temperature, the experiment was repeated with blackbody paint coating the central region of the crystal, which then acted as the heating element. Since the blackbody paint behaved essentially as a perfect electrical insulator, it did not change the electrical conductivity of the sample. The temperature was deduced by matching the change in electrical resistivity of the photonic crystal in the two experiments, and using Wein's law for the relationship between temperature and blackbody emission peak. The solid and dotted-dashed curves show relatively good agreement between calculation and experiment in terms of the wavelength and relative magnitude of the intensity peaks. Inhomogeneous broadening is included in the calculation to account for crystal imperfections. A 5 meV broadening is chosen to match the linewidths of the experimental spectra. Comparison of absolute intensity is not possible because of experimental calibration difficulties. The experimental emission peak at ~ 2 μm is absent in the calculated results because the band-structure calculation was terminated at the edge of the second band at ~ 3 μm.

To obtain a lower bound for the photonic-crystal emission, we consider the worst-case scenario where all the photons absorbed by the photonic lattice structure is lost nonradiatively. To approximate this situation, we use a minimum coupling function of $\Gamma_{min}(\lambda)=1-R(\lambda)-A(\lambda)$, where $A(\lambda)$ is calculated using the complex dielectric constant for tungsten.[17] The solid curves in Fig. 3 for the calculated emission spectra at different temperatures, show that for the most part, photonic-crystal emission is at or slightly below the blackbody emission (dashed curves). Comparison with the solid curves in Fig. 2 reveals noticeable spectral shape differences, that are also observed in experiments (compared dotted-dashed curves in Figs. 2 and 3). For the lossy case, the measurements were made with a photonic crystal that is similar to the one used in Fig. 2, but mounted on a heat sink which serves as a channel for nonradiative losses. An inho-

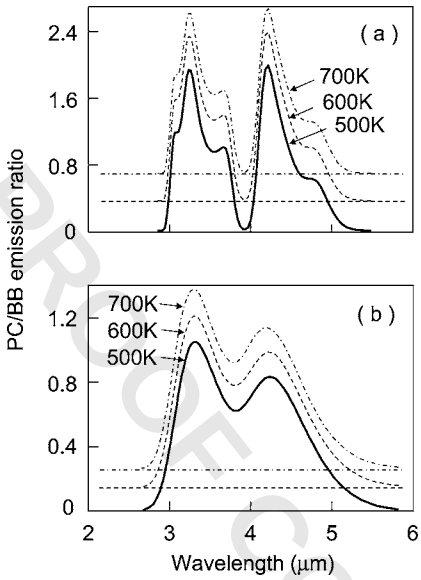

FIG. 4. Ratio of photonic crystal emission to blackbody emission for (a) lossless and (b) lossy cases at different temperatures.

mogeneous broadening of 20 meV is used in the calculation to match the experimental linewidths. The general agreement between theory and experiment provides some assurance of the accuracy of the transmission coupling functions used in the study.

Figures 4(a) and 4(b) are plots of the ratio between photonic-lattice and blackbody emission for the lossless and lossy cases. In both cases, the curves (displaced vertically for clarity) show the independence of the ratio on temperature, indicating that modifications to the emission by the photon lattice under low excitation and rapid equilibration conditions arise mainly from changes in the photon density of states. Therefore, it is unnecessary to excite an active photon-crystal structure to an extreme temperature to see the predicted effects.

Lastly, we note that inhomogeneous broadening plays an important role in determining the shape and amplitude of the photonic-crystal spectrum. This is the case because of the sharpness of the emission peaks in both lossless and lossy structures. Figure 5 illustrates the dependence of the lossy photonic-crystal spectrum on inhomogeneous broadening. Figures 5(a) and 5(b) show that greater than one photonic-crystal to blackbody intensity ratio is possible even in the lossy structure for inhomogeneously broadening of up to 10 meV. However, when both absorption losses and structural aperiodicities are present the photonic-crystal emission peaks are likely to no longer exceed the blackbody emission, as shown in Fig. 5(c).

IV. CONCLUSION

In summary, the emission from an active photonic-lattice crystal is investigated using a model consisting of an inhomogeneously broadened ensemble of two-level systems interacting with a quantized radiation field whose modal properties are determined by the photonic-lattice band structure.

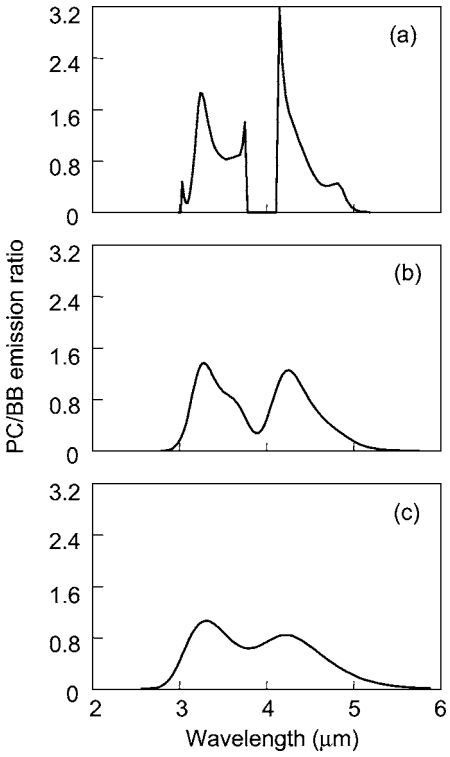

FIG. 5. Ratio of photonic crystal emission to blackbody emission for the lossy case and inhomogeneously broadening of (a) 0, (b) 10, and (c) 20 meV.

The model gives the emission spectra for arbitrary photonic-lattice configurations, and reproduces Planck's radiation formula for thermal emission into free space. Comparison of photonic-lattice and blackbody emission shows appreciable modification of the blackbody spectrum by the photonic lattice, where the redistribution of the photonic density of states results in suppression of emission at certain wavelengths and enhancement at others. Under low excitation and rapid relaxation conditions, the enhancement can give rise to exceedingly high emission peaks at the photonic lattice band edges, with peak intensities exceeding those of a blackbody at the same temperature and wavelength. However, imperfections, such as those resulting in inhomogeneous broadening, absorption and diffraction losses, can negate the excess emission. Our comparison is between an isolated active photonic crystal system and an isolated blackbody system. The results do not apply to situations involving the coupling of the two systems.[9] There, the interaction between the photonic crystal and blackbody (e.g., leading to population distribution changes) should be taken into account. Finally, the parameter space explored excludes situations involving nonequilibrium population effects, even though these effects can be treated within the framework of the present model.

ACKNOWLEDGMENTS

This work was supported by the U. S. Department of Energy under Contract No. DE-AC04-94AL85000 and the Forschungspreise from the Alexander von Humboldt Foundation.

[1] E. Yablonovitch, Phys. Rev. Lett. **58**, 2059 (1987).
[2] S. John and J. Wang, Phys. Rev. Lett. **64**, 2418 (1990).
[3] S. John and J. Wang, Phys. Rev. B **43**, 12772 (1991).
[4] G. Subramania, S. Y. Lin, J. R. Wendt, and J. M. Rivera, Appl. Phys. Lett. **83**, 4491 (2003).
[5] O. Painter, R. K. Lee, A. Scherer, A. Yariv, J. D. O'Brien, P. D. Dapkus, and I. Kim, Science **284**, 1819 (1999).
[6] C. M. Cornelius and J. P. Dowling, Phys. Rev. A **59**, 4736 (1999).
[7] S. Y. Lin, J. G. Fleming, E. Chow, J. Bur, K. K. Choi, and A. Goldberg, Phys. Rev. B **62**, R2243 (2000).
[8] J. G. Fleming, S. Y. Lin, and I. El-Kady, Appl. Phys. Lett. **83**, 593 (2003).
[9] T. Trupke, P. Würfel, and M. A. Green, Appl. Phys. Lett. **84**, 1997 (2004).
[10] N. Vats, S. John, and K. Busch, Phys. Rev. A **65**, 043808 (2002).
[11] M. O. Scully and M. S. Zubairy, *Quantum Optics* (Cambridge University Press, Cambridge, 1977).
[12] For a textbook discussion see A. E. Siegman, *Lasers* (University Science Books, Mill Valley, 1986), Chap. 24.
[13] W. E. Lamb, Jr., Phys. Rev. **134**, A1429 (1964).
[14] M. Sargent, III, M. O. Scully, and W. E. Lamb, Jr., *Laser Physics* (Addison-Wesley, Reading, 1974).
[15] L-L. Lin, Z.-Y. Li, and K.-M. Ho, J. Appl. Phys. **94**, 811 (2003).
[16] Z.-Y. Li and K.-M. Ho, Phys. Rev. B **67**, 165104 (2003).
[17] D. R. Lide, *Handbook of Chemistry and Physics*, 83rd ed. (CRC Press, Boca Raton, 2003).

PROOF COPY [LX9055B] 032543PRB

Experimental observation of photonic-crystal emission near a photonic band edge

Shawn-Yu Lin,[a] J. G. Fleming, and I. El-Kady
MS 0603, Sandia National Laboratories, P.O. Box 5800, Albuquerque, New Mexico 87185

(Received 28 March 2003; accepted 23 May 2003)

A three-dimensional tungsten photonic crystal is realized with a photonic band edge at $\lambda \sim 4$ μm wavelength. Its thermal emission is suppressed in the band gap regime and, at the same time, exhibits sharp peaks near the band edge. It is further observed that energy conversion efficiency from one side of the sample reaches $\eta \sim 40\%$. This finding is attributed to a complete metallic photonic band gap in the infrared ($\lambda \geqslant 6$ μm) and the enhanced density of photon states near the band edge of our tungsten photonic crystal. © *2003 American Institute of Physics.*
[DOI: 10.1063/1.1594263]

It has been suggested that a photonic-crystal (PBG) structure may be utilized to modify a thermal emission spectrum.[1–3] The first experiment was carried out by Lin *et al.* by using a combination of a heated silicon substrate and a three-dimensional (3D) silicon photonic crystal.[2] The resulting thermal emission was shown to be suppressed in the photonic band gap and enhanced slightly by ~30% near the band edge.[2] However, it remains unresolved whether the emission originates from the thick silicon substrate (~500 μm) or from the silicon photonic crystal itself. To observe intrinsic PBG emission, it is essential to fabricate a sample with no substrate attached to it. In this letter, a 3D tungsten photonic crystal is realized with a large infrared band gap ($\lambda \geqslant 6$ μm). The tungsten PBG sample is a freely standing thin film and, therefore, its emission should reflect the intrinsic photonic-crystal emission. It is experimentally observed that the emission exhibits a narrow spectral linewidth near the photonic band edge at $\lambda \approx 3.5$–4.5 μm. It is further shown that the electric-to-optical energy conversion efficiency from one side of the tungsten PBG sample reaches $\eta \sim 40\%$.

The 3D tungsten photonic-crystal sample is fabricated using a modified silicon process.[4] In the first step, a layer of silicon dioxide is deposited, patterned, and etched to create a mold. The mold is then filled with a tungsten film. The structure is then planarized using a chemical-mechanical-polishing process. The same process is repeated for several times. At the end of the process the silicon dioxide is released from the substrate and the sample is a freely standing thin film, ~4–5 μm thick. The photograph of five pieces of our sample is shown in Fig. 1(a). The different colors are due to diffraction of the camera's flashlight. In Fig. 1(b), a scanning electron microscopy (SEM) image of a five-layer 3D tungsten photonic-crystal sample is shown. It consists of layers of one-dimensional tungsten rods with a stacking sequence that repeats itself every four layers, that is, a unit cell.[4,5]

In Fig. 2(a), the measured reflection (black color) and absorption (blue color) spectra from five-layer tungsten PBG sample are shown, respectively. Light propagates along the $\langle 001 \rangle$ direction of the crystal and is unpolarized. The reflectance exhibits oscillations for $2 \leqslant \lambda \leqslant 4$ μm (the allowed band), increases sharply at $\lambda = 4$–5 μm (the photonic band edge) and reaches a high reflectance of 90% for $\lambda \geqslant 6$ μm (the photonic band gap). Such a 3D metallic photonic band gap is a complete gap and is effective (~30 dB/unit cell) in trapping light fully in all 4π solid angles and for both polarizations.[3] It is also noted that as light propagates away from the surface normal ($\theta = 0°$), the band edge shifts to longer wavelength and band edge reflectance does not rise as sharply, i.e., a larger $d\omega/dk$.[3] The absorptance is low ($\leqslant 3\%$) in the band gap and exhibits three strong peaks ($\geqslant 30\%$) near the band edge at $\lambda \approx 4$ μm. The three peaks occur at $\lambda = 3.5$, 4, and 4.5 μm, respectively, which agree with results of our model calculation. The peak absorption is about ten times stronger than tungsten's intrinsic absorption (2%–3%). This enhancement is due to a longer light-matter interaction time near the band edge, or equivalently, an enhanced density of photon states.[6–10] The selective absorption enhancement near the band edge suggests the possibility of achieving enhanced light emission at a narrow band.[11,12]

To achieve emission, the sample is biased by applying a voltage across the PBG sample and is heated through Joule heating. As the sample is operated at high temperatures, it is mounted to be thermally isolated from its surroundings. To minimize thermal loss, the sample is placed in a vacuum chamber pumped to $\sim 10^{-3}$ Torr. For power density measurements, a commercially available power meter, calibrated to better than 5%, is used. As our PBG sample is very thin, only 4–5 μm, it is experimentally difficult to attach a thermal sensor to the sample. Instead, the sample temperature is determined from its resistivity, which depends on temperature linearly for $T = 300$–800 K.[13] The measured temperature is an effective temperature $\langle T \rangle$, averaged over the entire sample, and has an uncertainty of $\Delta T/T \leqslant 8\%$.

In Fig. 2(b), the measured emission spectra at low biases ($V < 0.20$ V) are shown. The measurements are performed using a standard Fourier-transform infrared spectrometer from $\lambda = 1$–20 μm.[4,14] The measured spectrum consists of a broad emission at $\lambda \approx 8$–10 μm and three sharp peaks. At $V = 0$ V, the broad emission has a maximum at $\lambda \sim 10$ μm and

[a]Electronic mail: slin@sandia.gov

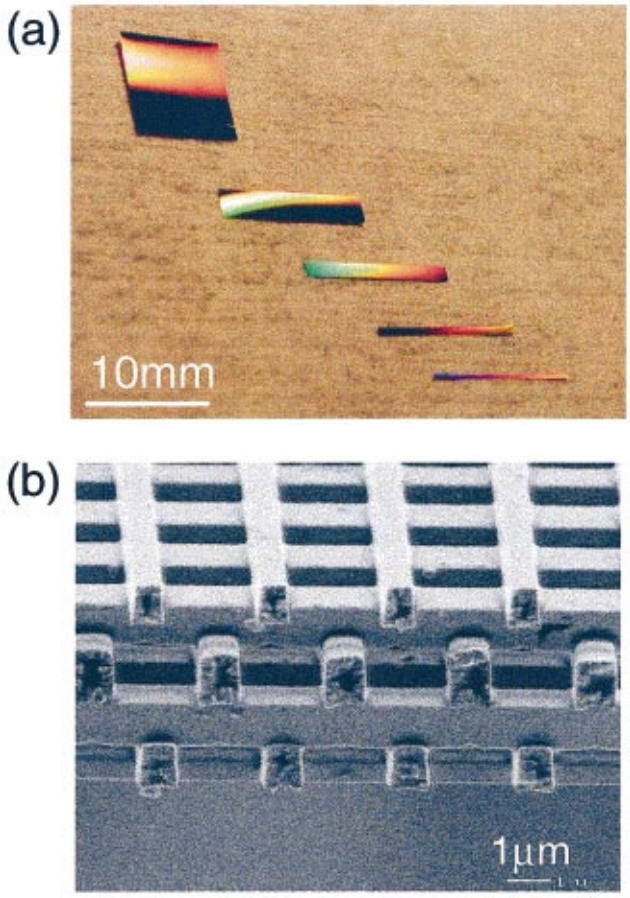

FIG. 1. (Color) (a) Photographs of representative 3D tungsten photonic-crystal samples. The samples are freely standing sheets. The different colors are due to diffraction of a camera's flashlight. (b) SEM side-view image of the tungsten photonic-crystal sample. The rod width is 0.85 μm, rod-to-rod spacing is 2.8 μm, and the filling fraction of the high index material is 30%.

persists even when spectrometer entrance is blocked with a mirror. It is attributed to background emission from the spectrometer. As V is increased to 0.20 V, the broad emission increases gradually in amplitude and shifts slightly to shorter wavelengths (indicated by red bars). As the background emission from the spectrometer is V independent, the slight increment part of the broad emission is from the heated sample. This V-dependent broad emission may originate from the sample's surface layer where it would experience little photonic band gap effect. The broad peak position also agrees with that predicted from the Wien's Displacement Law: $\lambda \times T \cong 2898$ [μm K].[15] The broad peak thus behaves like a gray-body radiation.

As V is increased, three distinct emission peaks appear at $\lambda = 3.5$, 4, and 4.5 μm, respectively. All three peaks increase at a much faster rate than the broad one and are pinned at the same wavelengths (indicated by dash lines) as V is increased. Moreover, the peak positions agree with that of the band-edge absorption within ± 0.1 μm [Fig. 2(a)]. This excellent agreement indicates that the peak emission is due to photonic crystal band edge effect. At the band edge of larger θ, the larger $d\omega/dk$ implies a smaller $D(\omega)$ and therefore less emission enhancement is observed at longer wavelength than $\lambda \approx 4.5$ μm. The evolution of the sharp peaks is further explored by increasing the voltage bias from $V = 0.2$ to 0.6 V. Or, equivalently, the input power is increased from

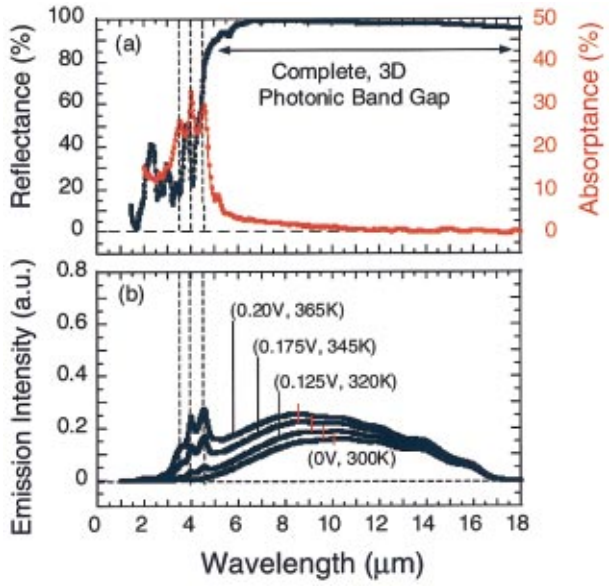

FIG. 2. (Color) (a) The measured reflection (black curve) and absorption (red curve) spectra for a five-layer tungsten photonic crystal. The reflectance exhibits oscillations for $2 < \lambda < 4$ μm (the allowed band), raises sharply at $\lambda = 4$–5 μm (the band edge) and reaches a high reflectance of 90% for $\lambda > 6$ μm (the band gap). Three strong absorption peaks ($\sim$30%) are observed near the photonic band edge, $\lambda = 3.5$–4.5 μm. (b) The measured emission spectra for the tungsten photonic-crystal sample at low biases ($V \leqslant 0.2$ V). As V is increased to 0.20 V, the broad emission increases gradually in amplitude and shifts slightly to shorter wavelengths (indicated by red bars). Simultaneously, three distinct sharp peaks appear at $\lambda \sim 3.5$, 4, and 4.5 μm, respectively. All three sharp peaks increase at a much faster rate than that for the broad one. The sharp peaks are also pinned at the same wavelengths, independent of V.

$P_{\text{in}} = 85$ to 485 mW and the effective temperature from $\langle T \rangle = 360$ to 560 K. In Fig. 3, a series of representative emission spectra are shown. The three peaks continue to occur at the same wavelengths and increase at a fast rate. This fast increase is consistent with Bose–Einstein distribution, which

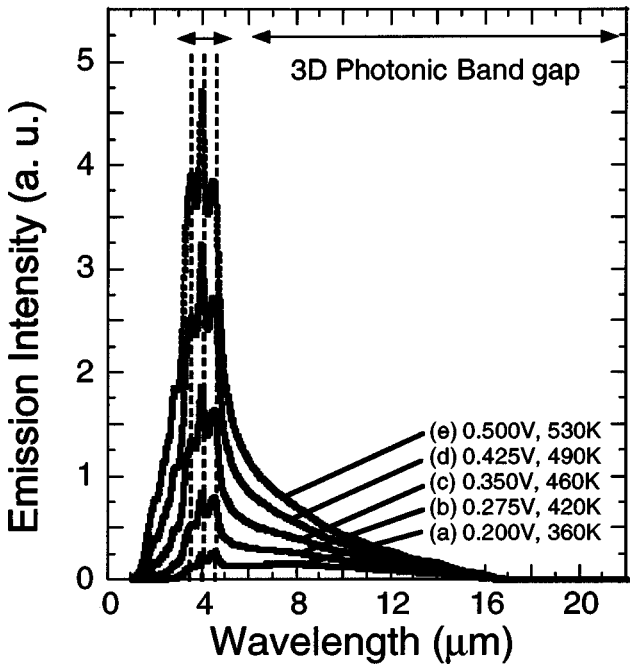

FIG. 3. A series of emission spectra taken at higher biases from $V = 0.2$ to 0.56 V. The three sharp peaks continue to occur at the same wavelengths and dominate the emission spectrum for $V > 0.275$ V.

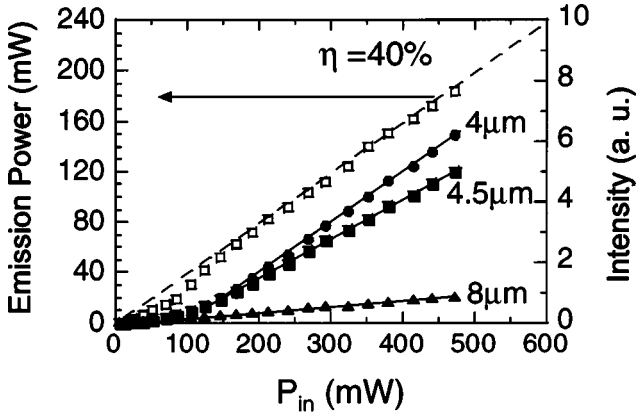

FIG. 4. The emission amplitudes are summarized as a function of P_{in} for $\lambda=4$ (solid circles), 4.5 (solid squares), and 8 μm (solid triangles), respectively. At high input powers ($P_{in}>150$ mW), the peak amplitudes at $\lambda=4$ and 4.5 μm scale linearly with P_{in}. The total emitted power (the open squares) also scales linearly with P_{in} at high input power and reaches a $\eta=40\%$ electric-to-radiation conversion efficiency (indicated by the dash line).

increases faster for shorter wavelengths as temperature is increased. For $V>0.275$ V, the sharp peaks dominate the emission spectrum and the broad emission at $\lambda=6-12$ μm becomes a weak shoulder. At $V=0.50$ V, or $\langle T\rangle=530$ K, the full width at half maximum (FWHM) of the spectrum is only $\Delta\lambda(\text{FWHM})\cong 2$ μm. For comparison purpose, a blackbody at $T=530$ K has a spectral width of $\Delta\lambda(\text{FWHM})\cong 6$ μm. This is reasonable as radiation from inside the PBG sample is suppressed by the complete band gap for $\lambda\geqslant 6$ μm, leading to a three-times linewidth narrowing. As the longer wavelength infrared radiation ($\lambda\geqslant 6$ μm) is significantly suppressed, the input thermal energy radiates into shorter wavelengths near the band edge of $\lambda=3-5$ μm.

In Fig. 4, the emission amplitudes are summarized as a function of P_{in} at $\lambda=4$, 4.5 μm (the sharp peaks) and $\lambda=8$ μm (the broad emission), respectively. At low input power, $P_{in}=100$ mW, the peak amplitude at $\lambda=4/4.5$ μm shows a superlinear behavior and is comparable to that at $\lambda=8$ μm. For $P_{in}\geqslant 150$ mW, the amplitudes at $\lambda=4/4.5$ μm far exceed that at $\lambda=8$ μm. Furthermore, the peak amplitude scales linearly with P_{in}. The linearity suggests a constant conversion of the input electric power into optical power at a narrow spectral band. To verify this point, the total emission power is measured and shown as open squares. Indeed, the emitted power scales linearly with P_{in} at high input power (indicated by the dash line) and reaches $\eta=40\%$ electric-to-radiation conversion efficiency. Taking into account radiation from the top and bottom emitting surfaces, the conversion efficiency is expected to be $\sim 80\%$. It is also noted that about half of the emission power is concentrated within the narrow spectral range of $\Delta\lambda(\text{FWHM})\cong 2$ μm. If we take the experimental solid angle, 1.8π steradiance, and account for the angular dependent reflection loss of the sample chamber window, we expect to gather no more than 45% from the top emitting surface. This is in reasonable agreement with our data, especially if we assume some power is conducted as heat down the supporting mount. Therefore, the PBG sample is at a steady state, where $\sim 10\%$ of its energy is dissipated as conduction loss and $\sim 90\%$ as radiation energy.

In summary, the complete 3D photonic band gap of our PBG sample is effective in suppressing the infrared part ($\lambda\geqslant 6$ μm) of the thermal radiation. At the same time, the enhanced photon-matter interaction near the band edge is effective in facilitating light emission. The end result is the dominance of light emission at a narrow band with a constant energy conversion. The combined modification of photon-matter interaction at the photonic band gap and near the band edge is essential to achieving this result.

The authors thank Dr. K. M. Ho of Iowa State University for valuable discussion. The authors also acknowledge J. Bur, J. Rivera, M. Tuck, and the Microelectronics Development team technical support. The work at Sandia National Laboratories is supported through DOE. Sandia is a multiprogram laboratory operated by Sandia Corporation, a Lockheed Martin Company, for the United States Department of Energy under Contract No. DE-AC04-94AL 85000.

[1] C. M. Cornelius and J. P. Dowling, Phys. Rev. A **59**, 4736 (1999).
[2] S. Y. Lin, J. G. Fleming, E. Chow, J. Bur, K. K. Choi, and A. Goldberg, Phys. Rev. B **62**, R2243 (2000).
[3] J. G. Fleming, S. Y. Lin, I. El-Kady, R. Biswas, and K. M. Ho, Nature (London) **417**, 52 (2002).
[4] S. Y. Lin, J. G. Fleming, D. L. Hetherington, B. K. Smith, R. Biswas, K. M. Ho, M. M. Sigalas, W. Zubrzycki, S. R. Kurtz, and J. Bur, Nature (London) **394**, 252 (1998).
[5] E. Ozbay, B. Temelkuran, M. M. Sigalas, G. Tuttle, C. M. Soukoulos, and K. M. Ho, Appl. Phys. Lett. **69**, 3797 (1996).
[6] K. Sakoda, Opt. Express **4**, 167 (1999).
[7] N. A. R. Bhat and J. E. Sipe, Phys. Rev. E **64**, 056604 (2001).
[8] S. John and J. Wang, Phys. Rev. B **43**, 12772 (1991).
[9] S. John and T. Quang, Phys. Rev. A **50**, 1764 (1994).
[10] S. Y. Lin, J. G. Fleming, Z. Y. Li, I. El-Kady, R. Biswas, and K. M. Ho, J. Opt. Soc. Am. B (in press).
[11] R. Loudon, *The Quantum Theory of Light* (Clarendon, Oxford, 1983), Chap. 1, pp. 13–17 and Chap. 5.
[12] A. Yariv, *Quantum Electronics* (Wiley, New York, 1989), Chap. 5, pp. 99–100.
[13] *Gmelin Handbook of Inorganic Chemistry*, 8th ed. (Springer, Berlin, 1989), W Suppl., Vol. A3, pp. 181–185.
[14] J. G. Fleming and S. Y. Lin, Opt. Lett. **24**, 49 (1999).
[15] See, for example, E. L. Dereniak and G. D. Boreman, *Infrared Detectors and Systems*, Series in Pure and Applied Optics (Wiley, New York, 1996), Chap. 2, pp. 69–70.

Three-dimensional photonic-crystal emitter for thermal photovoltaic power generation

S. Y. Lin,[a] J. Moreno, and J. G. Fleming
MS 0603, Sandia National Laboratories, P.O. Box 5800, Albuquerque, New Mexico 87185

(Received 7 April 2003; accepted 23 May 2003)

A three-dimensional tungsten photonic crystal is experimentally realized with a complete photonic band gap at wavelengths $\lambda \geq 3$ μm. At an effective temperature of $\langle T \rangle \sim 1535$ K, the photonic crystal exhibits a sharp emission at $\lambda \sim 1.5$ μm and is promising for thermal photovoltaic (TPV) power generation. Based on the spectral radiance, a proper length scaling and a planar TPV model calculation, an optical-to-electric conversion efficiency of ~34% and electrical power of ~14 W/cm^2 is theoretically possible. © *2003 American Institute of Physics.*
[DOI: 10.1063/1.1592614]

There is an emerging interest in using thermal photovoltaic (TPV) cells for electric-power generation.[1,2] Similar to a solar cell, in which solar radiation is converted into electricity, a TPV cell converts thermal radiation into electricity. The optical-to-electricity conversion is based on photocurrent generation by those photons having energy exceeding the electronic band gap, ($\hbar\omega_{\text{radiation}} \geqslant E_g$). The portion of photons with $\hbar\omega_{\text{radiation}} \leqslant E_g$ is not useful, leading to a lower conversion efficiency. In other words, E_g is the cutoff energy, below which radiation energy is wasted. To maximize conversion efficiency, it is desirable to have a narrow-band spectrum with its radiation energy slightly above the electronic band gap. While the solar spectrum is given, a thermal radiation spectrum may be modified by choice of radiator materials,[2] by surface structuring[3,4] and also by photonic band gap engineering.[5–9] In particular, a three-dimensional (3D) complete photonic band gap can be used to suppress radiation below the electronic band gap.[7,8] Meanwhile, emission can be enhanced at a narrow band near a photonic band edge or a narrow allowed band.[7,8] If both effects are combined, a nearly ideal radiation spectrum can be obtained.

In this letter, a tungsten 3D photonic crystal is experimentally realized with a complete photonic band gap at wavelengths $\lambda \geqslant 3$ μm. At a sample temperature of ~1535 K, the photonic-crystal emission is suppressed in the photonic band gap regime ($\lambda > 3$ μm), exhibits a peak at $\lambda \sim 1.5$ μm, and a narrow spectral width of $\Delta\lambda \sim 0.9$ μm. This nearly ideal radiation spectrum could lead to an optical-to-electric conversion efficiency of $\eta \sim 34\%$ and electric power density of $p \sim 14$ W/cm^2.

The 3D tungsten photonic crystal is fabricated using a modified silicon process. In the first step, a layer of silicon dioxide is deposited, patterned, and etched to create a mold. The mold is then filled with a 500-nm-thick tungsten film and planarized using a chemical mechanical polishing process. The process is repeated several times. At the end of the process, the silicon dioxide is released from the substrate and the sample is a freely standing thin film. A scanning electron micrograph (SEM) image of the fabricated sample is shown in Fig. 1(a). The one-dimensional (1D) rods represent the shortest ⟨110⟩ chain of atoms in a diamond lattice.[10,11] The rod-to-rod spacing is $a = 1.5$ μm, the rod width is $w = 0.5$ μm, and rod height $h \sim 0.75$ μm.

In Fig. 1(b), the computed absorption spectrum for an eight-layer photonic-crystal sample is shown. The absorptance is low for $\lambda > 3$ μm (the photonic band gap) and increases slightly at $\lambda \sim 3$–4 μm due to a higher tungsten material absorption at these wavelengths.[12] This band gap has been shown to be a complete band gap, capable of trapping light fully in all three dimensions and for both polarizations.[7] Beyond the photonic band gap regime, there are two strong absorptions. One is at $\lambda = 2.5$ μm with an absorptance of ~40% and the other at $\lambda = 1.5$–1.9 μm with an even stronger absorptance of ~80%. The high absorptance is due to a combination of finite tungsten absorption and a high density of

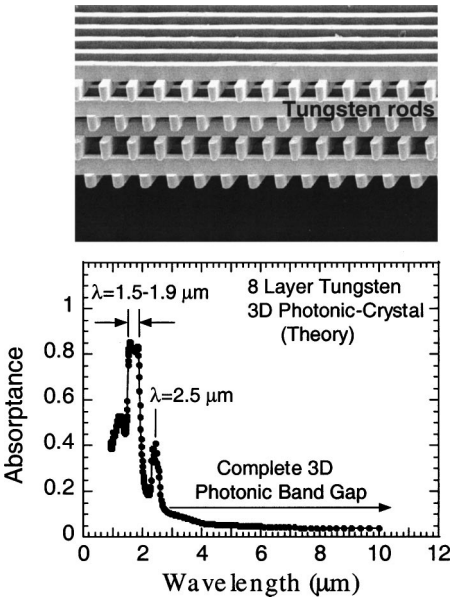

FIG. 1. (a) A SEM view of a 3D tungsten photonic crystal. Within each layer, the 1D rod width is 0.5 μm and the rod-to-rod spacing is 1.5 μm. (b) A computed absorption spectra for an eight-layer 3D tungsten photonic-crystal sample. The absorptance is low for $\lambda > 3$ μm (the photonic band gap), exhibits a peak of ~40% at $\lambda \sim 2.5$ μm, and a high plateau of ~80% at $\lambda \sim 1.5$–1.9 μm.

[a]Electronic mail: slin@sandia.gov

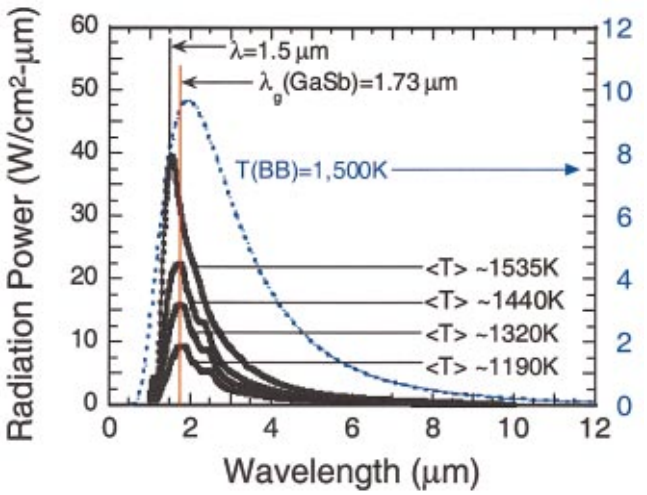

FIG. 2. (Color) The measured photonic-crystal emission power at a bias of $V=3$, 4, 5, and 6.5 V, respectively. The effective temperature, average over the entire sample, is $\langle T\rangle \sim 1190$, 1320, 1440, and 1535 K, respectively. At $\langle T\rangle \sim 1535$ K, the emission peaks at $\lambda \sim 1.5$ μm and has a full width at half maximum of 0.9 μm. The dashed blue line is a blackbody radiation curve. The electronic band gap wavelength of GaSb is also shown as a red line.

photon-states $D(\omega)$ at a narrow band.[13–15] As absorption and emission processes have the same physical origin,[16] a strong narrow absorption is suggestive of a narrow band emission from a photonic-crystal sample.

To achieve emission, the sample is biased by applying a voltage across the photonic-crystal sample and is heated through Joule heating. The emission spectra of the 3D photonic crystal are taken using a standard Fourier-transform infrared spectrometer from $\lambda=1$–15 μm.[17,18] As the sample is operated at high temperatures, it is mounted to be thermally and electrically isolated from its surroundings. To minimize thermal loss, the sample is placed in a vacuum chamber pumped to $\sim 10^{-5}$ Torr. For power density measurements, a commercially available Gentec power meter, calibrated to better than 5%, is used.

In Fig. 2, emission spectra taken at a bias of $V=3$, 4, 5, and 6.5 V are shown, respectively. The effective temperature, averaged over the entire sample, is $\langle T\rangle = 1190$, 1320, 1440, and 1535 K, respectively. It is determined by measuring sample resistivity and by comparing it to the calibrated, temperature-dependent tungsten resistivity. At $V=3$ V, or $\langle T\rangle \sim 1190$ K, the emission consists of a weak peak at $\lambda \sim 2.5$ μm and a stronger peak at $\lambda \sim 1.8$ μm. At a higher temperature, $\langle T\rangle \sim 1535$ K, the stronger peak dominates the spectrum and shifts to $\lambda \sim 1.5$ μm. The dashed blue curve is a blackbody cavity-radiation spectrum, having a peak power density of 9.8 W/cm^2 at $\lambda \sim 2$ μm and a full width at half maximum of $\Delta\lambda(\mathrm{FWHM}) \sim 2.3$ μm. Yet, the photonic-crystal (PBG) emission exhibits a peak power density of 40.5 W/cm^2 at $\lambda \sim 1.5$ μm and a much narrower $\Delta\lambda(\mathrm{FWHM}) \sim 0.9$ μm. To achieve a spectral linewidth this narrow, one would have to heat a blackbody to a temperature of $T \sim 4000$ K. The narrow PBG emission implies a better match of the emission spectrum to electronic band gap of a photovoltaic cell. The higher PBG-emission power than that of a blackbody (BB) emission at a selective wavelength range is beyond the scope of this letter, and is discussed in a separate publication.[8] For reference purposes, the band gap wavelength, $\lambda_{\text{band gap}} \approx 1.73$ μm, of a GaSb photovoltaic cell is shown as a solid red line.

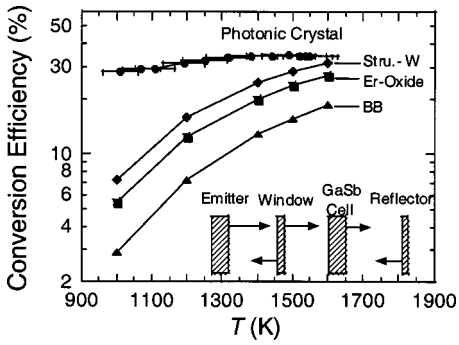

FIG. 3. The computed thermal photovoltaic conversion efficiency for four different emitters at temperatures $T=1000$–1600 K. The PBG emitter has a high efficiency of $\eta=27\%$–33%. In the inset, an illustration of radiative flux in a simple one-dimensional thermal photovoltaic model is shown.

To model photovoltaic energy conversion, a planar system is used to describe radiation heat transfer. This model is intended to evaluate radiator performance and does not include a process to heat the radiator. The radiation model we used is similar to Zenker *et al.*[2] As shown in the inset of Fig. 3, the system consists of an emitter, a cell window (model cell front surface), a GaSb photovoltaic cell, and a reflector. Both an ideal and a realistic window reflectivity are considered.[2] As our photonic-crystal itself emits a spectrally narrow radiation, no filter is used. The GaSb cell is modeled in the context of its thermodynamic limit at $T=300$ K. In this limit, the GaSb internal quantum efficiency is assumed to be one for $\hbar\omega_{\text{radiation}} \geqslant E_g$. It is also assumed that the only loss mechanism in the cell is radiative recombination. The conservation relations between the spectral radiant fluxes are written and symbolically solved using MathCad software. To check our model against Zenker's, the same cases were run for the thermodynamic limit and for an ideal window reflectivity.

In Table I, the model results are shown for three conventional radiators heated to $T=1500$ K. The BB cavity radiator is a broadband emitter and the Er_2O_3 and the structured tungsten radiators are selective emitters.[2] The optical-to-electric efficiency $\eta(\%)$ is defined as: $\eta \equiv p/Q_{\text{radiation}}$, where p is the electric power density in W/cm^2 and $Q_{\text{radiation}}$ is the total radiation power density. Making allowance for the uncertainties in digitizing the window reflectance in Zenker *et al.*, the agreement for all three emitters is quite reasonable.

Using the same model, the potential performance of a photonic-crystal (PBG) emitter is evaluated. To obtain a more optimal performance, the emission wavelength is scaled by 30%. This scaling corresponds to a photonic crys-

TABLE I. A summary of computed efficiency and power for a broadband emitter (the blackbody) and two selective emitters (the Er_2O_3 and the structured tungsten emitters).

	Zenker *et al.*		This work	
Emitter type	η (%)	El. power (W/cm^2)	η (%)	El. power (W/cm^2)
Blackbody	11	3.0	11	3.0
Er_2O_3	26	1.1	24	1.1
Struc.-tungsten	30	1.6	29	1.6

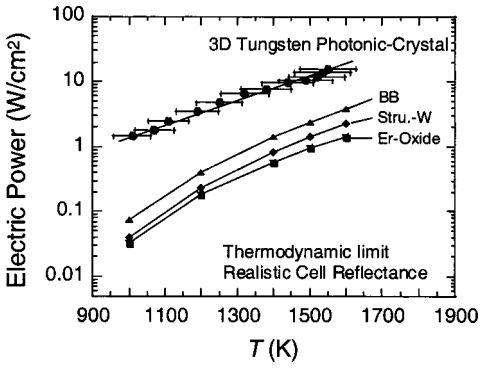

FIG. 4. The computed electric power density for four different emitters at temperatures $T=1000-1600$ K. Photonic-crystal emitter generates the highest output electric power density, yet the structured tungsten and the Er_2O_3 yield the least.

tal with a lattice constant of $a=1.05$ μm. In this analysis, a realistic window reflectivity is used. In Fig. 3, the computed efficiency for the PBG emitter and the three conventional emitters is shown. The PBG emitter has a high efficiency of $\eta=27\%-33\%$ over the entire temperature range. As the peak PBG-emission wavelength does not shift significantly with temperature (see Fig. 2), this nearly constant efficiency is expected. By contrast, the efficiency of the three conventional emitters exhibits a strong temperature dependence. The efficiency of the blackbody emitter increases from 3% to 15% for $T=1000-1600$ K. The efficiency is low as only a small fraction of the blackbody radiation satisfies the cutoff condition: $\hbar\omega_{\text{radiation}} \geqslant E_g$, or $\lambda_{\text{radiation}} \leqslant \lambda_{\text{band gap}}=1.73$ μm. For $T=1000-1600$ K, a blackbody emission peaks at λ_{peak} (μm)$\cong 2898/T(\text{K})=1.81-2.89$ μm>1.73 μm. Efficiency of the selective emitters, both Er_2O_3 and structured tungsten, is higher than that of a blackbody emitter. This is due to their shorter peak emission wavelength $\lambda_{\text{peak}} \approx 1.55-1.7$ μm and narrower spectral width[2,3] compared with that of a blackbody emitter.

In Fig. 4, the computed power density is plotted as a function of temperature for the PBG emitter and the three conventional emitters. As temperature is increased, radiation energy density is increased accordingly, leading to higher power density for all four emitters. The highest electric power density is generated by the PBG emitter. At $\langle T\rangle=1500$ K, the expected electric power is $p=13$, 2.4, 1.4, and 0.94 W/cm^2 for PBG, BB, structured tungsten, and Er_2O_3 emitters, respectively. This high value of electric power from a PBG emitter is a result of a narrow spectral width and high optical power density as shown in Fig. 2. The structured tungsten and Er_2O_3 produce the least electric power. This is because, for these selective emitters, their total radiation intensity for $\hbar\omega_{\text{radiation}} \geqslant E_g$ is less than that of a blackbody emitter. A selective emitter can yield high conversion efficiency, but often at the expense of a lower electric power density.

In summary, a 3D tungsten photonic crystal is realized in the near-infrared wavelengths. Comparing to a blackbody cavity radiation at $T\sim 1500$ K, its emission has a spectral width nearly 2.5 times narrower and also peaks at a lower wavelength of $\lambda\sim 1.5$ μm. Based on the spectral radiance, a proper length scaling and a planar TPV model calculation, a PBG emitter can yield an optical-to-electric conversion efficiency of $\sim 34\%$ and electrical power density of ~ 14 W/cm^2 at $\langle T\rangle\sim 1535$ K. A PBG emitter, thus, offers a potentially better efficiency and power over conventional emitters, including the blackbody cavity, the Er_2O_3, and the structured tungsten emitters.

The authors thank J. Gee for valuable discussion and J. Bur, M. Tuck, and J. Rivera for technical support. The work at Sandia National Laboratories is supported through DOE. Sandia is a multiprogram laboratory operated by Sandia Corporation, a Lockheed Martin Company, for the United States Department of Energy under Contract No. DE-AC04-94AL 85000.

[1] T. J. Coutts and M. C. Fitzgerald, Sci. Am. **1998**(7), 90.
[2] M. Zenker, A. Heinzel, G. Stollwerck, J. Ferber, and J. Luther, IEEE Trans Electron Devices **48**, 367 (2001).
[3] A. Heinzel, V. Boerner, A. Gombert, B. Blasi, V. Wittwer, and J. Luther, J. Mod. Opt. **47**, 2399 (2000).
[4] M. U. Pralle, N. Moelders, M. P. McNeal, I. Puscasu, A. C. Greenwald, J. T. Daly, E. A. Johnson, T. George, D. S. Choi, I. El-Kady, and R. Biswas, Appl. Phys. Lett. **81**, 4685 (2002).
[5] S. Y. Lin, J. G. Fleming, E. Chow, J. Bur, K. K. Choi, and A. Goldberg, Phys. Rev. B **62**, R2243 (2000).
[6] C. M. Cornelius and J. P. Dowling, Phys. Rev. A **59**, 4736 (1999).
[7] J. G. Fleming, S. Y. Lin, I. El-Kady, R. Biswas, and K. M. Ho, Nature (London) **417**, 52 (2002).
[8] S. Y. Lin, J. G. Fleming, I. El-Kady, and K. M. Ho (unpublished).
[9] J. D. Joannopoulos, R. D. Meade, and J. N. Winn: *Photonic Crystal* (Princeton University Press, Princeton, 1995).
[10] K. M. Ho, C. T. Chan, C. M. Soukoulis, R. Biswas, and M. Sigalas, Solid State Commun. **89**, 413 (1994).
[11] E. Ozbay, B. Temelkuran, M. M. Sigalas, G. Tuttle, C. M. Soukoulis, and K. M. Ho, Appl. Phys. Lett. **69**, 3797 (1996).
[12] M. A. Ordal, L. L. Long, R. J. Bell, S. E. Bell, R. R. Bell, R. W. Alexander, Jr., and C. A. Ward, Appl. Opt. **22**, 1099 (1983).
[13] S. Y. Lin, J. G. Fleming, Z. Y. Li, I. El-Kady, R. Biswas, and K. M. Ho, J. Opt. Soc. Am. B **20**, 1538 (2003).
[14] N. A. R. Bhat and J. E. Sipe, Phys. Rev. E **64**, 056604 (2001).
[15] K. Sakoda, *Optical Properties of Photonic Crystals* (Springer, New York, 2001), Chap. 5, p. 108.
[16] R. Loudon, *The Quantum Theory of Light* (Clarendon, Oxford, 1983), Chap. 1, pp. 13–17 and Chap. 5.
[17] S. Y. Lin, J. G. Fleming, D. L. Hetherington, B. K. Smith, R. Biswas, K. M. Ho, M. M. Sigalas, W. Zubrzycki, S. R. Kurtz, and J. Bur, Nature (London) **394**, 252 (1998).
[18] J. G. Fleming and S. Y. Lin, Opt. Lett. **24**, 49 (1999).

Origin of absorption enhancement in a tungsten, three-dimensional photonic crystal

S. Y. Lin and J. G. Fleming

MS 0603, Sandia National Laboratories, P.O. Box 5800, Albuquerque, New Mexico 87185

Z. Y. Li, I. El-Kady, R. Biswas, and K. M. Ho

Ames Laboratory, Department of Physics and Astronomy, Iowa State University, Ames, Iowa 50011

Received July 25, 2002; revised manuscript received February 18, 2003

A three-dimensional, metallic photonic crystal is realized and its absorption measured at infrared wavelengths. The metallic absorption rate is found to be suppressed in the photonic bandgap regime ($\lambda \sim 8-20\ \mu$m). On the other hand, order-of-magnitude absorption enhancement is observed at the photonic band edge ($\lambda \sim 5.8\ \mu$m). The enhancement is attributed to the slower group velocity of light at the photonic band edge, a longer photon–matter interaction length, and a finite intrinsic absorption of tungsten. © 2003 Optical Society of America

OCIS codes: 130.0130, 250.0250, 270.0270.

Optical absorption is among the most basic photon–matter interactions in nature. Phenomenologically, Einstein introduced the so-called A, B coefficients to characterize absorption and spontaneous and stimulated emission processes of a quantized system.[1] Quantum mechanically, A, B coefficients can be described as a summation of dipole-transition matrix elements over all available photonic density of states (DOS).[1] In a photonic crystal environment, photonic DOS may be engineered and a material's absorption rate ($1/\tau_{12}$) altered. More specifically, in the photonic bandgap regime, photonic DOS vanishes and no light is allowed either to penetrate into or radiate out of a photonic crystal structure. As light–matter interaction is suppressed, no absorption in the bandgap regime is possible. Another interesting case occurs near and at the photonic band edge where the electromagnetic Bloch wave is still extended throughout the structure, its v_g is near zero, and the photonic DOS is greatly increased.[2] In this regime, enhanced light–matter interaction is expected, and application of it to enhance absorption,[3] laser gain,[2–5] and nonlinear effects have all been proposed.[3,4] It has also been predicted that, at the band edge, a new photon–atom bound state may occur.[6,7] A photonic crystal thus offers unique environment for modifying the intrinsic optical interactions inside a material.

We describe a tungsten three-dimensional (3D) photonic crystal which is realized in the infrared and whose absorption properties are measured and analyzed. The tungsten absorption rate is found to be greatly suppressed in the photonic bandgap regime ($\lambda \sim 8-20\ \mu$m) of a tungsten, 3D photonic crystal. More importantly, an order-of-magnitude absorption enhancement is observed at the photonic band edge. An analysis is performed to understand the underlying mechanisms for absorption enhancement. It is found that the enhancement is due to the slower group velocity of light at the band edge, a longer photon–matter interaction length, and the material's intrinsic absorption.

Infrared, 3D silicon and tungsten photonic crystals have a diamond-crystal symmetry and are fabricated by a layer-stacking method.[8] Scanning electron microscopy images of the fabricated 3D silicon and tungsten photonic crystals are shown in Figs. 1(a) and 1(b), respectively. The one-dimensional rods represent the shortest ⟨110⟩ chain of atoms in a diamond lattice and are stacked like Lincoln Logs®. The rod-to-rod spacing is $a = 4.2\ \mu$m, the rod width is $w = 1.2\ \mu$m, and rod height is $h \sim 1.5\ \mu$m. The stacking sequence is such that four layers constitute unit cell. The fabrication details for our 3D photonic crystal structures have been described previously.[9–11]

The experimental reflection (R) spectra of the 3D photonic crystals are taken using a standard Fourier-transform-infrared spectrometer for wavelengths $\lambda = 2-20\ \mu$m. The absorption (A) spectrum is measured using a photoacoustic method.[12] The photoacoustic cell is commercially available and was easily adapted to our Fourier-transform-infrared spectrometer system. To obtain absolute values of R and A, a proper normalization of the sample signal to a reference is necessary. Reflectance from a silver mirror ($R > 98\%$ at infrared wavelengths) is used as our R reference. The absorption reference is taken from a carbon black absorber that has an A of 0.99 for $\lambda = 2-20\ \mu$m.

We first study R and A for a silicon 3D, photonic crystal. In Fig. 2(a), the high R at $\lambda \sim 10-14\ \mu$m indicates the existence of a photonic bandgap. The lower and higher band edges occur at $\lambda \sim 10\ \mu$m and $14\ \mu$m, respectively. Despite the intricate R spectrum, the absorption spectrum (blue curve) has no feature and the absorption is low ($<0.2\%$) for all wavelengths. This observation is consistent with the fact that silicon is a low-loss dielectric material at $\lambda \sim 1.2-20\ \mu$m. In Fig. 2(b), we show R and A

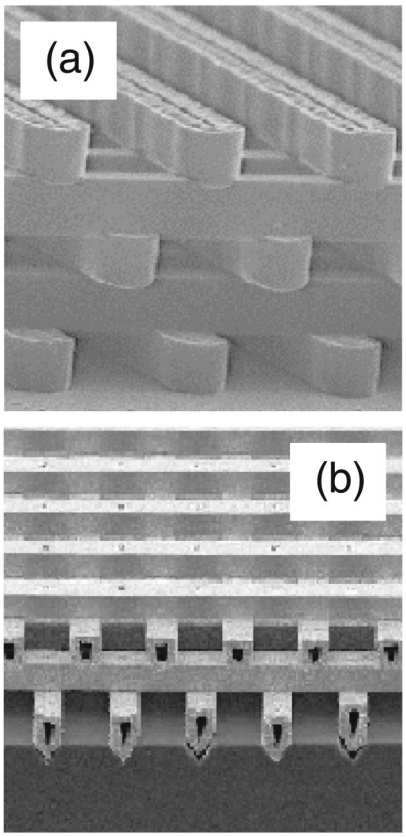

Fig. 1. Cross-sectional scanning-electron-microscopy view of 3D silicon (a) and tungsten (b) photonic crystals built using a layer-stacking design. Within each layer, the one-dimensional rod width is 1.2 μm and the rod-to-rod spacing is 4.2 μm.

for the tungsten, 3D photonic crystal. Although the data have been reported earlier,[10] they are shown here for comparison purposes. In brief, the R exhibits a large photonic bandgap for $\lambda \sim 8-20$ μm, a band edge at $\lambda \sim 6$ μm, and allowed band oscillations for $\lambda < 5$ μm. More important, the A exhibits a pronounced peak at the band edge of $\lambda \sim 5.8$ μm. The peak absorption of 22% is ~100 times larger than that observed (<0.2%) at the bandgap regime ($\lambda > 8$ μm). The simultaneous suppression of absorption at the bandgap and enhancement of it at the band edge is important for thermal emission modification. The observation of absorption enhancement only in the metallic, 3D photonic crystal suggests the importance of using metallic materials, as well as having the photonic band edge. The origin of the absorption enhancement is investigated next by theoretically computing R and A using a newly developed transfer-matrix method.[13] The method can effectively account for the presence of a complex dielectric function in a metallic, 3D photonic crystal.

To achieve absorption enhancement in a metallic 3D, photonic crystal, three criteria must be satisfied. First, the absorption must occur at or near the band edge. To verify this, the photonic band edge position is systematically shifted by increasing the layer thickness h from 1.5 to 2.0 to 2.4 μm. As will become clear later, the photonic bandgap dispersion is strongly dependent on h. In Fig. 3, the computed R (black curve) and A (blue curve) spectra for the three cases are shown. The R for $h = 1.5$ μm, Fig. 3(a), shows a band edge at $\lambda \sim 5.8$ μm. Correspondingly, an absorption peak of 18% is observed at $\lambda \sim 5.8$ μm. The computed peak absorption value agrees with the measured ones within 4%. The structural imperfection of the first layer of tungsten rods (see Fig. 1) could scatter light and result in the smaller experimental absorption value. The second absorption peak at $\lambda \sim 4.5$ μm is also evident at the second band edge. For $h = 2$ μm, Fig. 3(b), the first band edge is shifted to $\lambda \sim 6.6$ μm and the second bandgap is better developed at $\lambda \sim 6$ μm. Both the first and second absorption peaks occur at the photonic band edge of $\lambda \sim 6.6$ and 5 μm, respectively. The absorption peak at $\lambda \sim 6.6$ μm has a higher amplitude (~37%) and narrower bandwidth ($\Delta\lambda = 0.25$ μm) compared with those for $h = 1.5$ μm. As h is further increased to 2.4 μm, the band edges continued to shift to longer wavelengths and the second bandgap is now well developed. The peak absorption again occurs at the photonic band edge of $\lambda \sim 7.4$ μm. The peak absorption amplitude is further increased to 48% and the bandwidth further narrowed to $\Delta\lambda \sim 0.13$ μm. The first allowed band is tightly sandwiched between the first and second bandgap, which leads to a flat frequency-wavevector dispersion. These data show that absorption [see inset of Fig. 2(b)] is preferentially enhanced and always occurs at the photonic band edges. It is known that the

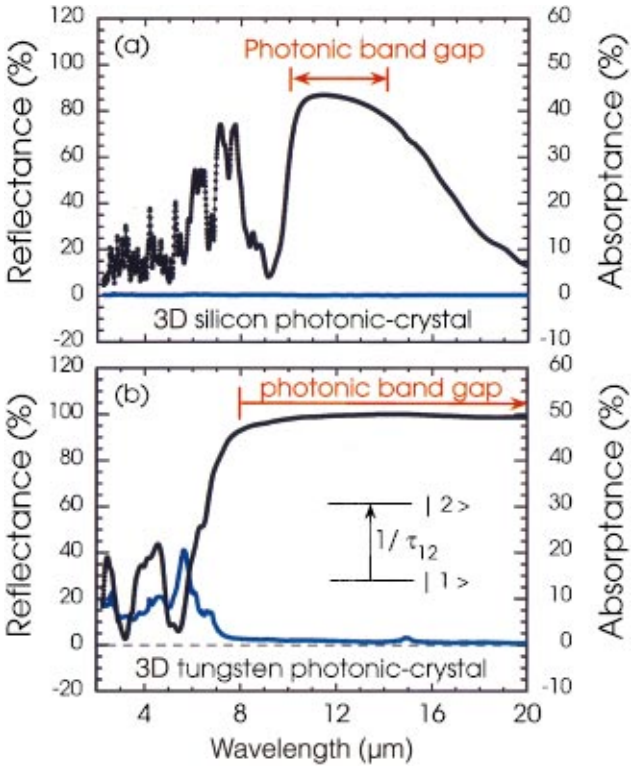

Fig. 2. (a) Measured reflection (black) and absorption (blue) spectra for a silicon, 3D photonic crystal. The photonic bandgap is at $\lambda \sim 10-14$ μm. Despite the intricate reflection spectra, the absorption spectrum is featureless and its amplitude low, i.e., <0.2%. (b) Measured reflection (black) and absorption (blue) spectra for the tungsten, 3D photonic crystal. The photonic bandgap is at $\lambda \sim 8-20$ μm and band edge at $\lambda \sim 5.8$ μm. While the absorption nearly vanishes in the bandgap regime, it shows peak of 22% at the photonic band edge. Thus, the absorption rate ($1/\tau_{12}$) of a tungsten photonic crystal structure is selectively enhanced at the band edge.

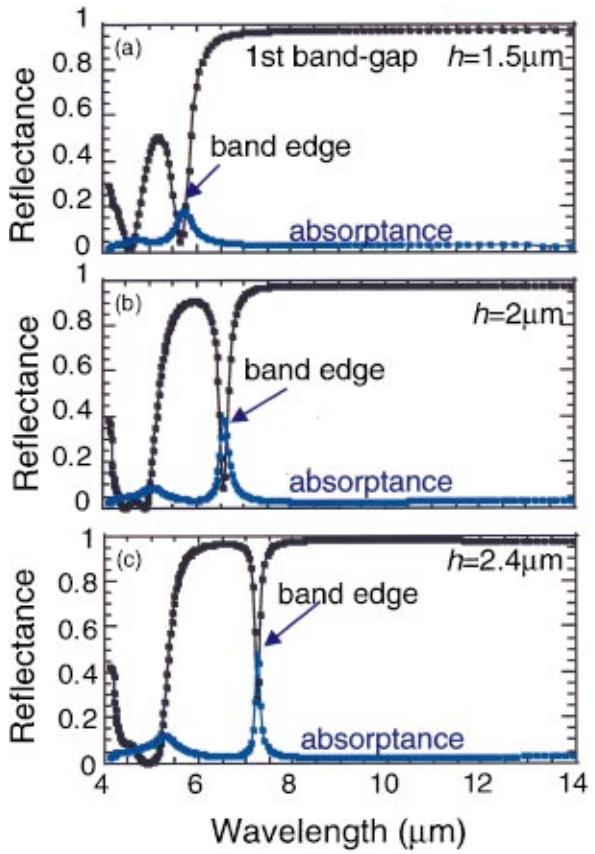

Fig. 3. Computed reflection (black) and absorption (blue) spectra for samples with different rod thickness h = (a) 1.5, (b) 2.0, and (c) 2.4 μm, respectively. As h is increased, the reflectance band edge is shifted systematically from $\lambda \sim 6$ to 6.6 to 7.4 μm. The absorption peak always occurs at the band edge. The absorption amplitude is also increased from 18 to 36 to 46%. Meanwhile, the second bandgap becomes better developed as h is increased and is also shifted from $\lambda \sim 5$ to 6 to 7 μm.

group velocity (V_g) of light approaches zero near the band edge.[2] The slower moving light thus experiences a longer light–matter interaction time ($\sim 1/V_g$) and is absorbed more strongly. This observation is also consistent with theoretical modeling that predicts that the enhancement is proportional to $1/V_g$.[2,4]

The second criterion is that the peak absorption amplitude depends on the number of layers N of the structure. In contrast, a typical metallic absorption depends on the skin depth of the metal surface layer. The peak absorption amplitude is computed for samples with different numbers of layers N and is plotted in Fig. 4. The peak absorption (filled circles) is 18% for $N = 4$, or equivalently, one unit cell. It then rises sharply for $4 < N < 8$ and becomes saturated at ~60% for $N > 12$. Meanwhile, the peak wavelength (open circles) remains nearly constant at $\lambda \sim 5.8$ μm for all Ns. The slight increase of the peak λ for $N > 6$ is due to the band edge's becoming sharper and moving toward longer λ for larger Ns. For $N < 4$, the structure is less than one unit cell and neither the bandgap nor band edge is well developed. The peak absorption saturates at 60%. That this does not occur at 100% is partially because of a finite reflectance at the air–crystal interface. The functional dependence of absorption is exponentiallike and is similar to that for an absorbing material with a constant attenuation coefficient. The red curve is a fit to such an exponential function: $A(\lambda \sim 5.8\ \mu\text{m}) = B_0 - B_1 * \exp(-\alpha_{\text{eff}} * H)$. Here, B_0 is the saturation value, B_1 is a fitting parameter to take into account that the bandgap is well developed only for $N > 4$, H ($=N*h$) is the total sample thickness, and α_{eff} is the attenuation constant of light in the tungsten, 3D photonic crystal. The fit is good and the deduced B_0, B_1, and α_{eff} are 0.58, 1.9, and 0.26 μm^{-1}, respectively. The deduced absorption length ($=1/\alpha_{\text{eff}}$) of 3.8 μm at $\lambda \sim 5.8$ μm is long compared to the skin depth (~20 nm) of the tungsten material at the same λ. For comparison, this absorption length is compatible with that for a GaAs semiconductor ($1/\alpha_{\text{eff}} \sim 0.8$ μm) at $\lambda = 0.82$ μm. Clearly, light continues to be absorbed as it traverses the photonic crystal structure as thick as 21 μm for the $N = 14$ sample. The electromagnetically excited Bloch wave can mold its way through the entire photonic crystal structure, which results in a much longer light–matter interaction length. Thus, the N-dependency of the absorption amplitude is attributed to the extended nature of the Bloch waves.

The third and last criterion is that the peak absorption must originate from the intrinsic tungsten absorption, or the imaginary part of its dielectric constant $\epsilon_i(\omega)$. To verify this, the absorption spectrum is computed for a series of samples using $\beta\epsilon_i(\omega)$ as a variable. Here, β is varied from 0% to 100%, corresponding to no and full intrinsic absorption, respectively. In Fig. 5, a summary of the peak absorption amplitude versus β for our tungsten, 3D photonic crystal is shown. The open circles are computed absorption values for a uniform tungsten film, which increases linearly from 0 to 1.4% as β is varied from 0 to 100%. For $N = 4$, the peak absorption amplitude (filled circles) also scales linearly with β and reaches 18% at the full absorption, $\beta = 100\%$. The same scaling behavior has been predicted previously in a calculation for enhanced stimulated emission at the band edge.[4] These data show that both the tungsten material absorption and the photonic crystal band edge absorption have the same origin, which is $\beta\epsilon_i(\omega)$. The effect of photonic band edge is to enhance the absorption rate. But once β

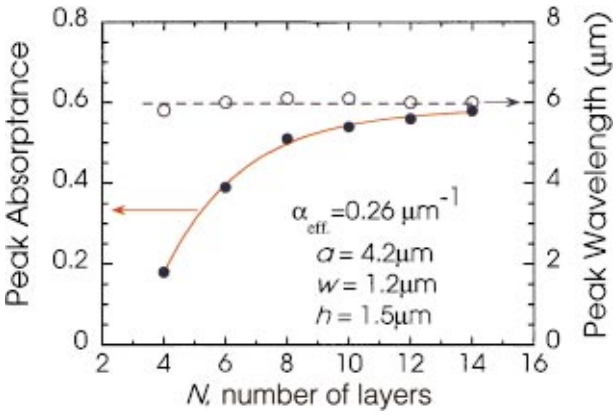

Fig. 4. Computed peak absorption as a function of number of layers N or sample thickness. The absorptance amplitude increases sharply for $N = 4$–8 and becomes nearly saturated at ~60% for $N > 12$. Clearly, light is being continuously absorbed as it traverses the whole photonic crystal structure.

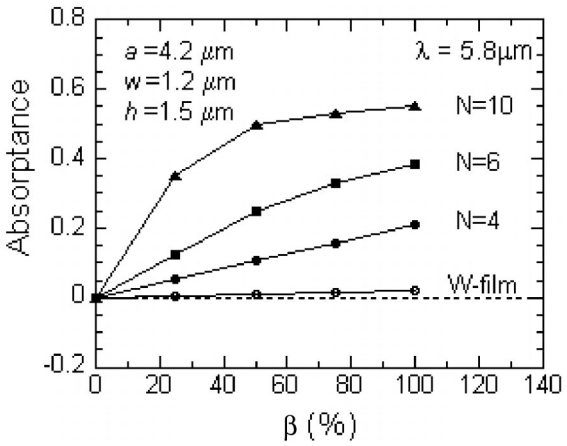

Fig. 5. Summary of peak absorptance versus $\beta\epsilon_i(\omega)$ for a series of tungsten, 3D photonic crystal samples. The absorptance of a uniform tungsten film (open circles) is also shown as a reference. The absorptance vanishes for a perfect conductor ($\beta = 0$) and increases linearly with material absorption $\beta\epsilon_i(\omega)$ for $N = 4$. For $N = 10$, the absorptance (triangles) rises sharply for $\beta < 50\%$ and reaches a saturation value of ~54% at $\beta = 100\%$.

is set to zero, no absorption is possible even with the band edge enhancement effect. This also explains why no absorption is observed for our silicon, 3D photonic crystal, as $\epsilon_i(\omega)$ for silicon is low ($<3 \times 10^{-3}$) in its transparent regime.[14]

For $N = 6$, absorption (squares) increases linearly for $\beta < 75\%$ and starts to slow at $\beta = 100\%$. For $N = 10$, absorption (triangles) rises sharply for $\beta < 50\%$ and reaches a saturation value of ~54% at $\beta = 100\%$. One may define an absorption enhancement factor (η) as the ratio of the intrinsic tungsten absorption to the absorption of the photonic crystal at the band edge at the same wavelength. For $N = 10$, the enhancement factor is then as large as $\eta = 100$, 70, 50, and 40 for $\beta = 25$, 50, 75, and 100%, respectively.

In summary, a 3D, metallic photonic crystal is realized and its absorption measured at infrared wavelengths. The metallic absorption rate is found to be suppressed in the photonic bandgap regime ($\lambda \sim 8-20\ \mu$m) and strongly enhanced at the photonic band edge ($\lambda \sim 6\ \mu$m). The peak absorption in our tungsten photonic crystal is an effective absorption that originates from the intrinsic tungsten absorption and is subsequently enhanced by the photonic band edge effect. The enhancement is attributed to a longer photon–matter interaction length as compared to the metallic skin depth, the slower group velocity of light at the band edge, and the finite metallic absorption constant.

The authors thank Dr. J. Moreno and J. Gees for valuable discussion and M. Tuck and J. Bur for technical support. Sandia is a multiprogram laboratory operated by Sandia Corporation, a Lockheed Martin Company, for the United States Department of Energy under contract DE-AC04-94AL 85000.

S. Y. Lin may be reached by e-mail at slin@sandia.gov.

REFERENCES

1. R. Loudon, *The Quantum Theory of Light* (Clarendon, Oxford, 1983), Chap. 1, pp. 13–17 and Chap. 5.
2. J. P. Dowling, M. Scalora, M. J. Bloemer, and C. M. Bowden, "The photonic band edge laser: A new approach to gain enhancement," J. Appl. Phys. **75**, 1896–1899 (1994).
3. N. A. R. Bhat and J. E. Sipe, "Optical pulse propagation in nonlinear photonic crystals," Phys. Rev. E **64**, 056604 (2001).
4. K. Sakoda, *Optical Properties of Photonic Crystals* (Springer-Verlag, New York, 2001), Chap. 5, p. 108.
5. V. I. Koop, B. Fan, H. K. M. Vithana, and A. Z. Genack, "Low-threshold lasing at the edge of a photonic stop band in cholesteric liquid crystals," Opt. Lett. **23**, 1707–1709 (1998).
6. S. John and T. Quang, "Spontaneous emission near the edge of a photonic band gap," Phys. Rev. A **50**, 1764–1769 (1994).
7. S. John and T. Quang, "Localization of Superradiance near a Photonic Band Gap," Phys. Rev. Lett. **74**, 3419–3422 (1995).
8. K. M. Ho, C. T. Chan, C. M. Soukoulis, R. Biswas, and M. Sigalas, "Photonic band-gaps in three dimensions: new layer-by-layer periodic structures," Solid State Commun. **89**, 413–416 (1994).
9. S. Y. Lin, J. G. Fleming, D. L. Hetherington, B. K. Smith, R. Biswas, K. M. Ho, M. M. Sigalas, W. Zubrzycki, S. R. Kurtz, and J. Bur, "A three-dimensional photonic crystal operating at infrared wavelengths," Nature **394**, 252–253 (1998).
10. J. G. Fleming, S. Y. Lin, I. El-Kady, R. Biswas, and K. M. Ho, "All-metallic three-dimensional photonic crystals with a large infrared bandgap," Nature **417**, 52–55 (2002).
11. J. G. Fleming and S. Y. Lin, "Three-dimensional photonic crystal with a stop band from 1.35 to 1.95 μm," Opt. Lett. **24**, 49–51 (1999).
12. J. F. McClelland, R. W. Jones, S. Lou, and L. M. Seaverson, "A practical guide to FTIR photoacoustic spectroscopy," in *Practical Sampling Techniques for Infrared Analysis*, P. B. Coleman, ed. (CRC Press, Boca Raton, Fla., 1993), Chap. 5.
13. Z. Y. Li, I. El-Kady, K. M. Ho, S. Y. Lin, and J. G. Fleming, "Photonic band gap effect in layer-by-layer metallic photonic crystals," J. Appl. Phys. **93**, 38 (2003).
14. E. D. Palik, ed., *Handbook of Optical Constants of Solids* (Academic, London, 1998), pp. 555–568.

Three-dimensional photonic-crystal emission through thermal excitation

Shawn-Yu Lin, J. G. Fleming, and I. El-Kady

MS 0603, Sandia National Laboratories, P.O. Box 5800, Albuquerque, New Mexico 87185

Received April 21, 2003

A three-dimensional tungsten photonic crystal is thermally excited and shown to emit light at a narrow band, $\lambda = 3.3-4.25\ \mu$m. The emission is experimentally observed to exceed that of the free-space Planck radiation over a wide temperature range, $T = 475-850$ K. It is proposed that an enhanced density of state associated with the propagating electromagnetic Bloch waves in the photonic crystal is responsible for this experimental finding. © 2003 Optical Society of America

OCIS codes: 270.0270, 250.0250.

It has been suggested that a three-dimensional (3D) metallic photonic crystal may be useful for incandescent lamp application and for thermal photovoltaic power generation.[1] For the former, an electrical bias is applied to a photonic-crystal sample and light is generated.[2,3] It remains unclear whether light emission from such a photonic bandgap (PBG) sample is due to an electronic excitation process or to Joule heating. It is therefore important to achieve PBG light emission through other excitation means, such as direct thermal heating with a heater. This experiment is also important for thermal photovoltaic applications, as it requires heating a PBG sample with a thermal source and converting the resulting thermal radiation into electricity.[4] In this Letter a 3D tungsten photonic crystal is realized with a large infrared PBG ($\lambda \geq 5\ \mu$m). It is shown experimentally that thermal excitation can give rise to PBG emission with sharp emission peaks at $\lambda \approx 3.3-4.25\ \mu$m. It is further shown that the amount of radiation transferred from the heated PBG sample into free space exceeds that expected of the free-space Planck radiation.[5,6]

The 3D tungsten photonic-crystal sample is fabricated with a modified silicon process.[1,7] In the first step, a layer of silicon dioxide is deposited, patterned, and etched to create a mold. The mold is filled with a 0.8-μm-thick tungsten film and then planarized. The same process is repeated for each layer. At the end of the process, the silicon dioxide is released, leaving an ~9-μm-thick freely standing thin film. In the inset of Fig. 1(b), a scanning electron microscope image of an eight-layer 3D tungsten photonic-crystal sample is shown. The sample consists of layers of one-dimensional tungsten rods with a stacking sequence that repeats itself every four layers.[7,8] The rod-to-rod pitch is $a = 2.8\ \mu$m, the rod width is $w = 0.8\ \mu$m, and rod height $h \sim 1.1\ \mu$m.

In Fig. 1(a), the measured reflection and transmission spectra are shown for an eight-layer PBG sample. Light propagates along the ⟨001⟩ direction of the crystal and is unpolarized. The reflectance is high for $\lambda \geq 5\ \mu$m (the PBG), decreases sharply at $\lambda \approx 4.5\ \mu$m (the photonic band edge), and shows several reflection dips for $\lambda \leq 4.5\ \mu$m. Correspondingly, the transmittance is low (≤0.5%) in the bandgap and exhibits narrow peaks at $\lambda_1 \approx 3.3, 3.8, 4.25\ \mu$m. From a theoretical calculation,[9] the peaks at $\lambda = 4.25\ \mu$m and $\lambda = 3.8\ \mu$m are due to light propagation in the first allowed mode (the electromagnetic Bloch wave). The $\lambda = 3.2\ \mu$m peak is due to the second allowed-mode propagation. In Fig. 1(b), a computed absorption spectrum is shown. The absorptance is low (≤3%) in the bandgap and exhibits three peaks (≈30%) at $\lambda \approx 3.3, 3.8, 4.1\ \mu$m. The peak absorption is approximately ten times stronger than tungsten's intrinsic absorption (2–3%) and is due to

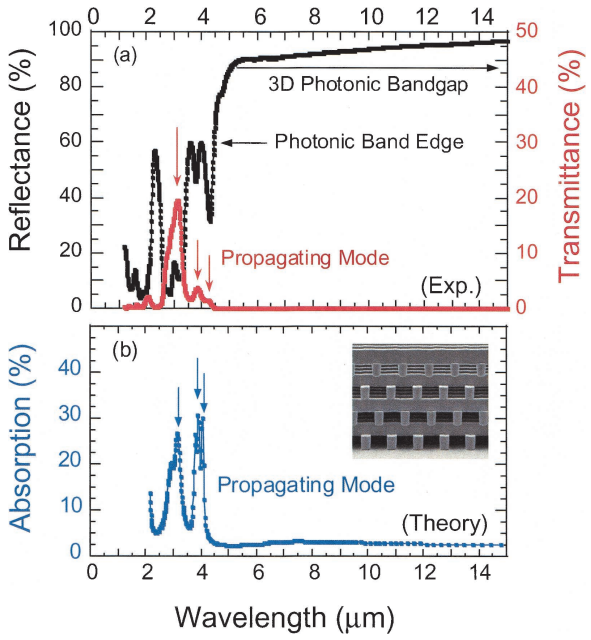

Fig. 1. (a) Measured reflection (black curve) and transmission (red curve) spectra for an eight-layer tungsten photonic-crystal sample. The reflectance is high for $\lambda \geq 5\ \mu$m (the PBG) and decreases sharply at $\lambda \approx 4.5\ \mu$m (the photonic band edge). The transmittance is low (≤0.5%) in the bandgap and exhibits narrow peaks at $\lambda_1 \approx 3.3, 3.8, 4.25\ \mu$m (red arrows). The peaks are due to light propagation through the first and second allowed modes of the photonic crystal. (b) Computed absorption spectrum for the same photonic-crystal sample. The absorptance also exhibits three peaks at $\lambda \approx 3.3, 3.8, 4.1\ \mu$m. Inset, scanning electron microscope side view image of the tungsten photonic-crystal sample.

0146-9592/03/201909-03$15.00/0

an enhanced density of photon states, $D_{\mathrm{PBG}}(\omega)$, in a narrow band.[10,11] Thus, the first and second allowed modes exhibit strong absorption and, at the same time, are propagating modes.

The absorption enhancement suggests the possibility of achieving enhanced light emission at a narrow band.[1,3] To achieve emission, we heat the PBG sample thermally, using an external heater. The sample is mounted with a good thermal contact to the heater, and its temperature is measured with a calibrated thermal resistor. The temperature reading is accurate to better than $\Delta T = 1$ K. To minimize thermal heating of the air and convection, we place the sample in a vacuum chamber actively pumped to $\leq 10^{-5}$ Torr. For power-density measurements, a commercially available powermeter calibrated to better than 5% is used. The emission collected from the sample is within a solid angle of $\sim 1.7\pi$.

In Fig. 2, the measured emission spectra are shown for $T = 500, 600, 660, 720$ K. The measurement is performed with a standard Fourier-transform infrared spectrometer from $\lambda = 1$–16 μm.[1,12] The emission is strongly suppressed for $\lambda \geq 10$ μm, has a broad shoulder at $\lambda \approx 5$–9 μm, and exhibits three sharp peaks at $\lambda = 3.3, 3.8, 4.25$ μm (indicated by black arrows). The peak wavelengths agree with the allowed-mode transmission–absorption peaks to within $\Delta\lambda = 0.2$ μm. This excellent agreement shows that the sharp emission is from the first and second allowed modes. Furthermore, all three peaks increase at a much faster rate than the broad one and are pinned at the same wavelengths, independent of temperature. Thus, radiation from inside the PBG sample is emitted preferentially in the narrow allowed modes.

In Fig. 3, the measured power-density spectrum of the PBG sample is compared with that computed for a blackbody cavity radiator at $T = 750$ K. The blackbody radiation follows the Planck radiation law, $M_e(\omega, T) = (\hbar\omega) D_0 F_{\mathrm{BE}}(\omega, T) c/4$.[5,6] Here, $D_0(\omega) = \omega^2/\pi^2 c^3$ is the free-space density of states, $F_{\mathrm{BE}}(\omega, T) = [\exp(\hbar\omega/k_b T) - 1]^{-1}$ is the Bose–Einstein distribution function, and c is the speed of light. In the bandgap, PBG emission is suppressed and is below the blackbody emission. However, PBG emission in the peak regime is found to exceed that of the blackbody by $\sim 300\%$. The combined suppression in the bandgap and enhancement in the allowed bands lead to a PBG emission spectrum with a narrow linewidth, i.e., a full width at half-maximum of $\Delta\lambda(\mathrm{FWHM}) \approx 1.8$ μm. For comparison, a blackbody spectrum at $T = 750$ K has a much broader linewidth of $\Delta\lambda(\mathrm{FWHM}) \approx 4.5$ μm. Given the $\leq 5\%$ experimental uncertainty of the power and temperature values, the experimental finding of emission enhancement is a real phenomenon.

It has been shown that the spectral radiance of a high-dielectric-index (n) medium can exceed that of the blackbody by n^2.[13] Here, $M_{\mathrm{dielectric}}(\omega, T) = (\hbar\omega) D_{\mathrm{dielectric}}(\omega) F_{\mathrm{BE}}(\omega, T) c/4$, and $D_{\mathrm{dielectric}}(\omega) = n^2 D_0(\omega)$ is the density of states inside the high-index medium. However, total internal reflection prohibits the propagation of certain modes (the evanescent modes) into free space, and the escaping efficiency (α) is inversely proportional to n^2, i.e., $\alpha_{\mathrm{dielectric}} = 1/n^2$. An evanescent coupling method of extracting radiation from such forbidden modes has been successfully demonstrated.[13]

For the specific photonic-crystal medium discussed here, the situation is different. At the first and second allowed bands, the density of state is enhanced because of its narrow bandwidth, i.e., flat dispersion.[9] Furthermore, the first and second bands are propagating Bloch modes, allowing for the extraction of PBG radiation into free space. Therefore, it is reasonable to describe PBG emission into a free space as

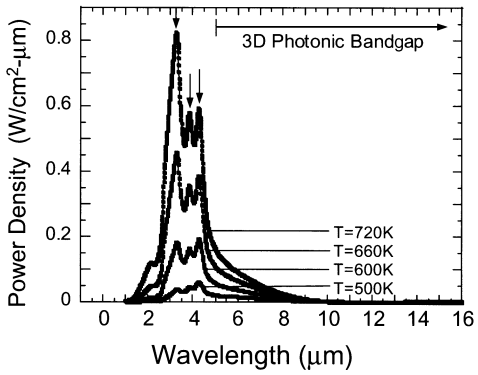

Fig. 2. Measured thermal emission spectra taken at different T values. The emission is strongly suppressed for $\lambda \geq 10$ μm. Meanwhile, it exhibits three sharp peaks in the absorption–transmission bands $\lambda = 3.3, 3.8, 4.25$ μm (arrows).

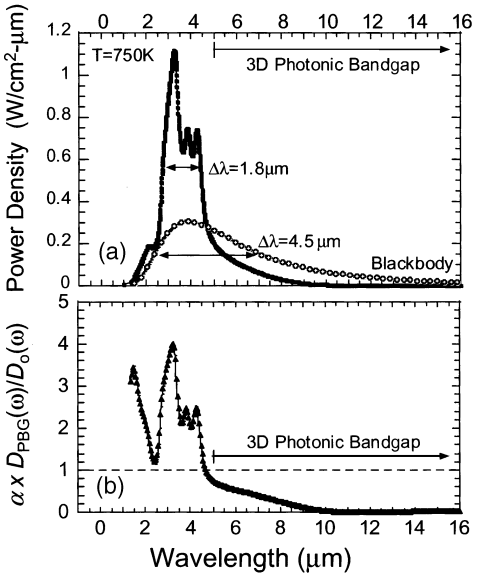

Fig. 3. (a) Comparison of emission power density between the 3D PBG sample and a blackbody cavity radiator at $T = 750$ K. The PBG emission exhibits a narrow FWHM of $\Delta\lambda \approx 1.8$ μm. For $\lambda = 3.3$–4.25 μm, the PBG emission is experimentally observed to exceed that computed for a blackbody. The experimental uncertainty in power and temperature values is less than 5%. (b) Ratio of the PBG density of states, $D_{\mathrm{PBG}}(\omega)$, to the free-space density of states, $D_0(\omega)$. The radiation transfer efficiency from the heated PBG sample to free space is denoted α_{PBG}. The dashed line indicates the free-space density-of-state value.

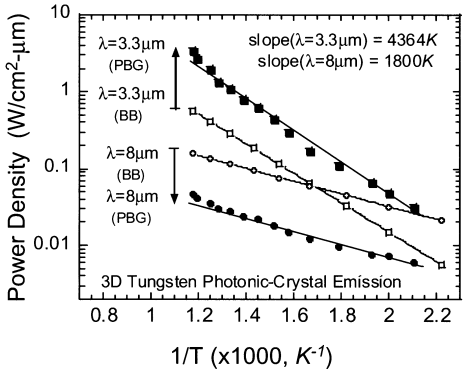

Fig. 4. Semilog plot of the emission power density versus $1/T$ for both the PBG sample and a blackbody (BB). At $\lambda = 8\ \mu$m, the PBG emission intensity is strongly reduced yet exhibits a slope similar to that of the blackbody. At $\lambda = 3.3\ \mu$m, the PBG emission intensity is enhanced and the slope also agrees with that predicted for a blackbody, $\approx 14,400/3.3\ [\mu\text{m}] \approx 4364$ K.

$M_{\text{PBG}}(\omega, T) = \alpha_{\text{PBG}}(\hbar\omega) D_{\text{PBG}}(\omega) F_{\text{BE}}(\omega, T) c/4$. Here, α_{PBG} and $D_{\text{PBG}}(\omega)$ are the extraction efficiency and the density of state of the PBG sample, respectively. As tungsten's dielectric function is frequency dependent and contains an imaginary part,[9] it remains a challenge to compute $D_{\text{PBG}}(\omega)$ for our 3D tungsten PBG sample. However, the density-of-state enhancement may be experimentally deduced by comparison of the PBG's and the blackbody's spectral radiance. The ratio is given by $M_{\text{PBG}}/M_e = \alpha_{\text{PBG}}[D_{\text{PBG}}(\omega)/D_0(\omega)]$ and is shown in Fig. 3(b). The dashed line indicates the free-space density-of-state value. Indeed, the PBG density of states is suppressed in the bandgap and enhanced by ~300% in the allowed bands.

As the density of state in a PBG sample is structure dependent, the same enhancement factor should also be observed at other temperatures. To verify this, we plot the emission power density for both the PBG sample and a blackbody in Fig. 4 for temperatures $T = 475$–850 K. At $\lambda = 8\ \mu$m, the PBG emission (filled circles) is strongly reduced yet exhibits a slope (S) similar to that for the blackbody (open circles). At these temperatures, $\hbar\omega/k_b T >> 1$ and the Bose–Einstein distribution function becomes $F_{\text{BE}} \cong \exp - (S/T[K])$. The slope is given by $S[K] \cong 14400/\lambda[\mu\text{m}]$ and is 1800 K at $\lambda = 8\ \mu$m for a blackbody cavity radiator. At $\lambda = 3.3\ \mu$m, the PBG emission (filled squares) is enhanced and the slope also agrees, within $\pm 10\%$, with that predicted from the Bose–Einstein distribution, $S \cong 14,400/3.3\ [\mu\text{m}] = 4364$ K.[6] This agreement of the experimental and theoretical slopes shows that the temperature-dependent part of the PBG emission can be described by $F_{\text{BE}}(\omega, T)$. Moreover, the temperature-independent part of it can be described by $D_{\text{PBG}}(\omega)$.

In summary, a 3D tungsten photonic-crystal sample is thermally excited and exhibits emission at a narrow band. The sharp emission is experimentally shown to exceed the free-space Planck radiation. It is proposed that an enhanced density of state associated with the propagating electromagnetic Bloch waves is responsible for the observed effect. As our PBG sample is a highly dispersive medium,[9] further theoretical formulation may be necessary to provide insight into whether the observed emission is thermal equilibrium radiation.[14]

The authors thank J. Bur, J. Rivera, M. Tuck, and the Microelectronics Development Laboratory for technical support. The work at Sandia National Laboratories is supported through the U.S. Department of Energy (DOE). Sandia is a multiprogram laboratory operated by Sandia Corporation, a Lockheed Martin Company, for the DOE under contract DE-AC04-94AL 85000. S. Y. Lin's e-mail address is slin@sandia.gov.

References

1. J. G. Fleming, S. Y. Lin, I. El-Kady, R. Biswas, and K. M. Ho, Nature **417,** 52 (2002).
2. S. Y. Lin, J. G. Fleming, E. Chow, J. Bur, K. K. Choi, and A. Goldberg, Phys. Rev. B **62,** R2243 (2000).
3. S. Y. Lin and J. G. Fleming, Proc. SPIE **5000,** 1 (2003).
4. T. J. Coutts and M. C. Fitzgerald, Sci. Am. **279,** 90 (1998).
5. A. Yariv, *Quantum Electronics* (Wiley, New York, 1989), Chap. 5, pp. 98–100.
6. E. L. Dereniak and G. D. Boreman, *Infrared Detectors and Systems*, Series in Pure and Applied Optics (Wiley, New York, 1996), Chap. 2.
7. S. Y. Lin, J. G. Fleming, D. L. Hetherington, B. K. Smith, R. Biswas, K. M. Ho, M. M. Sigalas, W. Zubrzycki, S. R. Kurtz, and J. Bur, Nature **394,** 252 (1998).
8. E. Ozbay, B. Temelkuran, M. M. Sigalas, G. Tuttle, C. M. Soukoulos, and K. M. Ho, Appl. Phys. Lett. **69,** 3797 (1996).
9. Z. Li, I. El-Kady, K. M. Ho, S. Y. Lin, and J. G. Fleming, J. Appl. Phys. **93,** 38 (2003).
10. K. Sakoda, Opt. Exp. **4,** 167 (1999), http://www.opticsexpress.org.
11. S. Y. Lin, J. G. Fleming, Z. Y. Li, I. El-Kady, R. Biswas, and K. M. Ho, J. Opt. Soc. Am. B **20,** 1538 (2003).
12. J. G. Fleming and S. Y. Lin, Opt. Lett. **24,** 49 (1999).
13. J. L. Pan, H. K. H. Choy, and C. G. Fonstad, Jr., IEEE Trans. Electron. Devices **47,** 241 (2000).
14. L. D. Landau and E. M. Lifshitz, *Electrodynamics of Continuous Media* (Pergamon, New York, 1984), Sect. 80.

Highly efficient light emission at $\lambda = 1.5\ \mu$m by a three-dimensional tungsten photonic crystal

S. Y. Lin, J. G. Fleming, and I. El-Kady

Sandia National Laboratories, MS 0603, P.O. Box 5800, Albuquerque, New Mexico 87185

Received March 14, 2003

For what is believed to be the first time, a three-dimensional tungsten photonic crystal is demonstrated to emit light effectively at wavelength $\lambda = 1.5\ \mu$m. At a bias of $V = 7$ V, the thermal emission exhibits a full width at half-maximum of $\Delta\lambda = 0.85\ \mu$m. Within this narrow band, the emitted optical power is 4.5 W and the electrical-to-optical conversion efficiency is ~22% per emitting surface. This unique emission is made possible by a large, absolute bandgap in the infrared λ and flat photonic dispersion near the band edges and in a narrow absorption band. © 2003 Optical Society of America

OCIS codes: 270.0270, 250.0250.

Light emitters operating in the near-infrared wavelength regime ($\lambda = 1$–$2\ \mu$m) are almost universally based on semiconductor materials.[1] To vary the emission wavelength, researchers often apply the principle of electronic bandgap engineering to obtain the appropriate electronic bandgap energy.[2] A thermal radiator can also emit light in the near infrared, if it is heated to a temperature of $T \geq 1500$ K.[3] Nonetheless, this radiation process is not efficient at producing narrowband emission. For example, a blackbody thermal radiation spectrum at $T = 1500$ K has a full width at half-maximum (FWHM) of $\Delta\lambda = 2.3\ \mu$m, and ~75% of its total emission power is distributed in the mid infrared ($\lambda > 2\ \mu$m). However, it has been suggested that the principle of photonic bandgap engineering can be applied to modify the thermal radiation pattern.[4–6] In particular, a complete photonic bandgap is effective in trapping light in the infrared and thus reduces radiation loss in this regime. Second, nearly flat-band photonic dispersion (ω versus k, where $d\omega/dk \approx 0$) has been proposed to facilitate light emission at a narrow band.[4] Flat photonic dispersion can be found at the photonic band edges and at a narrow allowed band. If both effects are successfully implemented, a thermal emitter with a narrow band and high efficiency can be realized.

In this Letter a tungsten three-dimensional (3D) photonic crystal is demonstrated to emit light effectively at wavelength $\lambda = 1.5\ \mu$m. At a bias of $V = 7$ V, the emission exhibits a FWHM of $\Delta\lambda = 0.85\ \mu$m. Within this narrow band, the emitted power is 4.5 W and the electric-to-optical conversion efficiency is ~22% per emitting surface. The high efficiency and high power emission at $\lambda = 1.5\ \mu$m are attributed to two unique photonic bandgap effects. The large, absolute photonic bandgap is effective in suppressing mid-infrared emission ($\lambda > 2\ \mu$m), and, at the same time, the emission is enhanced in a narrow band because of enhanced density of photon states, $D(\omega)$.

The 3D tungsten photonic crystal is fabricated by use of a modified silicon process. In the first step, a layer of silicon dioxide is deposited, patterned, and etched to create a mold. The mold is then filled with a 500-nm-thick chemical-vapor-deposited tungsten film. The structure is then planarized by use of a chemical–mechanical polishing process. At the end of the process, the silicon dioxide is released from the substrate and the sample is a freely standing thin film. In Fig. 1, a scanning electron micrograph image of the fabricated sample is shown. The one-dimensional rods represent the shortest ⟨110⟩ chain of atoms in a diamond lattice. The stacking sequence is such that every four layers constitute a unit cell.[7,8]

The experimental reflection, transmission, and emission spectra of the 3D photonic crystal are taken with a standard Fourier-transform infrared spectrometer at $\lambda = 0.8$–$15\ \mu$m.[9,10] For the emission measurement, the sample is mounted so that it is thermally and electrically isolated from its surroundings. Thermal heating of the air and convection are minimized by placing the sample in a vacuum chamber pumped to $\sim 10^{-5}$ Torr. For power density measurements, a commercially available Gentec powermeter, calibrated to within 5%, is used.

In Fig. 2, the reflection (black curve) and transmission (blue curve) spectra of an eight-layer 3D photonic-crystal sample are shown. The high reflectance for $\lambda > 3\ \mu$m indicates the existence of a large photonic bandgap. Such a 3D metallic bandgap is a complete bandgap and is effective (~30 dB/unit cell) in blocking light fully in all directions and for both polarizations.[4] The reflectance shows a dip at $\lambda \sim 2.5\ \mu$m

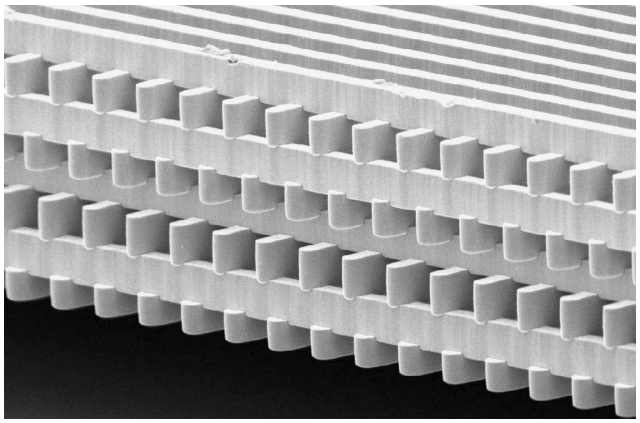

Fig. 1. Scanning electron microscope image of a 3D tungsten photonic crystal. Within each layer, the one-dimensional rod width is 0.5 μm and the rod-to-rod spacing is 1.5 μm. The sample is a freely standing thin film.

0146-9592/03/181683-03$15.00/0

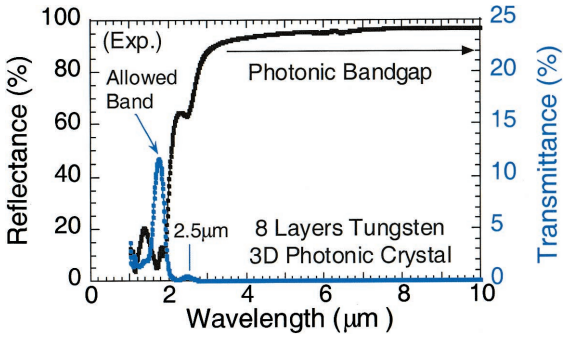

Fig. 2. Measured reflectance (black) and transmission (blue) spectra for a 3D tungsten photonic crystal sample. The photonic bandgap is at $\lambda > 3\ \mu$m. There is a small transmittance peak at $\lambda \sim 2.5\ \mu$m and a high transmittance peak at $\lambda \sim 1.75\ \mu$m.

and drops sharply to a value of <10% at $\lambda \sim 2\ \mu$m. Correspondingly, the transmittance is low in the bandgap and exhibits a small peak at $\lambda \sim 2.5\ \mu$m and a sharp peak of ~10% at $\lambda \sim 1.75\ \mu$m. The sharp transmission band is indicative of flat photonic dispersion (i.e., ω versus k) associated with a narrow allowed band.[11] In the following, the experimental data are compared with results of a modified transfer-matrix calculation.[11] This new calculation method can handle the complex dielectric constant of tungsten material in our 3D photonic crystal.

In Fig. 3, computed results of the reflection (black curve), transmission (blue curve) and absorption (red curve) spectra for the same sample are shown. The computed reflection and transmission spectra agree well with the measured ones. In particular, the reflectance is high for $\lambda > 3\ \mu$m (first photonic bandgap) and shows a slight dip at $\lambda \sim 2.5\ \mu$m, a peak at $\lambda \sim 2.2\ \mu$m (second photonic bandgap), and finally a sharp drop at $\lambda \sim 2\ \mu$m. The first and second band edges are closely spaced, leading to a reflectance dip, a transmission peak, and finely resolved doublet absorption peaks, all at $\lambda \sim 2.5\ \mu$m. The strong absorptance of ~40% is due to an enhanced photon density of states, $D(\omega)$, at the band edges.[12,13] Additionally, there exists a narrow transmission peak at $\lambda \sim 1.7\ \mu$m and a corresponding absorption band at $\lambda_2 \sim 1.5$–$1.9\ \mu$m (indicated by red arrows). The high absorptance of ~80% at $\lambda \sim 1.5$–$1.9\ \mu$m is due to both high $D(\omega)$ and high tungsten material absorption at these wavelengths.[14]

To achieve emission, we biased the photonic-crystal sample by applying a voltage across the sample and heating it through joule heating. The emission intensity is uniform across the entire sample, as shown in the inset of Fig. 4(b). The photograph shows a slight visible emission at the tail of the emission peak. In Figs. 4(a) and 4(b), emission spectra taken at low and intermediate bias, respectively, are shown. At $V = 0.25$ V, the emission spectrum consists of broad emission near $\lambda \sim 3$–$6\ \mu$m and a peak at $\lambda_1 \sim 2.5\ \mu$m. As V is increased to 0.5 and then to 0.75 V, an additional emission peak appears at $\lambda_2 \sim 1.9\ \mu$m. The broad emission is attributed to thermal emission from the surface layer of the sample, which experiences little photonic bandgap effect. The two sharp peaks correspond well to the absorption peaks predicted in Fig. 3. As $D(\omega)$ affects both the emission[15] and the absorption rate, the close agreement of emission and absorption peaks is expected.

The intensity evolution of both peaks is worth noting. At $V = 0.25$ and $V = 0.5$ V, the λ_2 emission is weaker than the λ_1 emission. The respective intensities of the emissions become nearly equal at $V = 0.75$ V, and eventually λ_2 emission dominates the spectrum at $V = 1$–3 V [Fig. 4(b)]. In short, as V is increased, or equivalently as the input electric power is raised, the λ_2 peak increases at a faster rate than the λ_1 peak. A similar finding was also observed previously but at a longer wavelength of $\lambda \sim 4\ \mu$m.[16] It is noted that, while the λ_1 peak remains at the same

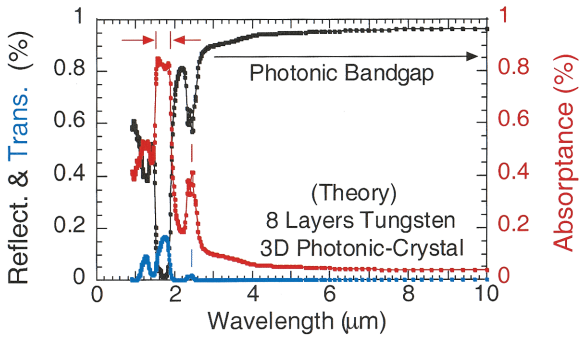

Fig. 3. Computed reflectance (Reflect., black), transmission (trans., blue), and absorption (red) spectra for a 3D tungsten photonic-crystal sample. The computed positions of the photonic bandgap and band edge agree with the measured ones. The absorptance is suppressed in the bandgap regime ($\lambda > 3\ \mu$m) and exhibits a fine doublet peak at $\lambda_1 \sim 2.5\ \mu$m and a narrow absorption band at $\lambda_1 \sim 1.5$–$1.9\ \mu$m.

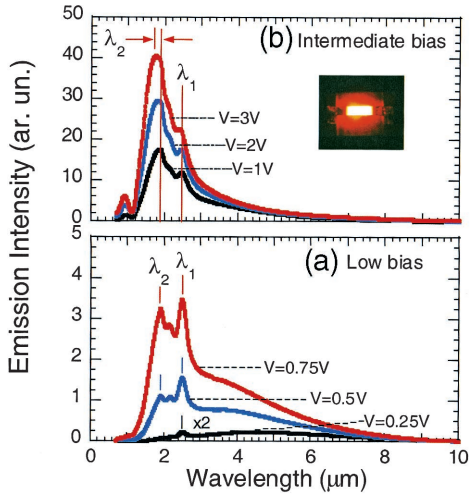

Fig. 4. Photonic-crystal emission spectra taken at (a) low ($V = 0.25$–0.75 V) and (b) intermediate ($V = 1$–3 V) bias. At low bias, the emission spectrum consists of a broad emission peak ($\lambda \sim 3$–$6\ \mu$m) and two sharp emission peaks at $\lambda_1 \sim 2.5\ \mu$m and $\lambda_2 \sim 1.9\ \mu$m. At intermediate bias, the λ_2 peak dominates the emission and also shifts slightly to $\lambda_2 \sim 1.75\ \mu$m. The photograph in the inset of (b) shows a slight visible emission at the tail of the emission peak. It is evident that emission across the entire sample is uniform.

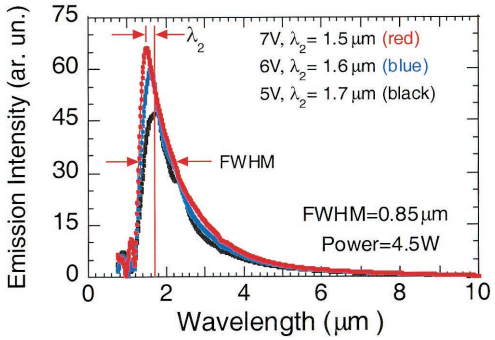

Fig. 5. Photonic-crystal emission spectra taken at high biases, $V = 5$ V (black), $V = 6$ V (blue), and $V = 7$ V (red). The emission wavelength shifts from $\lambda \sim 1.7$ μm at $V = 5$ V to $\lambda \sim 1.5$ μm at $V = 7$ V, corresponding to wavelength scanning of a narrow absorption band. At $V = 7$ V, the emission has a FWHM of $\Delta\lambda_1 \sim 0.85$ μm and an emission power of 4.5 W within the narrow band.

wavelength as V is increased, the λ_2 peak is shifted slightly to a lower wavelength at $\lambda_2 \sim 1.9$–1.75 μm. This wavelength shifting is further examined below at higher biases.

In Fig. 5, the emission spectra taken at even higher biases of $V = 5, 6, 7$ V are shown. The λ_1 peak becomes an indiscernible weak shoulder. Meanwhile, the λ_2 peak continues to shift from $\lambda_2 \sim 1.7$ μm at $V = 5$ V to $\lambda_2 \sim 1.5$ μm at $V = 7$ V. The wavelength shifting from $\lambda_2 \sim 1.9$ μm to $\sim$1.5 μm corresponds to scanning of the absorption band (indicated in Fig. 3 by the red arrows) as V is increased. At $V = 7$ V, the emission has a FWHM of $\Delta\lambda_1$(FWHM) ~ 0.85 μm. Within this narrow band, optical power of 4.5 W is measured from the top sample surface, with a collection angle of 1.8π. The corresponding electrical-to-optical conversion efficiency is 22% per emitting surface, or, equivalently, a total efficiency of 44%. It is noted that a blackbody spectrum at $T = 1500$ K has a much broader linewidth of $\Delta\lambda$(FWHM) ~ 2.3 μm. The observed spectral linewidth narrowing is caused by the combined suppression of emission in the bandgap and enhanced emission at a narrow band.[16] In the bandgap regime, light is trapped and therefore there is no loss of energy in the mid infrared. This strong suppression of light leakage in the mid infrared is also responsible for the observed high conversion efficiency at a narrow band. As the sample has a surface area of $A = 0.16$ cm^2, the emitted optical power density is large, $\sim$27 W/cm^2, at a narrow band. Optical emission at this power may be promising for pumping near-infrared solid-state lasers.[17]

The operating principle of this class of tungsten photonic-crystal light emitter is different from that of the conventional LED. A LED is based on semiconductor technology and relies on radiative recombination of electrons and holes to achieve light emission. Quite differently, a tungsten photonic-crystal emitter is based on metals. It achieves narrowband light emission through spectral modification of thermal radiation. The challenge for realizing such a photonic-crystal emitter is in nanofabrication. To achieve visible light emission, our metallic structure needs a minimum feature size of $\sim$100 nm. However, one of the great advantages of this photonic-crystal approach is its ease of wavelength scalability. For the same tungsten material, we can vary the emission wavelength from $\sim$5 μm to 500 nm by simply scaling the minimum feature size from $\sim$1 μm down to 100 nm.

In summary, a tungsten 3D photonic crystal has been successfully demonstrated to emit light preferentially at wavelength $\lambda = 1.5$ μm. The tungsten photonic-crystal light emitter exhibits high efficiency of $\sim$22% per surface and high output power of 4.5 W. This demonstration of high efficiency and high power is made possible by the presence of an absolute bandgap in the infrared and enhanced density of photon states near the band edges and in a narrow absorption band.

The authors thank J. Bur, M. Tuck, and J. Rivera for technical support. The work at Sandia National Laboratories is supported through the U.S. Department of Energy (DOE). Sandia is a multiprogram laboratory operated by Sandia Corporation, a Lockheed Martin Company, for the DOE under contract DE-AC04-94AL 85000. S.-Y. Lin's e-mail address is slin@sandia.gov.

References

1. G. P. Agrawal and N. K. Dutta, *Long Wavelength Semiconductor Lasers* (Van Nostrand Reinhold, New York, 1986).
2. G. Bastard, *Wave Mechanics Applied to Semiconductor Heterostructures* (Halsted, New York, 1988).
3. E. L. Dereniak and G. D. Boreman, *Infrared Detectors and Systems*, Wiley Series in Pure and Applied Optics (Wiley, New York, 1996), Chap. 2, pp. 56–68.
4. J. G. Fleming, S. Y. Lin, I. El-Kady, R. Biswas, and K. M. Ho, Nature **417,** 52 (2002).
5. S. Y. Lin, J. G. Fleming, E. Chow, J. Bur, K. K. Choi, and A. Goldberg, Phys. Rev. B **62,** R2243 (2000).
6. C. M. Cornelius and J. P. Dowling, Phys. Rev. A **59,** 4736 (1999).
7. K. M. Ho, C. T. Chan, C. M. Soukoulis, R. Biswas, and M. Sigalas, Solid State Commun. **89,** 413 (1994).
8. E. Ozbay, B. Temelkuran, M. M. Sigalas, G. Tuttle, C. M. Soulokous, and K. M. Ho, Appl. Phys. Lett. **69,** 3797 (1996).
9. S. Y. Lin, J. G. Fleming, D. L. Hetherington, B. K. Smith, R. Biswas, K. M. Ho, M. M. Sigalas, W. Zubrzycki, S. R. Kurtz, and J. Bur, Nature **394,** 252 (1998).
10. J. G. Fleming and S. Y. Lin, Opt. Lett. **24,** 49 (1999).
11. Z. Li, I. El-Kady, K. M. Ho, S. Y. Lin, and J. G. Fleming, J. Appl. Phys. **93,** 38 (2003).
12. N. A. R. Bhat and J. E. Sipe, Phys. Rev. E **64,** 56604 (2001).
13. S. John and T. Quang, Phys. Rev. A **50,** 1764 (1994).
14. M. A. Ordal, L. L. Long, R. J. Bell, S. E. Bell, R. R. Bell, R. W. Alexander, Jr., and C. A. Ward, Appl. Opt. **22,** 1099 (1983).
15. E. Merzbacher, *Quantum Mechanics*, 2nd ed. (Wiley, New York, 1970), Chap. 18, Sect. 8.
16. S.-Y. Lin, J. G. Fleming, and I. El-Kady, Appl. Phys. Lett. **83,** 593 (2003).
17. C. D. Nabors, J. Ochoa, T. Y. Fan, A. Sanchez, H. K. Choi, and G. W. Turner, IEEE J. Quantum Electron. **31,** 1603 (1995).

Efficient light emission by a three-dimensional, all-metallic photonic crystal and its energy consequences

S.Y. Lin and J.G. Fleming

MS 0603, Sandia National Laboratories, P.O. Box 5800, Albuquerque, NM 87185

ABSTRACT

A review is given on the recent progress in three-dimensional (3D) all-metallic photonic-crystals in the near- and mid-infrared wavelengths. Results of optical spectroscopy of the sample will be described. Unique light emission characteristics at a narrow band from the photonic-crystal will also be presented. This new class of 3D all-metallic photonic-crystal is promising for thermal photo-voltaic power generation and for lighting application.

Keywords: Photonic Crystal, Photonic Band Gap, Metallic Structure, Thermal Emission

1. INTRODUCTION

There is an emerging interest in all-metallic three-dimensional (3D) photonic-crystal for energy applications [1]. It is suggested that the principle of "*photonic band gap engineering*" may be applied to modify the broadband nature of thermal radiation [1-3]. In particular, a complete 3D photonic band-gap is effective in trapping light in the infrared [1,2], thus reducing radiation-loss in this regime. As a comparison, a 2D surface structure could not trap light fully in all three dimensions and, consequently, loss of light always occurs. Secondly, a nearly flat-band photonic dispersion (ω vs k, where $d\omega/dk \approx 0$) is proposed to facilitate light emission at a narrow band [1]. Flat photonic-dispersion can be found near the photonic band-edges and at a narrow allowed band. If both effects are successfully implemented, a thermal emitter with a narrow band and high efficiency can be realized.

In this paper, a 3D metallic photonic-crystal is realized and a selective absorption enhancement near the photonic band-edge is observed. It is shown that the use of metal can generate a large, absolute, 3D photonic band-gap for light trapping. Combining both effects, efficient light emission at a narrow near-infrared band is experimentally demonstrated. This emission characteristic is shown to have important consequence for thermal photovoltaic (TPV) power generation and for lighting application.

Photonic Crystal Materials and Devices, Ali Adibi, Axel Scherer, Shawn Yu Lin, Editors,
Proceedings of SPIE Vol. 5000 (2003) © 2003 SPIE · 0277-786X/03/$15.00

2. METHODS OF 3D STRUCTURE FABRICATION

The 3D tungsten photonic-crystal is fabricated using two different methods. The first one is the, so-called, mold process [1]. A SEM image of the sample is shown in Fig. 1 (a). The starting structure is a fabricated polysilicon/SiO2 3D photonic crystal. Details on the fabrication of it are given in reference-4. As the first step, the polysilicon in a 3D silicon photonic crystal was removed using a KOH etch. Over-etch during the KOH process results in the formation of a "V" structure on the bottom of the layer contacting the substrate. This is due to etching of the underlying substrate. Secondly, the blanket CVD tungsten film does not adhere to silicon dioxide and was therefore grown on a 50nm thick TiN adhesion layer. The chemical vapor deposition of tungsten results in films of very high purity; the film resistivity was ~10 microOhm-cm. The step coverage of the deposition process is not 100% and this gives rise to the formation of a keyhole in the center of the more deeply imbedded lines (see Fig.1a). And lastly, excess tungsten on the surface was removed by chemical mechanical polishing and the oxide mold was removed with HF solution.

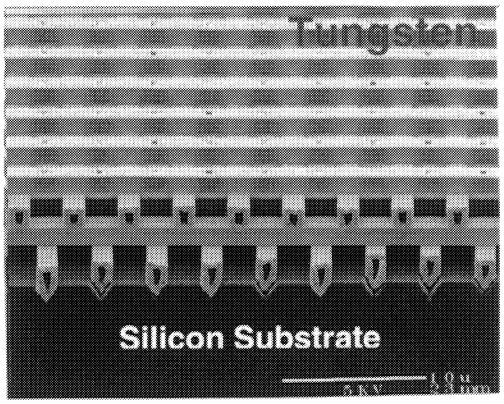

Fig. 1(a) A SEM image of a five-layer tungsten 3D photonic-crystal structure, fabricated using the mold process. The V-shaped at the bottom layer is due to an over-etch of the silicon substrate.

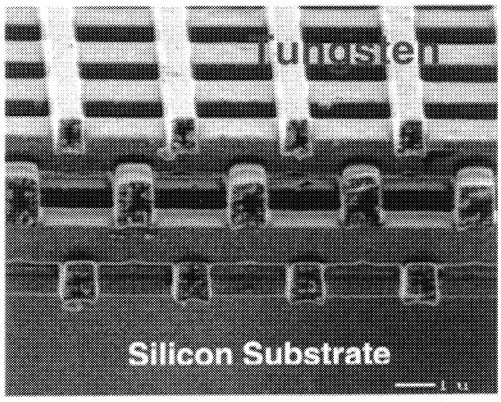

Fig. 1(b) A SEM image of a six-layer tungsten 3D photonic-crystal structure, fabricated using the modified mold process.

The second method is based on a modified mold process [5]. A SEM image of the representative sample is shown in Fig. 1 (b). In the first step, a layer of silicon dioxide is deposited using plasma-enhanced deposition. The thickness of this oxide layer is the same as that of the final tungsten layer thickness. Photolithography and etching are then employed to create a mold. The mold is then filled with a 500nm thick chemical vapor deposited tungsten film. A thin 25nm TiN layer is used as an adhesion layer. The structure is then planarized and the overburden of W is removed using a CMP (Chemical Mechanical Polishing) process. Since planarity is maintained, the entire process can be repeated as many times as needed. At the end of the process the die are diced into strips of the desired dimension and released from the substrate using HF. HF does not attack

either the tungsten or TiN. We also typically ensure that the initial oxide layer is thicker than the tungsten layer so that an oxide release layer remains between the first tungsten layer and the silicon substrate. The 1D rods represent the shortest <110> chain of atoms in a diamond lattice. The rod-to-rod spacing is a=1.5μm, the rod width is w=0.5μm and rod height h~0.75μm. The stacking sequence is such that every four layers constitute a unit-cell [6,7]. It should be emphasized that all these standard processes were performed on commercially available tools.

3. EXPERIMENTAL MEASUREMENTS: REFLECTION, TRANSMISSIONA ND ABSORPTION

The experimental reflection (R) and transmission (T) spectra of the 3D tungsten photonic crystal are taken using a standard Fourier-Transform-Infrared-Spectrometer (FTIR) for wavelengths from λ=1-20 μm [4,8]. The absorption (A) spectrum is measured using a photo-acoustic method [1,9]. The photo-acoustic cell is commercially available and can be easily adapted to our FTIR system. To obtain absolute values of R and A, a proper normalization of the sample-signal to a reference-one is performed. Reflectance from a silver mirror (R>98% at infrared λ) is used as our reflectance reference. The absorptance-reference is taken from a black-carbon absorber, which has an absorptance of 0.99 for λ=2-20 μm.

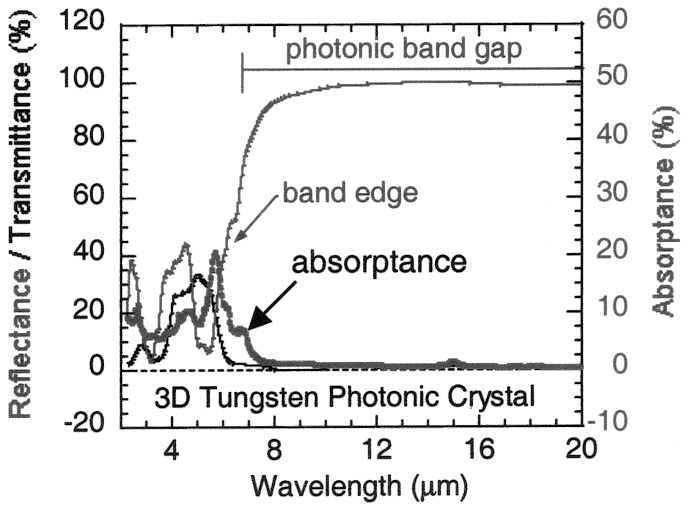

Fig.2 The experimental reflectance (red), transmittance (black) and absorptance (blue) spectra, taken from a 3D tungsten photoni-crystal sample. The photonic band-gap and band-edge are at λ>8μm and λ~6μm, respectively. The absorptance peaks near the band-edge, exhibiting a nearly ten times absorption enhancement.

In Fig.2, we show R, T and A for a tungsten 3D photonic-crystal sample. The reflectance exhibits a large photonic band-gap for λ~8-20μm, a band-edge at λ~6μm and allowed band oscillations for λ<5μm. The absorptance shows a pronounced peak of 22% at the band-edge of λ=5.8μm ad a low absorptance in the band-gap. The simultaneous

suppression of absorption at the band-gap and enhancement of it at the band-edge is important for thermal emission modification. The origin of the absorption-rate enhancement has been investigated by theoretically computing R, T and A using a newly developed Transfer-Matrix method [9]. The method can effectively handle the presence of a complex dielectric function in a metallic 3D photonic-crystal. It is concluded that there are three criteria for achieving absorption enhancement. First, the enhancement always occurs at the band-edge where group velocity of light approaches zero, leading to a longer photon-matter interaction time [11-13]. To enhance the photon-matter interaction length, light is to be propagated through a thicker sample (more layers) and, thus, absorption is enhanced. Finally, the presence of intrinsic absorption is necessary. Absorption enhancement is possible only when there is a finite material absorption for the density of photon-states to enhance it from.

4. PHOTONIC-CRYSTAL THERMAL EMISSION

To achieve emission, the sample is biased by applying a voltage across the photonic-crystal sample and is heated through Joule heating. The sample is mounted so that it is thermally and electrically isolated from its surroundings. To minimize thermal heating of the air and convection, the sample is placed in a vacuum chamber actively pumped to ~10 m-torr. For spectroscopy measurements, the emitted light from the top-surface of our sample first passes through an infrared optical window, an aperture, and a long wavelength ZeSe lens before it enters the FTIR spectrometer. For power density measurements, a commercially available Gentec power meter is first used to measure the power.

In Fig. 3, emission spectra taken from two different samples are shown. The first sample has a lattice constant of a=2.8 μm, a rod-width of w=0.8 μm. Its peak emission wavelength is at λ=4μm and the full-width-half maximum is Δλ (FWHM)=1.8μm. The second sample has a lattice constant of a =1.5 μm, a rod-width of w=0.5 μm, a peak emission wavelength at λ=1.8μm and a full-width-half maximum is Δλ (FWHM)=1.0μm. It follows from Fermi's golden rule that emission rate is proportional to the available density of photon-states $D(\omega)$[14]. The spectral line-width narrowing is the result of a simultaneous suppression and enhancement of $D(\omega)$ in the band gap and near the band-edge, respectively. Thus, a 3D metallic photonoc-crystal allows for spectral-shaping without loss of energy. This conclusion is further supported by the observed high electrical-to-optical power conversion efficiency of ~45% for both samples. Also shown in the same figure is a simulated absorptance (red color) and reflectance (blue color), done for a 3D gold photonic crystal sample with a =0.4 μm and w=0.13 μm. Gold material is used to properly balance the real and imaginary part of material's dielectric constants in this wavelength regime. The reflectance shows the existence of a photonic band gap for λ>800nm, a band edge at λ~700nm. Correspondingly, the absorptance exhibits a well-defined peak in the blue, λ~400nm.

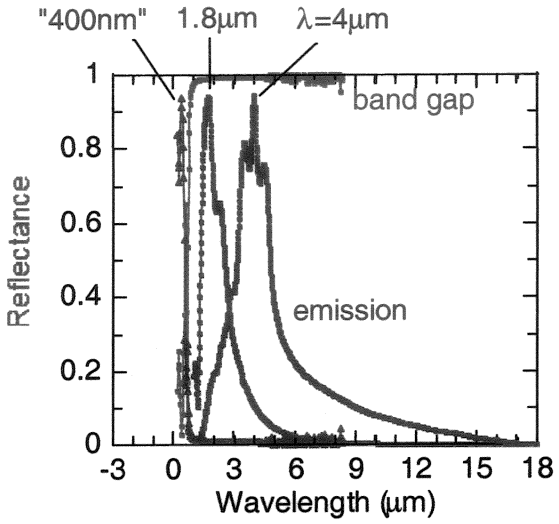

Fig.3 Experimental emission curves, showing the wavelength-scalability of our 3D metallic photonic-crystal sample. The emission peak at λ~4μm and λ~1.8μm are for samples with lattice constant of a=2.8 and 1.5μm, respectively. A simulation has also been perform for a sample with a=0.4μm. The corresponding absorptance peak is at the blue, λ=400nm.

5. POTENTIAL LIGHTING AND TPV APPLICATIONS

From Fig.3, it is clear that visible light emission with high efficiency is possible by simply reducing the rod size to w=100-200nm,. The challenge for realizing such a photonic-crystal emitter is then in nano-fabrication. Current silicon processing can routinely produce feature size of 130nm and 180nm over a twelve-inch silicon wafer. In a year or two, it is reasonable to expect a more mature 90nm feature size technology. A large scale, low cost manufacturing of photonic-crystal filament might become a reality.

On the other hand, TPV application for power generation is more imminent. A TPV system converts thermal radiation energy into electric energy through the use of a photo-voltaic cell [15,16]. A schematic of a TPV system is shown in Fig.4 (a). It typically consists of a thermal emitter, a filter, a window and a photo-voltaic cell. A GaSb photo-voltaic cell is commonly used, as it has a relatively low electronic band gap (λg~1.8μm). The required thermal radiation source temperature is in a more manageable range of T=1500-1800K. It is noted that only the part of thermal radiation energy above the electronic band gap contributes to photo-current generation (shown in figure-4b as the shaded region). The part of radiation energy below the electronic band gap is wasted, leading to low optical-to-electric conversion efficiency. The use of either surface structuring or a filter to reject the unwanted low energy radiation could lead to higher conversion efficiency. Yet, it often reduces the electrical power density as well [15,16].

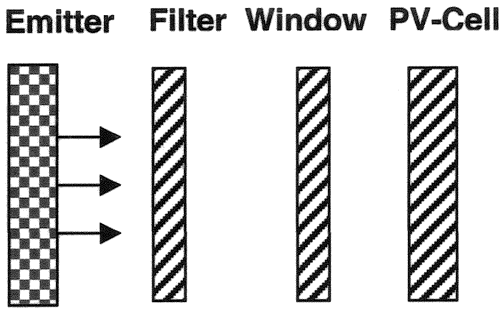

Fig. 4(a) A schematic of a TPV energy conversion system. It consists of a heated emitter, a filter for spectral shaping, a window and a photo-voltaic cell.

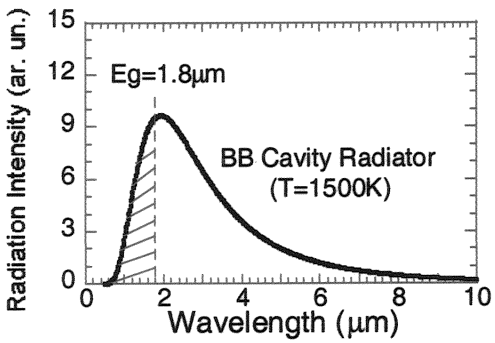

Fig. 4(b) A blackbody cavity radiation spectrum. Only the part of thermal radiation above the electronic band gap, Eg, contributes to photo-current generation.

To achieve both high efficiency and high electric power density, the radiation pattern must be matched to the photo-response of a PV-cell. In practice, a complete 3D photonic band-gap is effective in trapping the otherwise wasted infrared radiation, thus minimizing loss. The peak emission can also be matched to the cell's electronic band gap, maximizing the conversion-efficiency. In other words, the *photonic* band-gap energy is matched to the *electronic* band-gap energy to maximize TPV device performance. This example illustrates a new design freedom, enabled by our capability to independently engineer *electronic* and *photonic band-gap*.

A theoretical modeling has been performed for a photonic-crystal emitter similar to the one shown in Fig.3, but scaled down in wavelength by 30% to obtain a more optimum emission. The model is similar to the one performed by Zenker et. al. [15]. It takes into account both the radiative-recombination of a GaSb cell and a realistic cell reflectance. The modeling result shows an optical-to-electrical efficiency of η=35.5% and electrical power-density of P=7.1Watts/cm^2 at a sample temperature of T~1400K. In comparison, a blackbody radiator at T=1400k delivers a η=12.8% and P=1.4Watts/cm^2.

6. SUMMARY

In summary, a metallic 3D photonic-crystal is successfully demonstrated to emit light efficiently at near-infrared and mid-infrared wavelength. The 3D metallic photonic crystal holds great promises for TPV and lighting applications. Both applications illustrate a new design freedom, enabled by our capability to independently engineer *electronic* and *photonic band-gap*. Moreover, this new class of light emitter can be made to cover a wide range of wavelengths, from infrared to visible.

7. ACKNOWLEDGEMENT

The authors would like to acknowledge Drs I. El-kady, Z. Li and professor K.M. Ho of Iowa State University/Ames National Labs for theoretical support. The authors also like to thank J. Bur, M. Tuck and J. Rivera for technical support. The work at Sandia National Laboratories is supported through DOE. Sandia is a multi-program laboratory operated by Sandia Corporation, a Lockheed Martin Company, for the United States Department of Energy under contract DE-AC04-94AL 85000.

REFERENCES

1. J. G. Fleming, S.Y. Lin, I. El-Kady, R. Biswas and K. M. Ho, ***Nature*** **417**, 52-55 (2002).
2. S.Y. Lin, J. G. Fleming, E. Chow, J. Bur, K.K. Choi and A. Goldberg, ***Phys. Rev. B 62,*** **R2243** (2000).
3. C.M. Cornelius and J. Dowling, ***Phys. Rev.*** **A59**, 4736 (1999).
4. S.Y. Lin, J.G. Fleming, D.L. Hetherington, B.K. Smith, R. Biswas, K.M. Ho, M.M. Sigalas, W. Zubrzycki, S.R. Kurtz and J. Bur, ***Nature*** 394, 252-253 (1998).
5. S.Y. Lin, J.G. Fleming, I. El-Kady, Li Z. Y. Li, and K. M. Ho, Submitted for publication.
6. K.M. Ho, C.T. Chan, C. M. Soukoulis, R. Biswas and M. Sigalas, ***Solid State Comm.*** **89**, 413-416 (1994).
7. E. Ozbay, B. Temelkuran, M.M. Sigalas, G. Tuttle, C.M. Soulokous , and K.M. Ho, ***Appl. Phys. Lett.*** 69, 3797-3799 (1996).
8. S.Y. Lin and J. G. Fleming, ***Optics Letters*** **24**, 49-51 (1999).
9. McClelland, J.F., Jones, R.W., Lou, S., and Seaverson, L.M., A Practical guide to FTIR photoaccoustic spectroscopy, in *Practical sampling teciniques for infrared analysis*, P.B. Coleman, Ed. (CRC Press, Boca Raton, Florida, 1993), Chapter 5.
10. Li Z. Y. Li, I. El-Kady, K. M. Ho, S. Y. Lin and J. G. Fleming, ***Phys. Rev. B,*** *accepted Dec. 2002.*
11. N. A. R. Bhat and J. E. Sipe, ***Phys. Rev. E*** **64**, 56604 (2001).
12. K. Sakoda, ***Optics Express***, **v. 4**, p. 167-176 (1999).
13. S. John and T. Quang, ***Phys. Rev.*** **A 50**, 1764-1769 (1994).
14. E. Merzbacher, "Quantum Mechanics", Ch.18, Sec.8, John, 2nd Edition, Wiley & Sons, New York, 1970.
15. M. Zenker, A. Heinzel, G. Stollwerck, J. Ferber and J. Luther, ***IEEE Trans. Electr. Dev.*** **Vol. 48**, 367-376 (2001).
16. T.J. Coutts, ***Renewable and Sustainable Energy Reviews*** **3**, 77-184 (1999).

Distribution List

1 MS 0972, Andy Boye, 5710
1 MS 0972, Carter Grotbeck, 5725
1 MS 0603, Jim Hudgens, 1713
4 MS 0603, Shanalyn Kemme, 1713
1 MS 0603, Rick McCormick, 1713-1
1 MS 0603, David Peters, 1713-1
1 MS 0570, Eric Shields, 5712
1 MS 0965, Jody Smith, 5712
1 MS 0603, Charles Sullivan, 1742
1 MS 0603, Allen Vawter, 1742

2 MS 9018, Central Technical Files, 8945-1
2 MS 0899, Technical Library, 9616
1 MS 0323, D.Chavez, LDRD Office, 1011

Sandia National Laboratories